Over 100 GHz High Power Modified Uni-Travelling-Carrier Photodiodes for Analog Optic Link

A Dissertation

Presented to
the Faculties of the School of Engineering and Applied Science
University of Virginia

In Partial Fulfillment of the
Requirements for the Degree of
Doctor of Philosophy

By

Qinglong Li

January 2018

APPROVAL SHEET

The dissertation is submitted in partial fulfillment of the requirements

for the degree of

Doctor of Philosophy in Electrical Engineering

Author:

Qinglong Li

This dissertation has been read and approved by the examining Committee:

Dr. Archie L. Holmes

Dr. Stephen J. McDonnell

Dr. Steven M. Bowers

Dr. Arthur W. Lichtenberger

Dr. Joe C. Campbell (Advisor)

Dr. Andreas Beling (Co-advisor)

Accepted for the School of Engineering and Applied Science:

Dr. Craig H. Benson, Dean, School of Engineering and Applied Science

November 2017

This dissertation is dedicated

to my parents, my wife and my daughter

Table of Contents

Acknowledgement

I feel lucky that I have the opportunity to work in one of the best teams in photonic research area across the world. There are so many excellent researchers in our group, and many of them made important contributions to my research work. I really would like to show them my deepest appreciation.

I would like to express my deepest gratitude to my advisor, Dr. Joe C. Campbell, for his support and guidance throughout my research work. He is such an enthusiastic person who is really into what he loves – research. He even listened to an audio book while he was mowing his lawn. His passionate to his research work motivate me a lot. Not only research work he could provide insightful thoughts and guidance, but also he always takes care of student's personal life and tries to offer the best he can provide. He is such an interesting person that he likes to share his life stories with us about everything. I would never forget his begins when he starts talking about his stories, like "When you are old, you will have many stories, and when I was at …". It is my great honor to be a student of such nice and knowledgeable man who made huge contributions to photonic research area.

I want to thank my co-advisor, Dr. Andreas Beling. He is really nice and decent to his student and treats everyone well. He is well organized and rigorous about work, and sets a good example for his student and other co-workers. To me, he provided great help and guidance for my research work and I benefited greatly from the discussion with him. He is also a humorous guy and he likes making jokes with us. It is my great fortune to have such a good co-advisor.

I appreciate Dr. Stephen J. McDonnell, Dr. Arthur W. Lichtenberger, Dr. Steven M. Bowers and Dr. Archie L. Holmes for kindly serving on my committee, reviewing my work and offer good advices.

I would like to thank my fellow research group members and colleagues, Kejia Li, Keye Sun, Yaojia Chen, Xiaojun Xie, Yang Shen, Wenlu Sun, Lijun Li, Min Ren, Zhanyu Yang, Jizhao Zang, Qianhuan Yu, Ze Wang, Ye Wang, Yang Fu, Bassem Tossoun, Jesse Morgan, Jiyuan Zheng, Yuan Yuan, Nan Ye, Taching Tzu, Fengxin Yu, Yiwei Peng, Andrew Jones and Maddy Woodson. It was my great time working together with them. Especially, I would like to thank Kejia Li for mentoring me at the start of my Ph.D. work and Keye Sun for great discussion about technical problems.

I want to thank my friends at University of Virginia, Ge Song, Jie Lian, Yukang Feng, Chi Zhang, Fei Yan, Longteng Wang who share with me their happiness, sadness. We grew up together during this important part of my life. Appreciate them a lot for showing up at this time. My dissertation is incomplete without their help and support.

I would like to thank all the staff members of the Microfabrication Lab at University of Virginia, including Alex Lobo, Michael Stogoski, Joseph Beatrice. With their good maintenance on the tools in cleanroom, I was able to finish my work for my dissertation.

I would like to greatly thank to my parents for always giving out without even asking for anything back. I feel guilty of not being able to go back to see them during my Ph.D. work, especially when they are getting older. For sure, I could not achieve this degree without their great support. I love them deeply and I am forever grateful for their love.

From the bottom of my heart, I would like to appreciate my beautiful wife, Shaoting Hu, who loves me and supports me for whatever I do. Without her, I would not ever have thought about coming to United States for study. She is such a kind and thoughtful person that I am so fortunate to have her in my life. The dissertation is impossible to complete without her.

I would like to thank my little baby girl, Amelia Li, who will soon be born in the next couple of months when I write this dissertation. It is amazing that this little angle will come into my life and bring the most significant and pleasant moments in my life. I feel very grateful about the opportunity to be a father and I can’t wait to see her growing up and be a woman like her mother.

Abstract

Since 1970s when fiber-optics were introduced, they have revolutionized the telecommunications industry. With the development of low loss fiber, fiber optic links have proved to be advantageous over their electronic counterparts (coaxial cables) for a number of applications in terms of low loss, high EMI immunity and large bandwidth. Although digital optic links dominate the fiber optics communications, there are growing interests in analog optic links for applications like RoF wireless communications, phased arrayed antennas, antenna remoting and radio astronomy most of which are for military use. As demand for high speed communication, the carrier frequency has to increase (in mmW range) to accommodate this change. Photonic generation of mmW carrier frequency can provide not only wide tunable carrier frequency range with low phase noise, but also reduce system cost by eliminating the expensive electronic components if an optical to electrical (O/E) converter can handle high enough power. At the same time, in mmW frequency, atmosphere attenuation due to oxygen, water absorption is not trivial, and high output power from the O/E converter is necessitated to compensate the large attenuation in order to provide large coverage for wireless communication. In conclusion, development of high power high speed photodiodes is necessitated for these applications.

In this work, over 100 GHz high power modified uni-travelling-carrier (MUTC) photodiodes for high speed and high power 1.55 μm applications were developed and characterized. Both surface normal photodiode and evanescently-coupled waveguide photodiode are realized with over 100 GHz frequency. With benefit of uniform absorption, easy coupling, over 100 GHz surface normal back-illuminated flip-chip-bonded MUTC photodiodes with inductive peaking can

deliver RF output power levels as high as 9.6 dBm at 100 GHz and 7.8 dBm at 110 GHz, respectively. Through optimization of impedance of the CPW line together with the extracted parameters and circuit model, bandwidths of 125 GHz with flat frequency response were achieved with 5 μm-diameter. A 6 μm-diameter photodiode achieved 3.3 dBm and 0.83 dBm RF output power at 130 GHz and 150 GHz, respectively; With benefit of high speed along with high efficiency from a waveguide integration, high power evanescently-coupled MUTC photodiodes were achieved with 38 GHz bandwidth efficiency product compared with normal incidence devices of 15 GHz. Waveguide photodiodes can output RF power of 7.8 dBm and 6.1 dBm at 60 GHz and 70 GHz, respectively and smaller device can achieve over 90 GHz bandwidth with RF output power of 2 dBm and 1.3 dBm at 100 GHz and 105 GHz, respectively. To demonstrate the photonic integration capability with my photodiodes, a photonic integration of W-band emitter was realized by flip-chip bonding high power surface normal photodiodes onto a Vivaldi antenna with matching network. The emitter can output as high as 5 dBm effective isotropic radiation power at 110 GHz, which is among the highest that have been reported in this frequency range. The compact integrated photonic emitter is fully compatible with planar integration.

List of Figures

List of Tables

Chapter 1. Introduction

A fiber optic communication system uses an optical fiber as the transmission medium and light as the carrier to transmit information. Compared with electrical cabling, a fiber optic system offers advantages of light weight, wide bandwidth, frequency-independent low propagation loss (for long distance transmit) and better immunity to electromagnetic interference. With recent fast development of photonic components, fiber-optics have advanced the telecommunication and data transmission industries into a new era.

1.1 Analog Optic Link

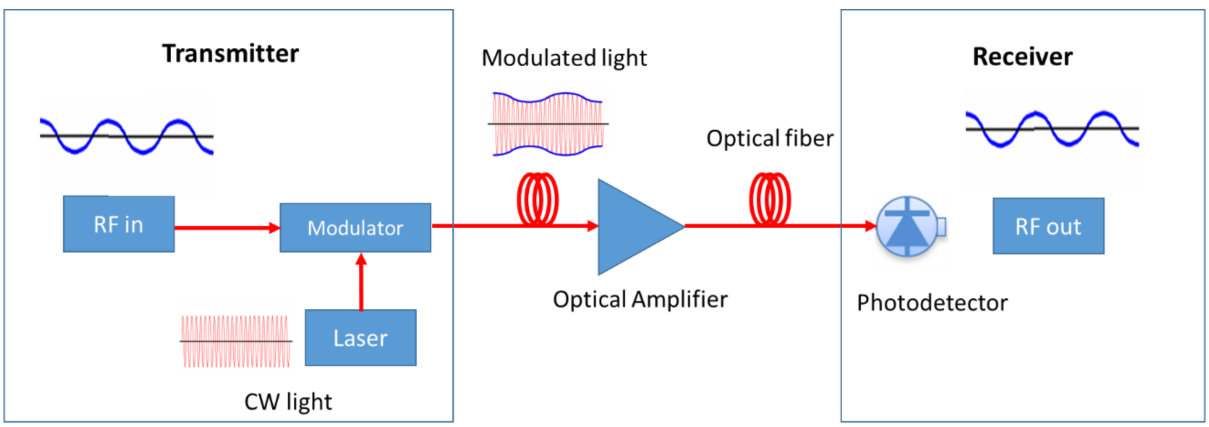

Figure 1-1. Simple analog fiber optic link.

A fiber optic link typically consist of three parts: transmitter, transmission medium (optical fiber) and receiver. Most fiber optical systems implement digital links for data transmission due to their large tolerance of noise. However, analog optic links are ideal for applications that require signals with high fidelity. There are many applications for analog optic links, such as, video distribution in CATV; analog fiber optic delay lines, in which the length of the analog optical link fiber can be used for storage, and also can provide true time delay for phased arrayed beamforming, which can be used for military radar systems; medical ultrasound imaging; antenna remoting, in which a high fidelity RF signal is transmitted between an antenna and a base station through an analog optic link with the benefit of removing expensive instruments used in the base station [1-1].

For an analog link, figures of merit to characterize the link performance include the noise figure, spurious free dynamic range (SFDR) and link gain [1-2]. The noise factor quantifies the noise performance of the link. Mathematically, the noise factor is the ratio of the signal-to-noise ratio (SNR) at the input to that at the output. The noise factor is often expressed in dB. The SFDR is defined as the range of input powers over which the output signal is above the noise floor and all the distortions are below the noise floor. The SFDR quantifies how well the system can resist distortion response. Finally, the link gain is the ratio of the output RF power at the load to the input RF power. Due to the nature of analog signals, low noise figure, large SFDR and high link gain are essential for signal transmission with high fidelity. One way to improve the link performance is to increase the input optical power. Therefore, at the receiver side, a photodiode that can handle high power is beneficial for link performance.

1.2 Photonic generation of millimeter wave

The millimeter wave (mmW) or sub-terahertz wave of the electro-magnetic spectrum ranges from 30 to 300 GHz, corresponding to the wavelength range 1 to 10 mm. In recent years, there has been growing interest in the mmW region as a result of the wide application space. The mmW spectrum is extensively used in a broad range of applications such as telecommunication, military and defense, sercurity screening, automotive and healthcare [1-3]~[1-6]. In security sensing, with small enough wavelength the mmW can transmit through cloth or other orgnanic materials to detect weapons or contraband carried under clothing. Since the mmW does not penetrate skin but only reflects, it causes no harm to the body and has been widely deployed in airport security systems as seen in Figure 1-2.

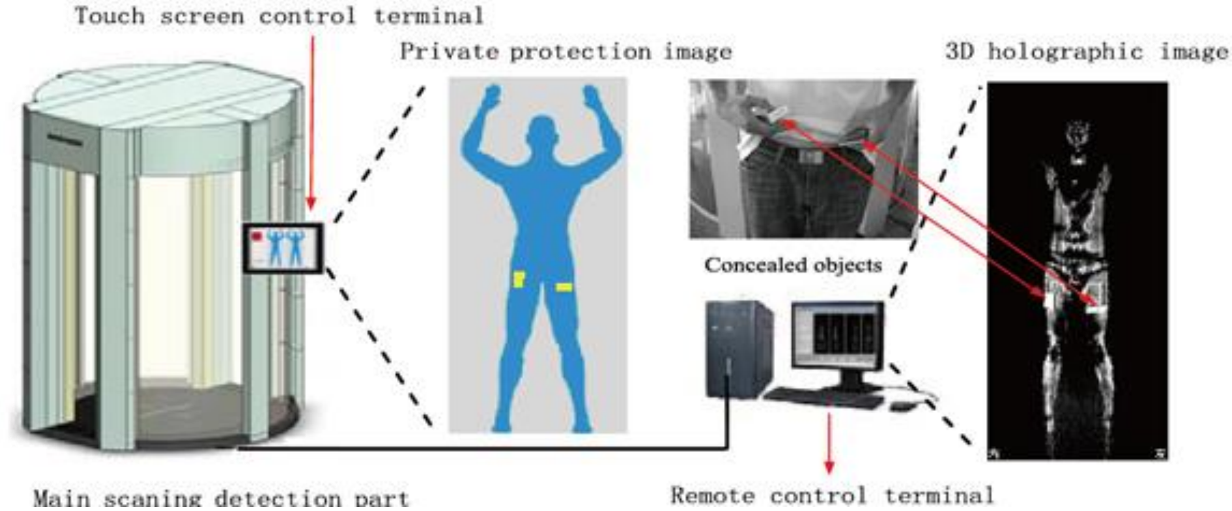

Figure 1-2. Millimeter wave detector.

For telecommunication, althrough the mmW tends to attenuate faster through the atmosphere due to gases or water absorption, an important implementation of mmW is for short wireless communication. In the mmW range, a wide available frequency spectrum with faster data rates is expected. Recently, the IEEE defined the Wireless Personal Area Network (WPAN) standard, IEEE 802.15.3c [1-7], in which the wireless data rate can reach up to 5.3 Gb/s with single carrier frequency of 57 ~ 64 GHz. Therefore, generation of good mmW carrier signals is critical for this high speed wireless communication. Electrical oscillators, such as frequency multiplication, impact ionization avalanche transit time IMPATT diodes and Gunn diode oscillators, can generate frequencies above 100 GHz, but with relatively high phase noise.

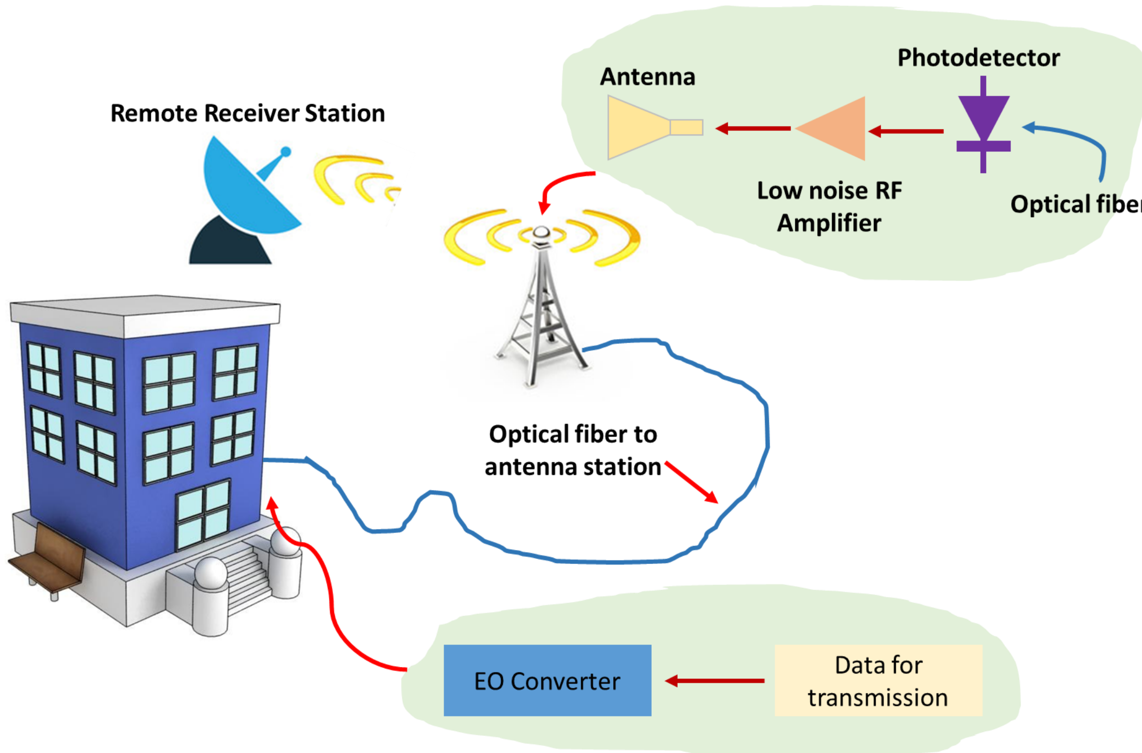

Figure 1-3. Photonice-based wireless communication sytem architecture.

Photonic mmW generation not only provides extremely broad tunable bandwidth with low loss as a result of the optical fiber, but also lowers phase noise compared with electrical signal generation [1-8]~[1-10]. Among the photonic techniques to generate mmW, photomixing is a simple and promising way to realize continuous, stable and variable-freqeueny signals with low cost. In photomixing, two optical beams separated in frequency, f_{RF}, are mixed together onto the photodiode which can generate the mmW signal in terms of their beat signal. Therefore, the frequency response and power handling capability of a photodiode determines the available power that can be broadcast from the attenna. Meanwhile, post amplification of the mmW signal using a low noise amplifier can be eliminated if the photodiode handles high enough power. It is desireable to develop a high power and high speed (over 100 GHz) photodiode that meets this criteria. Figure 1-3 shows a typical fiber-based wireless communication system architecture, which illustrates electrical-to-optical (EO) conversion, fiber uplink to the antenna, and optical-to-electrical (OE) conversion for free-space RF transmission.

1.3 Dissertation orginization

The pursuit of high-performance and high-speed optical links for optic communcations has driven the development of photodetectors that can operate at high optical power to improve the optical link performance. The motivation of my dissertation is to develop high-power and high-speed photodiodes that meet these requirements.

Chapter 2 introduces the fundamentals of high-power photodiodes and ways to improve power and speed performance; Chapter 3 discusses the photodiode fabrication processes and device characterization techqinues; Chapters 4 and 5 describe the realization of > 100 GHz surface normal and waveguide integrated MUTC photodiodes with high RF output power; Chapter 6 presents the integration of the surface-normal 100 GHz high-power MUTC photodiode with an antenna and matching network to achieve a high-power W-band photonic emitter. Chapter 7 sumarizes this work and includes suggestions for future work.

Chapter 2. High Power and High Speed Photodiode

2.1 Introduction

In this chapter, first, the factors that limit the speed and power performance of a photodiode are illustrated. Then, photodiode structures are discussed and their advatanges and disadvatages are presented. Finally, strategies used to improve the device power and speed are presented.

2.2 Photodiode Power Delivery

RF power is the amount of AC power delivered to the load. For a single frequency sinusoidal signal with frequency f, the RF power can be expressed as:

$$P_{RF} = |I_{(t,f)}|^2 Z$$

Eq. (2.1)

Where $\left|I_{(t,f)}\right| = \frac{I_p}{\sqrt{2}}$ is the root mean square (RMS) of the AC current, Z is the impedence of the load, which is usually pure resistance of 50 ohms, and I_p represents the peak current. Asumming 100 % modulation depth, the DC photocurrent, I_{dc} , is equal to the peak amplitude of the AC current, I_p. Therefore, the RF power delivered to the load is:

$$P_{RF} = \frac{1}{2} I_{dc}{}^2 R_{load}(50\ ohms)$$

Eq. (2.2)

Ideally, it is expected that the output of the optical to electrical converter should always follow a linear trend with input signal, like the power transfer curve shown below (ideal power) in Figure 2-1. However, in fact, the power transfer charatersitc of a tyical photodiode does not act this way. Usually, the output initially increases linearly and then deviates from the linear response as the input optical signal continutes to increase. Finally, the output of the photodiode saturates. Further increase of the input signal causes failure due to thermal effects or dielectric breakdown. The RF compression is defined as the deviation of the measured RF output power from the ideal linear output calculated from Eq. (2). The photodiode RF saturation is defined as the point where the RF compression decreases 1 dB from its peak value. The photocurrent at which this occurs is the saturation current.

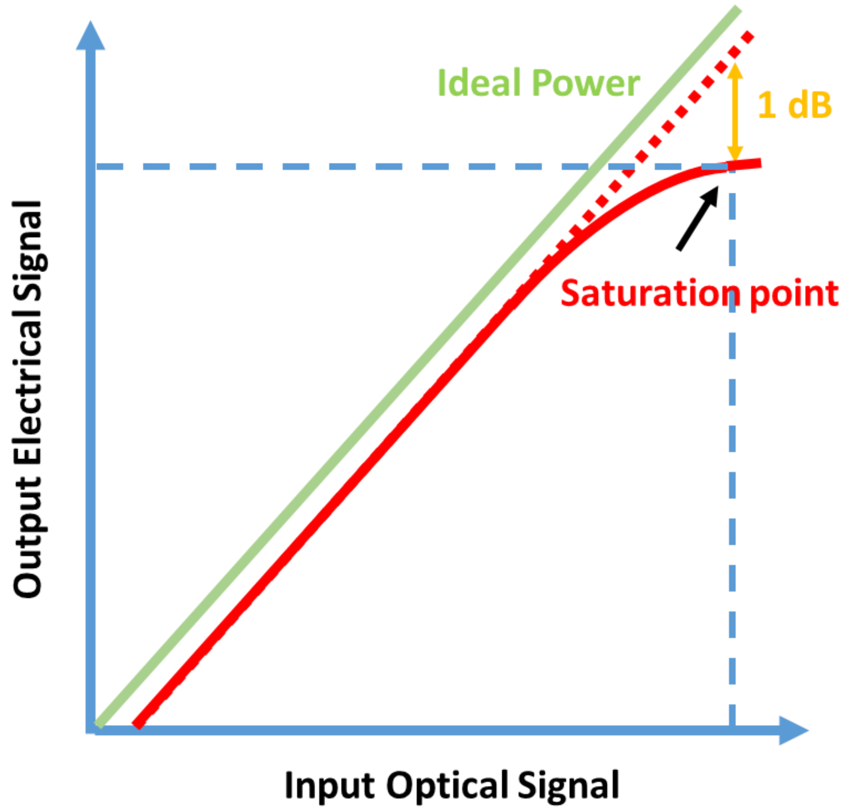

Figure 2-1. Power transfer curve of a typical photodiode and its saturation.

Two factors limit the photodiode power delivery performance. One effect that gives rise to saturation originates from the space charge effect, which results from charge screening in the depletion region. As shown in Figure 2-2, when incoming photons are absorbed in the intrinsic region in a PIN photodiode, electron and hole pairs are generated and they drift toward the anode and cathode at high velocity. With increased density of mobile carriers as the input optical power increases, the charges accumulate toward the edges of the depletion region which gives rise to an internal field that opposed the applied bias. This can be explained in terms of the Poisson equation (take one dimenstion for simplification):

$$\frac{dE}{dx} = \frac{\rho_{(x)}}{\varepsilon_0 \varepsilon_r} = \frac{q}{\varepsilon_0 \varepsilon_r}(-N_A + N_D - n + p)$$

Eq. (2.3)

$$E = \int_{x}^{x+\triangle x} \frac{\rho_{(x)}}{\varepsilon_0 \varepsilon_r} dx = \frac{q}{\varepsilon_0 \varepsilon_r} \int_{x}^{x+\triangle x} (-N_A(x) + N_D(x) - n(x) + p(x)) dx$$

Eq. (2.4)

where the E is the electric field; $\rho_{(x)}$ and $\varepsilon_0 \varepsilon_r$ are the charge density in the depletion region and absolute permittivity of the semiconductor materials; N_A, N_D, are the immobile acceptor and donor concentration; and n, p are electron and hole concentrations, respectively. In a PIN photodiode, the intrinsic layer is undoped, and therefore, the slope of the electric field in this region is approximately zero, which indicates that there is a constant electric field across the whole intrinsic region. As the photogenerated electrons and holes started drifting in the depletion region, each location along the intrinsic region has different charge density. And therefore, the electric field strength varys along the intrinsic region, or in another words, the electric field is distorted. It is well known that for sufficiently high bias voltage, the carriers exhibit velocity saturation due to balancing of carrier kinetic energy gain and loss. As seen from Figure 2-2, as the optical signal increases, the electric field collapses more and more until the reduced electric filed cannot maintain the saturation velocity of the carriers. There is always a location where the electric field exhibits a minimum because n and p are equal and net charge density is zero. Typically, that location is closer to n-side electrode since electrons move faster than holes.

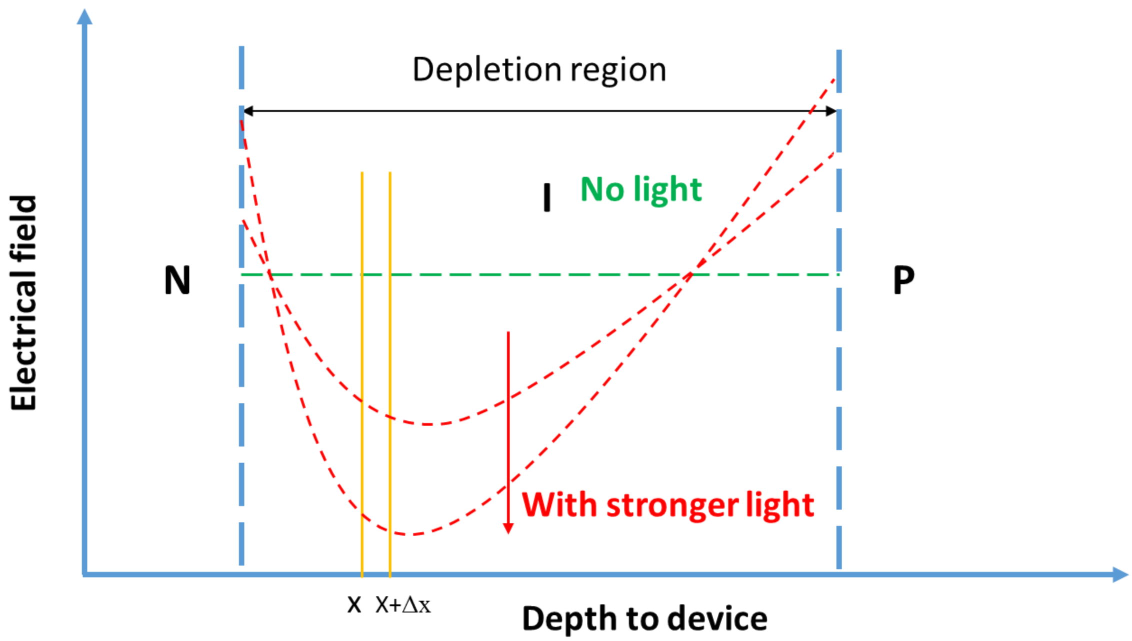

Figure 2-2. Electric field distribution across a PIN photodiode with and without light.

Another factor that limits the output power of a photodiode is heat dissipation. The high electric field in the depletion region contributes to most of the heat generation in a photodiode. For a typical telecommunication PIN photodiode, the intrinsic layer (InGaAs) with narrow bandgap serves both as the absorber and the depletion region. Its poor thermal conductivity of 0.05 $W \cdot cm^{-1} \cdot K^{-1}$ constrain the heat dissipated from the drift layer to the InP substrate layer (0.68 $W \cdot cm^{-1} \cdot K^{-1}$) [2-1]. As a result, the device junction temperature increases as the optical input increases, finally leading to thermal failure. The mechanism is a thermal runaway process with a positive feedback loop as seen in Figure 2-3. It proceeds as follows: the temperature increase in InGaAs leads to reduced energy bandgap of InGaAs. The reduced bandgap absorbs more photons with more phonon scattering, which generates more heat. At the same time dark current of the junction also increases. These lead to further increase in the junction temperature, which may activate defect states. Finally, the device dies as a result of thermal breakdown.

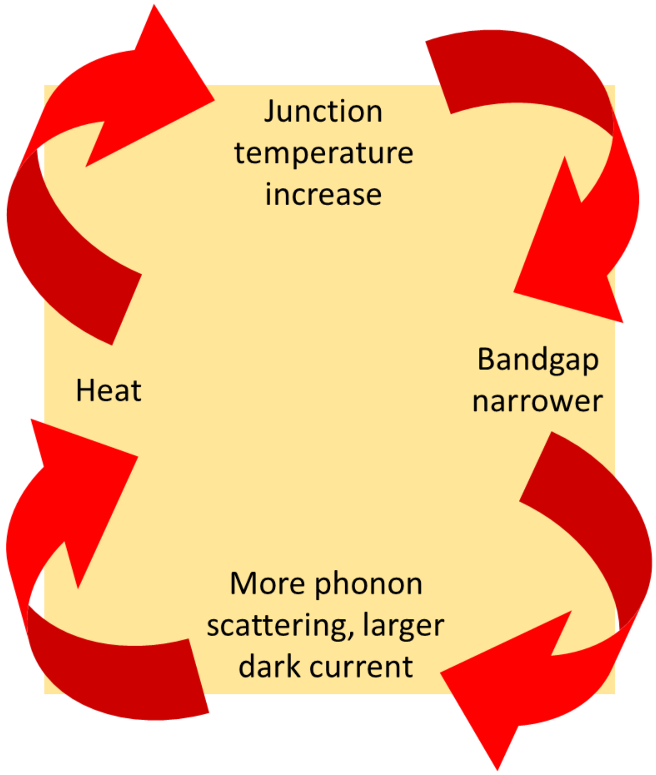

Figure 2-3. Thermal runway process with positive feedback.

2.3 Photodiode Speed

A photodiode can be treated as a low pass filter when reversed biased. The 3-dB bandwidth is used to describe the frequency response of a photodiode. The bandwidth is defined as the frequency where RF output power decreses 3 dB from its low frequency value. The speed of device is primarily limited by the carrier transit time and the RC circuit response time as illustrated in Figure 2-4.

The carrier transit time is the time required for the photo-generated electrons and holes to travel through the depletion region to the quasi-neutral p and n regions. Assuming light uniformly illuminates a PIN photodiode with absorber thickness d, and that the electron, hole travel at a constant saturation velocity, V_e and V_h, respectively, the normalized current can be expressed as [2-2]:

$$\frac{I(\omega)}{I(0)} = \left[\frac{1}{\omega^2{\tau_e}^2}\{1 - \exp(j\omega\tau_e)\} - \frac{1}{j\omega\tau_e}\right]\left[\frac{1}{\omega^2{\tau_h}^2}\{1 - \exp(j\omega\tau_h)\} - \frac{1}{j\omega\tau_h}\right]$$

Eq. (2.5)

where $I(\omega)$ is the photo-current at frequency ω and $I(0)$ is the DC photo-current; τ_e, τ_h are the electron and hole transit times, respectively; and ω is the angular frequency. The 3dB transit time limited frequency f_t can be achieved when $\left|\frac{I(\omega)}{I(0)}\right| = \frac{1}{\sqrt{2}}$, and approximated as:

$$f_t \approx \frac{3.5\,\bar{V}}{2\pi d}$$

Eq. (2.6)

where $\bar{V}$ is the average drift velocity in the depletion region and can be defined as:

$$\bar{V} = \frac{1}{\sqrt[4]{\frac{1}{2}\left(\frac{1}{V_e^4} + \frac{1}{V_h^4}\right)}}$$

Eq. (2.7)

The term f_t represents the device frequency response if the RC time constant is small. From Eq. (2.6), we can conclude that f_t is primarily limited by d, the absorber thickness of the PIN photodiode.

As seen in Figure 2-4, which is the RC time equivalent circuit, a photodetector is a current source with internal series resistance, R_s, junction capacitance, C_{pn} in parallel with a large junction resistance, R_p, and a 50 ohm load resistance, R_L. Assuming $R_p$is large enough that it can be treated as open circuit, the current flow through the load becomes:

$$I(\omega) = I(0)\frac{\frac{1}{j\omega C_{pn}}}{\frac{1}{j\omega C_{pn}} + (R_s + R_L)} = \frac{I(0)}{1 + j\omega C_{pn}(R_s + R_L)}$$

Eq. (2.8)

The junction capacitance, C_{pn} is estimated with:

$$C_{pn} = \frac{\varepsilon_0 \varepsilon_r A}{d}$$

Eq. (2.9)

where A is the photodiode junction area. The RC time bandwidth f_{RC} can be expressed as:

$$f_{RC} = \frac{1}{2\pi C_{pn}(R_s + R_L)}$$

Eq. (2.10)

Therefore, C_{pn} is the dominate factor for the RC limited bandwidth if the photodiode internal resistance is not comparable with to the load. However, for a hundred-GHz-bandwidth device the size of photodiode is expected to be in the range of a few microns in diameters, which results in larger contact resistance. For that case, the device series resistance also needs to be taken into consideration.

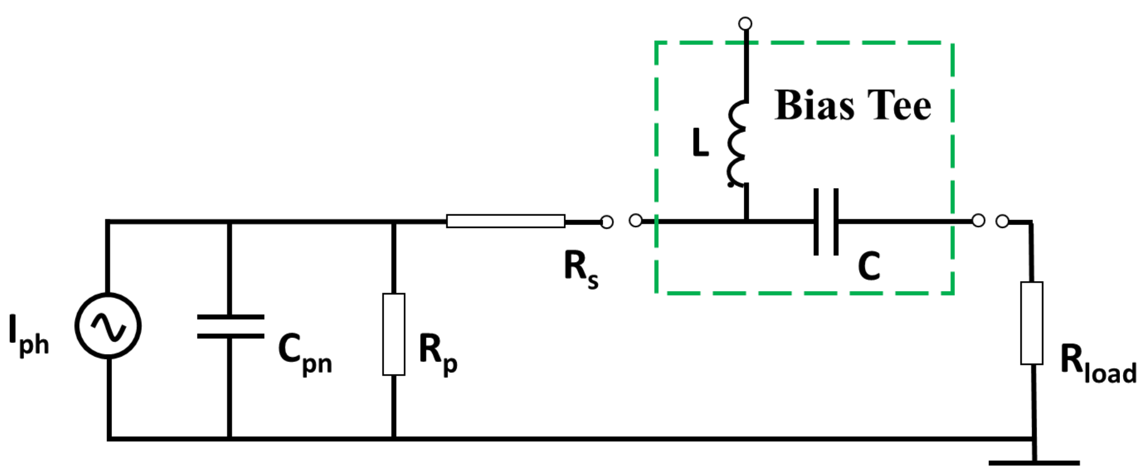

Figure 2-4. A typical photodiode equivalent circuit model.

If the transit time and RC time bandwidth have Gaussian responses, the 3 dB bandwidth, f_{3dB}, can be approximated as [2-2]:

$$f_{3dB} = \frac{1}{\sqrt{\frac{1}{f_t^2} + \frac{1}{f_{RC}^2}}}$$

Eq. (2.11)

2.5 Inductive Peaking

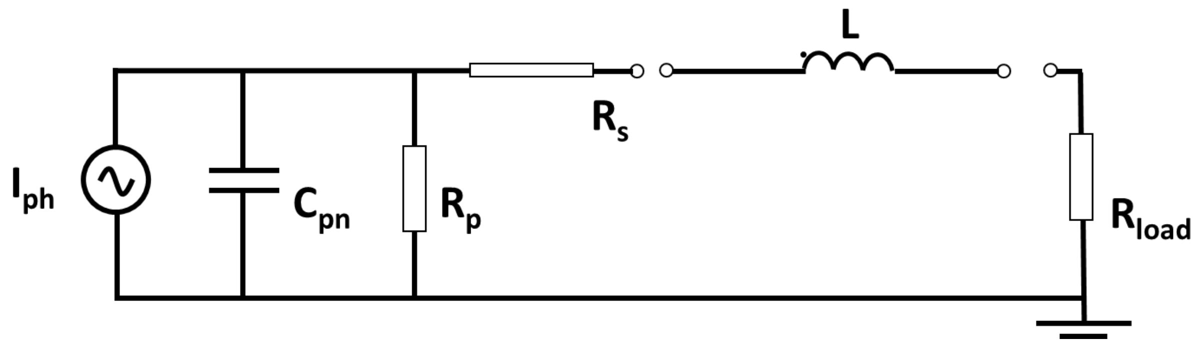

Figure 2-5. A typical photodiode equivalent RLC circuit model.

The RC-limited bandwidth can be further improved by incorporating an inductor in a photodiode circuit. The equivalent RC model of a photodiode with an inductor is shown in Figure 2-5. The current flow through the load can be written as:

$$\frac{I(\omega)}{I(0)} = \frac{1}{1 - \omega^2 LC + j\omega C(R_{load} + R_s)}$$

Eq. (2.12)

The inductor L can cause peaking effect at a certain resonant frequency. The resonant frequency, f_r, is given by the expression:

$$f_{resonant} = \frac{1}{2\pi\sqrt{LC_{pn}}}$$

Eq. (2.13)

It can be found that with an optimized inductor ($L = \frac{C_{pn}(R_{load}+R_s)^2}{2}$), the RC-limited bandwidth, f_{RLC}, has an optimium value:

$$f_{RLC}(optimum) = \frac{\sqrt{2}}{2\pi C_{pn}(R_{load} + R_s)}$$

Eq. (2.14)

The optimum f_{RLC} can be 41% higher than f_{RC} by incorporating an inductor. Figure 2-6 shows simulations of RC and RLC frequency responses, assuming 10 mA photocurrent, 100 fF C_{pn}, 151 pH L, 5 ohms R_s and 50 ohms R_{load}. From the curves, the RLC circuit (42 GHz) clearly shows 40 % improvement compared with RC circuit (30 GHz). The drawback for the RLC circuit can also be seen in figure 2-6 (b). Beyond the 3 dB bandwidth, the RF output power drops more rapidly with increasing frequency compared to the RC circuit. Above the 3 dB bandwidth, the power output from the RLC circuit drops 40 dB/dec compared with 20 dB/dec for the RC circuit. This is attributed to the peaking effect with a resonant frequency at 40 GHz. In conclusion, inductive peaking increases the bandwidth but at the price of a more abrupt decrease.

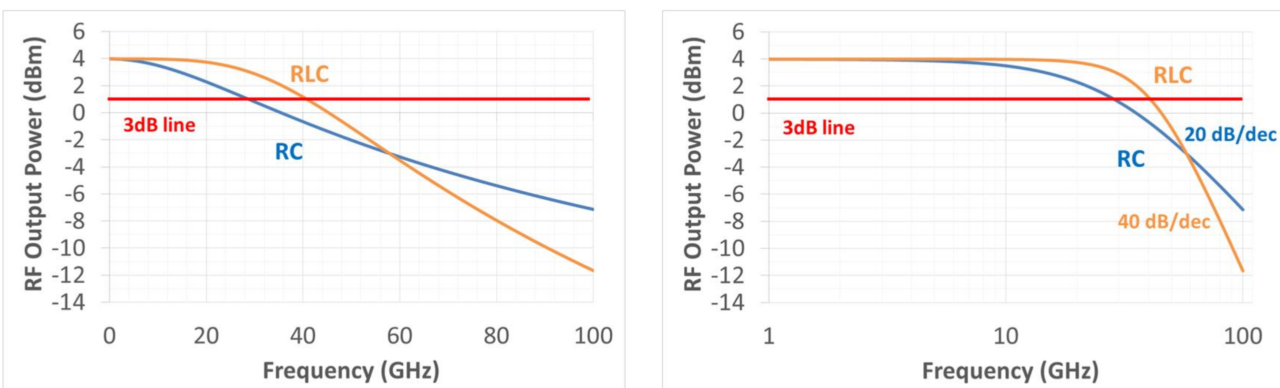

(a) (b)

Figure 2-6. Simulations of ideal photodiode circuits with and without an inductor. (a): linear scale (b): log scale.

Note that, by incorporating an inductor, the RLC response can no longer be treated as a Gausiaan reponse. As for the total photodiode bandwidth, Eq. (2.5) needs to be used for combining the frequency responses instead of the simplified model of Eq. (2.11).

An ideal inductor does not have any resistance or capacitance, however, there is always series resistance and parasitic capacitance associated with an inductor. In a certain frequency range, self-resonance may occur in which the parasitic capacitance resonates with the inductance. The inductor behaves like a short circuit or an open circuit at this frequency depending on whether the parasitic capacitace is in series or parallel with the inductor. Therefore, it is impractical to include a lump inductor into the high speed photodiode design.

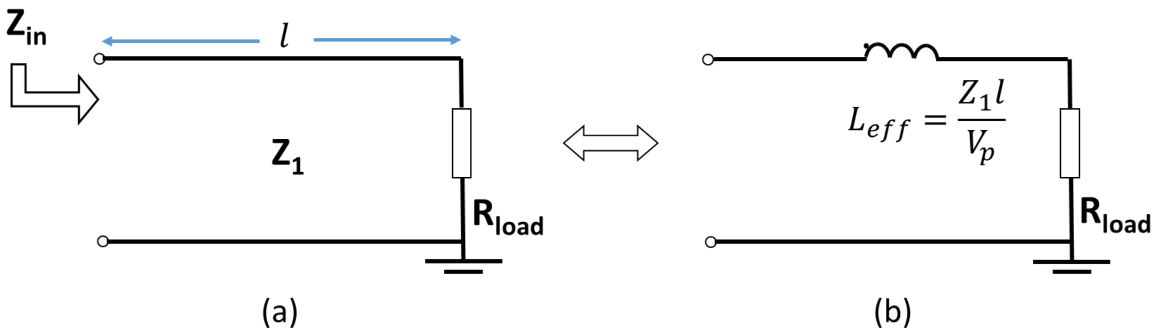

Figure 2-7. (a) Short section of transmission line; (b): Equivalent lump circuit of (a).

Instead, a short section of transmission line with a large characteristic impedance can be approximately treated as a series inductor. As seen in figure 2-7, the input impedance, Z_{in} , of a short transmission line terminated with a matched load, can be expressed with [2-3]:

$$Z_{in} = Z_1 \frac{Z_L + jZ_1 \tan \beta l}{Z_1 + jZ_L \tan \beta l}$$

Eq. (2.15)

where Z_1 is the characteristic impedance of the transmission line, Z_L is the load impedance, β is the phase constant of the wave and l is the length of the transmission line. Assuming a short length of transmission line with electrical length $\beta l < \pi/4$, Z_{in} can be approximated as:

$$Z_{in} \approx Z_1 \frac{Z_L + jZ_1\beta l}{Z_1 + jZ_L\beta l}$$

Eq. (2.16)

If Z_{in} is larger than Z_L,

$$Z_{in} \approx Z_L + jZ_1\beta l = Z_L + j\omega \frac{Z_1 l}{V_p} = Z_L + j\omega L_{eff}$$

Eq. (2.17)

where V_p is the phase velocity and L_{eff} is the equivalent inductor of the high impedance transmission line. Therefore, by incorporating a high impedance coplanar waveguide in the photodiode design, the device frequency can be dramatically improved.

2.4 Review of High Power Photodiode

In order to improve the link performance, it is critical to improve the photodetector power handling capacity. Various types of photodiode structures have been developed to improve power performance.

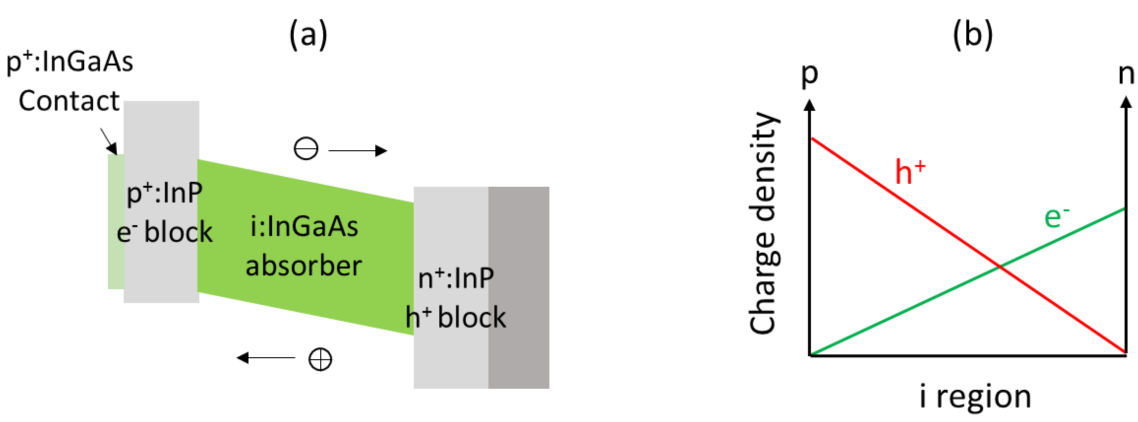

Figure 2-8. PIN photodiode (a): Band diagram; (b): Charge density in the depletion region.

The PIN photodiode is the simplest structure. Figure 2-8 (a) shows a schematic band diagram of a heterojunction PIN structure. Compared with the normal p-n diode, an intrinsic layer is inserted between two heavily n- and p- doped regions. The intrinsic region can provide a constant electric field under reverse bias. The PIN diode can handle higher optical power than a p-n diode. However, the unmatched drift velocity of electrons and holes in a PIN leads to an unbalanced electric field collapse. As shown in Figue 2-8 (b), for a constant photocurrent flow through the PIN diode, the higher saturation velocity of electron compared with hole causes the charge density at the n side to be smaller than that at the p-side. Therefore, the zero net charge density location is close to the n side. As a result, the electric field collapses toward the n-side. The advantage of the PIN photodiode is low recombination rate since all the photo-generated carriers are transported by drift in an electric field, which is beneficial to high internal quantum efficiency.

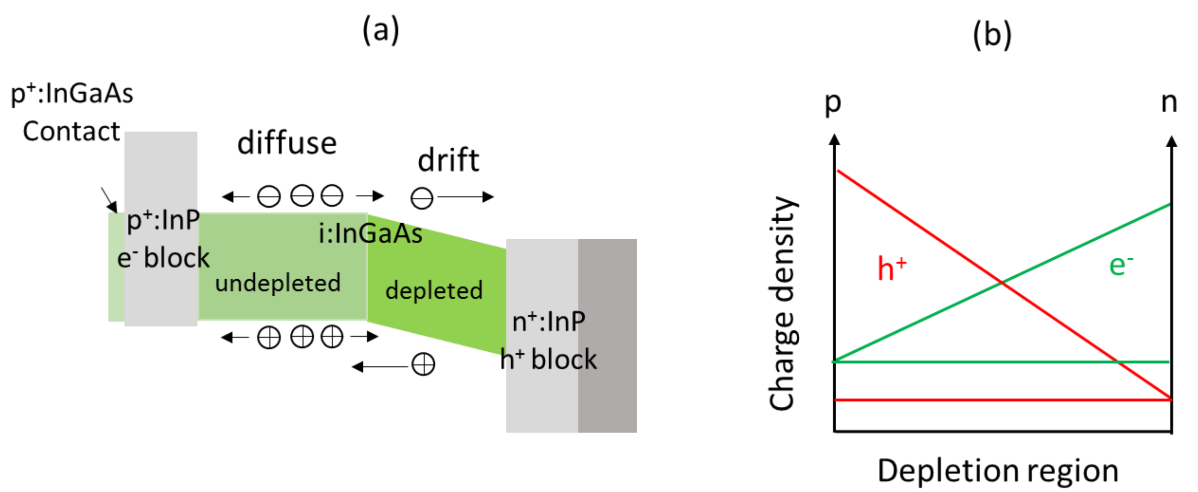

Figure 2-9. PDA photodiode (a): Band diagram; (b): Charge density in the depletion region.

Partially depleted absorber (PDA) photodiodes are designed to include both depleted and undepleted absorber regions to improve the power handling capability [2-4]. Unlike the PIN photodiode, the depletion region has holes and electrons that diffuse from the undepleted absorber. Since the depletion region always sweeps the minority carrer away, this leads to higher concentration of diffusive electrons than holes in the depletion region as seen in Figure 2-9 (b). By proper design of the ratio between the two absorbers the electric field collapse point can be optimized to the center of depletion region. Meanwhile, the thin depletion region in the PDA photodiode can lower the space charge effect relative to PIN photodiodes. In all, the power handling of a PDA photodiode is better than that of PINs. However, the drawback of PDA photodiode is that the diffusion process included in the undepleted absorber increases the transit time, which results in lower speed compared to PINs. Similar to PINs, the narrow bandgap absorber limits its thermal dissipation capability which may result in device early thermal failure.

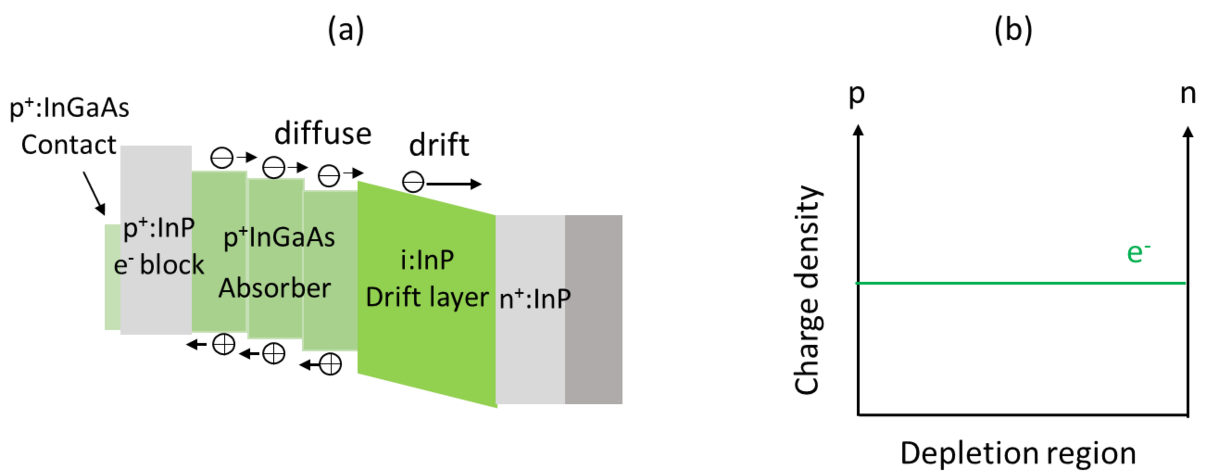

Figure 2-10. UTC photodiode (a): Band diagram; (b): Charge density in the depletion region.

Improved performance has been achieved with the uni-traveling-carrier (UTC) photodiode, demonstrated by Ishibashi in 1997 [2-5], in which only electrons traverse the depletion region. The UTC structure consists of a narrow bandgap (usually $In_{0.53}Ga_{0.47}As$) undepleted absorber adjacent to a wide bandgap (usually InP) drift layer as seen in Figure 2-10. The undepleted absorber is graded doping with which a quasi-electric-field can be formed to assist carrier transport. The excess hole density in the absorption layer decays quickly with the dielectric relaxation time and the photogenerated electrons are injected into the drift layer. Since only electrons transit the drift layer, the bandwidth of UTC photodiodes can be much higher than PIN photodiodes in which both electrons and holes, which are slower than electrons, contribute to the frequency response. Having a single carrier type in the drift layer also mitigates the space charge effect. Since most the heat is generated inside the large bandgap InP depletion/drift region, the thermal dissipation capacity is better than that of PINs and PDAs.

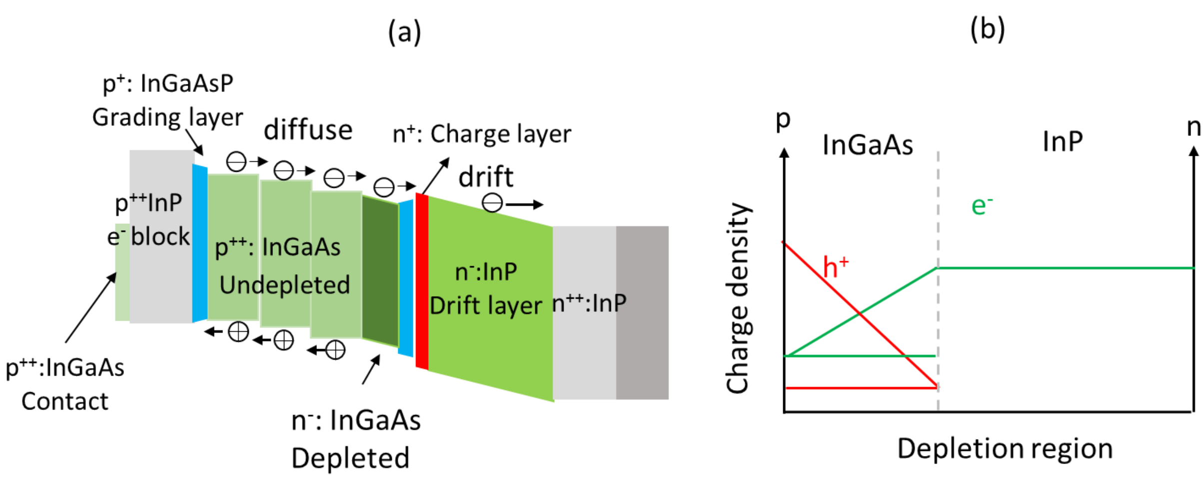

Figure 2-11. MUTC photodiode (a): Band diagram; (b): Charge density in the depletion region.

The performance of UTC photodiodes has been further improved by modifications of the epitaxial-layer structure. The modified UTC (MUTC) photodiode is shown in Figure 2-11 [2-6]. By incorporating a depleted InGaAs absorber layer with suitable thickness, the responsivity of the photodiodes can be increased without sacrificing bandwidth [2-7]. Of greater benefit, this layer helps to maintain high electric field at the heterojunction interfaces between the absorption and drift regions, which suppresses charge accumulation at the conduction band steps. At the heterojunction interface, quarternary InGaAsP layers are inserted to smoothen the bandgap discontiniuity which further mitigates the charge accumulation. The RF output power can also be increased by incorporating a light n-type doping in the drift layer [2-8], which pre-distorts the electric field to partially compensate the field change caused by the space charge effect. Finally, adding a charge layer, also referred to as a “cliff” layer [2-9], suppresses field collapse in the depleted absorber layer. Another factor that limits the output power is device heating.

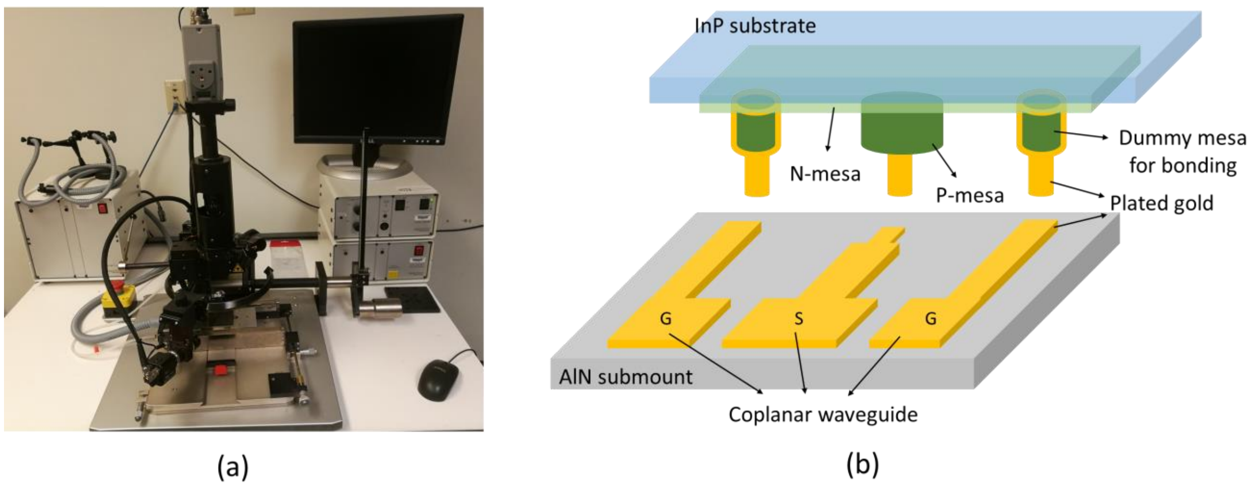

Figure 2-12. (a): Finetech flip-chip bonder; (b): 3D view of flipchip bonding process.

In order to improve thermal dissipation, a flip chip bonding technique is employed. It has been shown that improved thermal management through flip-chip bonding to high-thermal-conductivity substrates can provide significantly higher saturation current and RF output power [2-10]~[2-12]. Gold is chosen as the bonding material not only because it can be joined to itself at temperatures below its melting point, but also it provides good electrical conductance. The Au-Au bonding is a thermocompression process in which both force and heat are used to form a stable joint at the Au-Au interface. A 3D illustration of the flip chip bonding process is shown in Figure 2-12. A Finetech Lamda is the bonding machine. During the process, with 3~5 N force depending on the pillar size, the high power photodiode with plated gold on top of the p-mesa and dummy mesas is flip-chip bonded onto the gold of a coplanar waveguide on top of a high thermal conductivity heat sink AlN (2.85 $W \cdot cm^{-1} \cdot K^{-1}$). The AlN submount is placed on top of the heating stage beforehand. Then, the stage is heated up to 340 ºC followed by the thermocompression process.

Chapter 3. Photodiode Fabrication and Characterization

3.1 Introduction

This chapter describes the photodiode fabrication processes and device characterization techniques. First, fabrication of normal-incidence and waveguide integrated photodiodes are discussed. Details of process steps are illustrated in sequence. Then, electrical and optical measurement techqiues are introduced for device characterization, including current-voltage, capacitance-voltage, S parameter, responsivity, bandwidth and saturation measurements.

3.2 Fabrication of Normal Incidence MUTC Photodiode

3.2.1 P-metallizaztion

For high-speed near-infrared (1.55 μm) photodiodes, it is critical to achive a good p-type ohmic contact since a major part of the device series resistance comes from the p-type contact. Making low resistance electrical contacts to p-type InP is well known [3-1]. Therfore, for our MUTC deisgn, the substitution of p-type InP with a thin layer of p-type InGaAs contact layer is always preferable to achieve a low series resistance. Metal layer stacks of Ti/Pt/Au/Ti (20/30/50/10 nm) on the thin p-type InGaAs surface provides low contact resistance and good adhesion. The titaunium serves as the adhesion and platinum can prevent the gold migration into the III-V semiconductor, which can form deep level traps or spikes that short the device. Upon annealing, the gold-zinc alloy is favorable to reduce the contact resistance.

The metal stack is deposited using E-beam evaporation. Before deposition, the wafer is cleaned with IPA+Acetone+O_2 plasma to make sure the surface is free of particles and contaminates. Before loading into the E-beam chamer, the wafer is dipped in a buffered oxide etchant

($HF+NH_4F$) to remove native oxide. Then, the evaporation is carried out in vacuum level below ~1e-7 Torr. Three metal films are deposited in sequence to avoid defects or contaminates at the metal interfaces.

3.2.2 P-mesa etch

One of the most critical steps in the whole photodiode fabrication is the P-mesa etch. This step bacically defines the photodiode structure. Both wet etch and dry etch can be used to form the P-mesa. A wet etch solution can stop at the desired layer if the etchant has high selectivity. At the same time, the smooth side wall can be easily passivated, which results in lower dark current due to surface leackage. The disadvantage is that wet etching is isotropic and lateral undercutting can be an issue if a longer etch needed. For high-speed photodiodes with smaller mesa size, the dry etch technique has to be implementd in order to eliminate the undercut issue. However, this introduces side wall damage that may lead to higher dark current. In our experiments, a reactive ion etch (RIE) with Cl_2:N_2 gas mixture is used to etch III-V materials with 150 W RF power, and the ICP power (100 ~ 1000 W) which controls the plasma density can be adjusted to vary the dry etch rate.

We use an SiO_2 hard mask instead of photoresist to transfer the pattern due to faster etch rate of the photoresist in RIE. A PECVD 600 nm SiO_2 is deposited after the metal films. Note that the top of the p-metal stack is titanium without which SiO_2 detaches easily. For mesa lithography, AZ 5214 photoresist is spun on the wafers and pre-baked at 100 ºC for 2 min before exposure. We have a Karl Suss MJB4 contact lithography tool for exposure. The exposure time for 1.8 µm-thick AZ 5214 is ~ 25 s with equivalent dose of 170 mJ/cm^2. Then the wafer is developed in AZ 300 MIF developer for 30 s. The hard mask etch is done by dry etching with SF_6 gas prior to the mesa etch. After that, the p-mesa etch is performced in the Oxford RIE machine. We typically prepare a dummy SiO_2 wafer, which has the same oxide thickness as the device wafer and this dummy wafer can monitor how much of the SiO_2 is etched. The thickness of the SiO_2 is measured with an interferometer. The step height of the mesa plus oxide can be determined by a profilometer. Therefore, with step height of the mesa plus mesa and remaining oxide on the mesa, we can precisely mesure how much III-V we etched away. Figure 3-1 shows a schematic cross section of the photodiode after mesa lithography and etch along with the images taken post p-mesa etch.

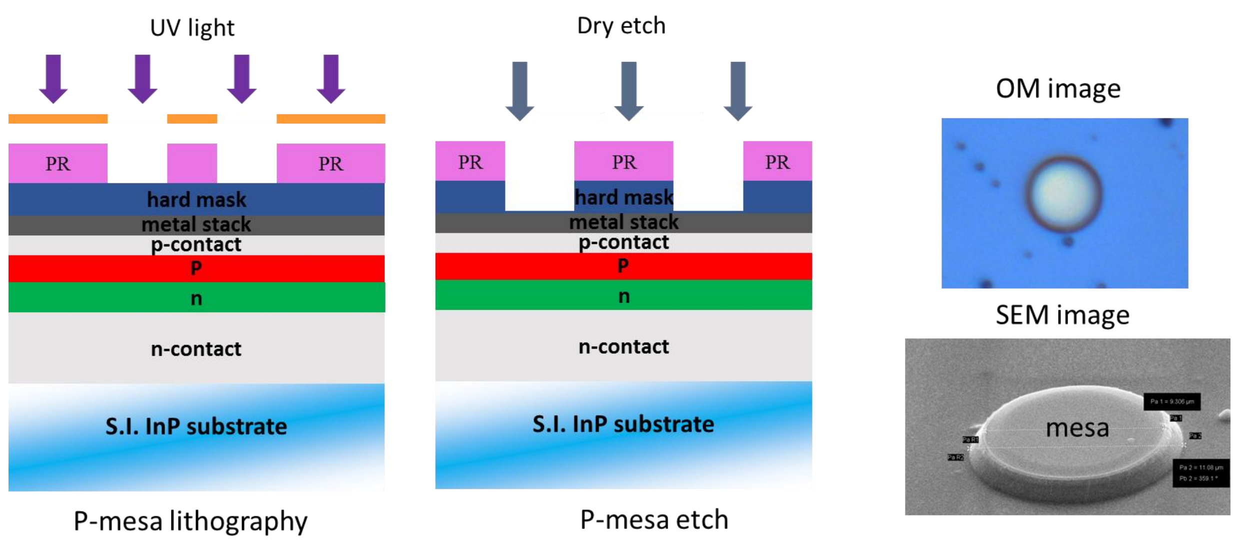

Figure 3-1. Schematic cross section view of P-mesa steps and device images. (S.I.: semi-insulating)

3.2.3 N-mesa etch

Post p-mesa etch, the wafer is cleaned and loaded into the PECVD chamber for another layer of SiO_2. This oxide layer is 300 nm thick. It serves as the passivation layer. Normally, the RIE uses a plasma, to chemically and physically etch way the III-V materials. However, it can also induce defects along the sidewall due to dangling bonds. This SiO_2 can passivate those dangling bonds, thus reducing the suface leackage current and preventing device degradation. This SiO_2 is also used as the hard mask for n-mesa formation.

The n-mesa is realized after passivation to isolate each device. For on-wafer RF pads, the heavily doped n-type layer beneath the RF signal pad must be removed to expose the semi-insulating layers in order to minimize the RF signal loss. For flip-chip bonded device, the isolated n-mesa can reduce the parasitic capacitance resulting from the larger overlap between the RF signal pads and the n contact layer.

Standard lithography with the n-mesa pattern is followed by a hard mask etch and III-V etch into the semi-insulating substrate as shown in Figure 3-2.

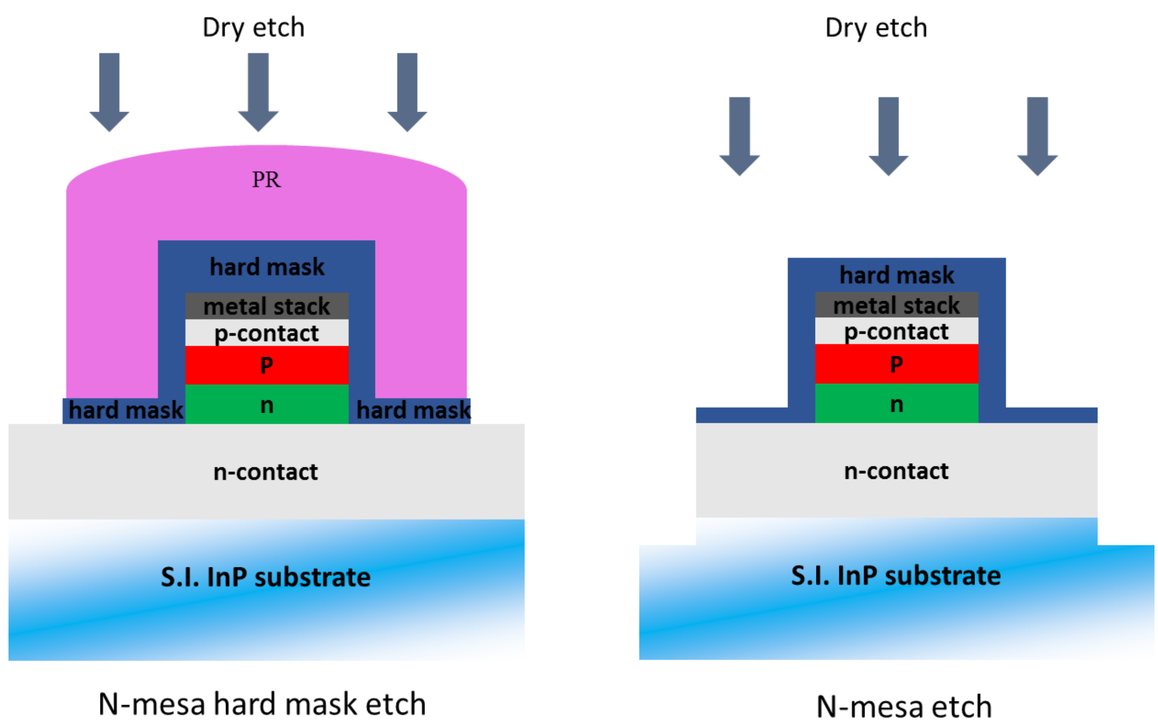

Figure 3-2. Schematic cross section view of N-mesa steps. (S.I.: semi-insulating)

3.2.4 N metallization

Unlike p-type InP, n-type InP can easily achive low resistivity with heavy Si doping. The n-metal stacks we use usually consist of AuGe/Ni/Au (30/20/80 nm), which can provide low series resistance and good adhesion. Due to the low eutectic melting point, AuGe is preferable for both InP and GaAs contact metal. For InP, it is believed that, upon annealing at ~320 ºC, a Au_xIn_y alloy with lower barrier height at the InP interface forms while indium out-diffuses and Au diffuses inward, and the Ge settles in the indium vacancies as a donor. This results in contact resistance as low as 10^{-7} $\Omega\cdot cm^2$ [3-2].

Similar to P-metal stack, after standard lithography, the n metal is deposited by E-beam evaporation. A lift-off process is done to remove the unwanted metal together with photoresist.

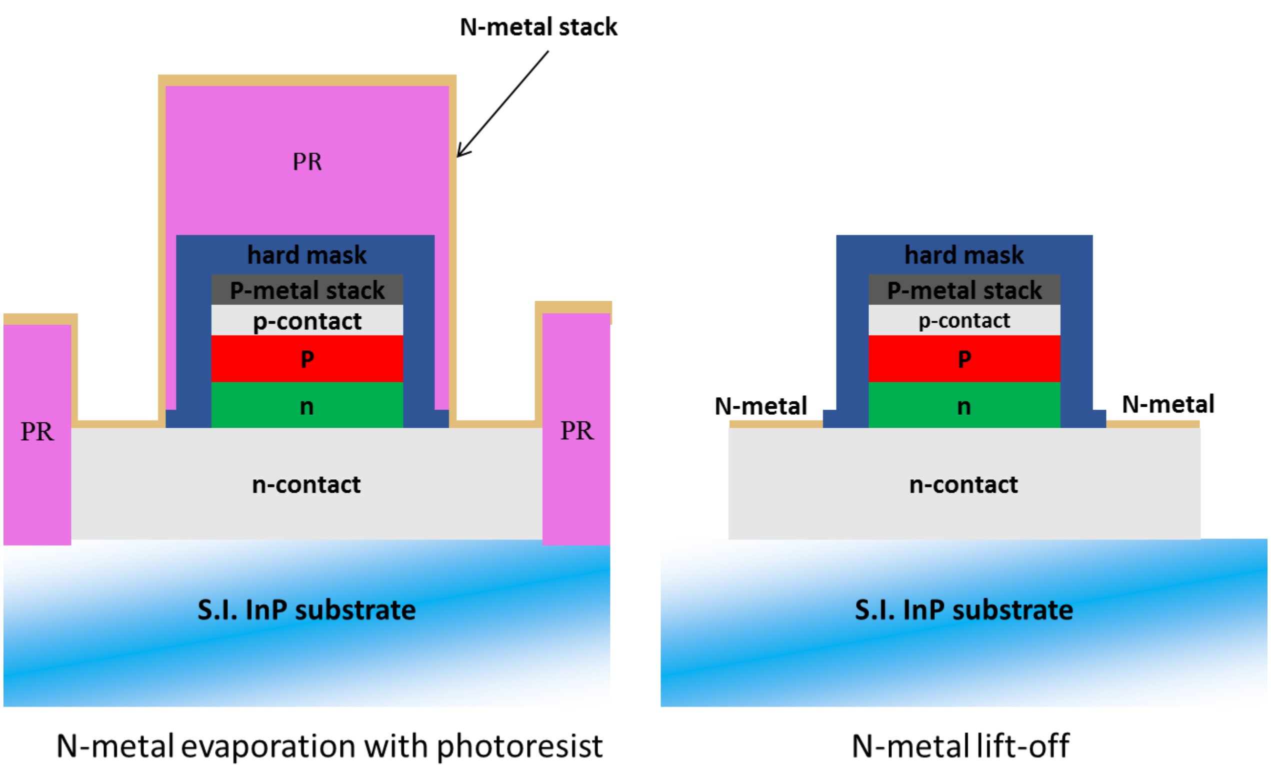

Figure 3-3. Schematic cross section view of N-metal steps. (S.I.: semi-insulating)

3.2.5 *P contact open*

A thin layer of SiO_2 needs to be removed in order to make connection to the RF pads. For high-speed devices with diameter as small as 5 µm, the contact opening has to be even smaller, which makes the alignment difficult with our contact aligner. It is preferable to work with projection lithography for < 1µm alignment tolarence. Figure 3-4 shows a schematic view of the procedure to open the contacts.

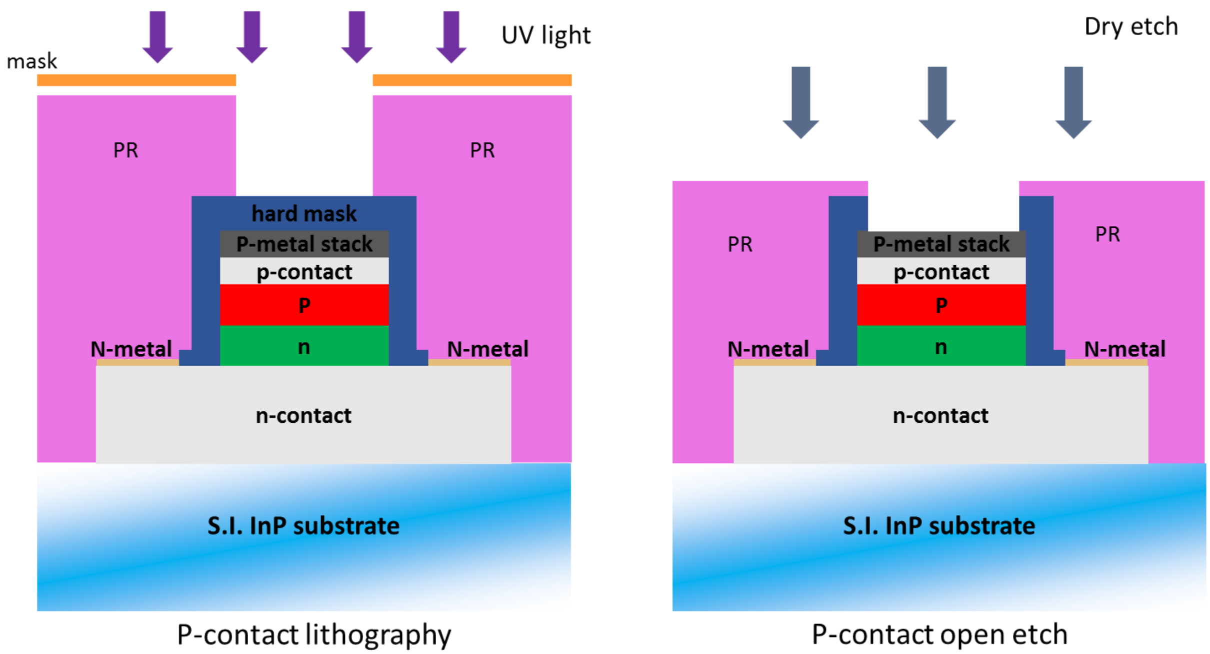

Figure 3-4. Schematic cross section view of P-contact steps. (S.I.: semi-insulating)

3.2.6 *Airbridge and electroplating*

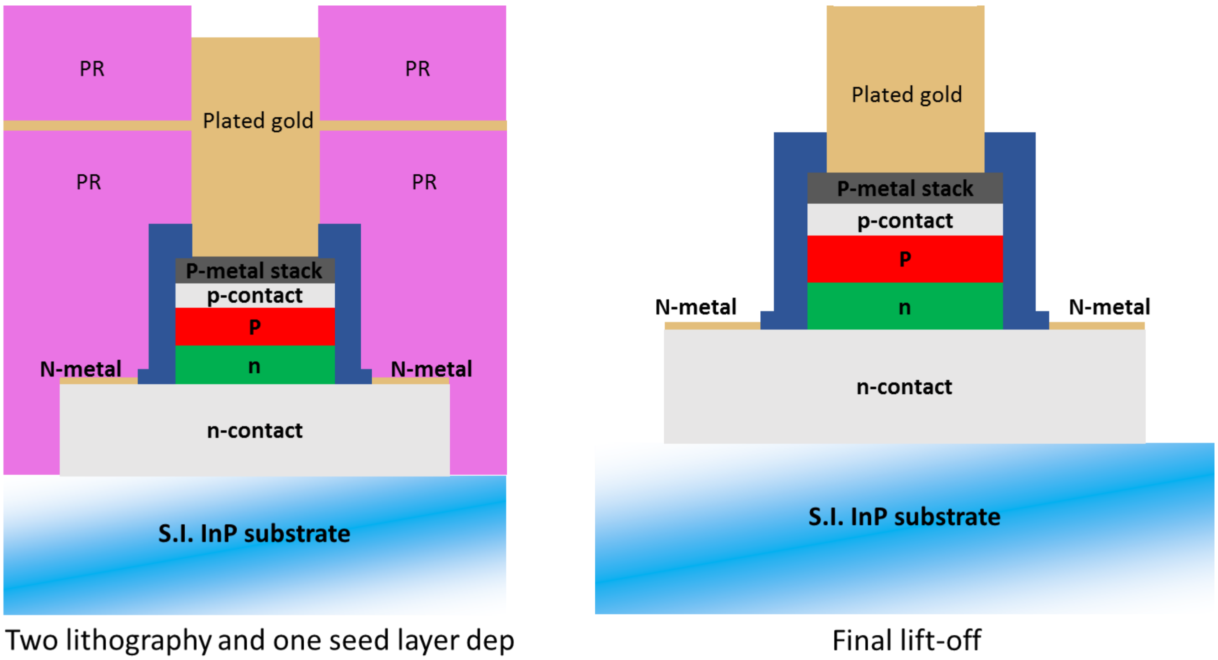

Figure 3-5. Schematic cross section view of air-bridge steps. (S.I.: semi-insulating)

To connect the p-mesa to the RF pads, we use a metal bridge on top of an air gap (referred to as an air-bridge). To realize the air-bridge, two lithography steps are processed in sequence as shown in Figure 3-5. As shown in Figure 3-6, the first lithography buids up the air-gap with photoresist. Then, Ti/Au (15/60 nm) is evaporated as a seed layer. The second lithography is done on top of the first photoresist to open the whole air-bridge region. Next, electroplating is performed with plated gold in the open area. The RF pads are formed with the airbirdge. Finally, lift off is carried out to complete the photodiode fabrication process. Usually, an anti-reflection coating is deposited on the back-side of the wafers to reduce the reflection loss for flip-chip bonded photodiodes.

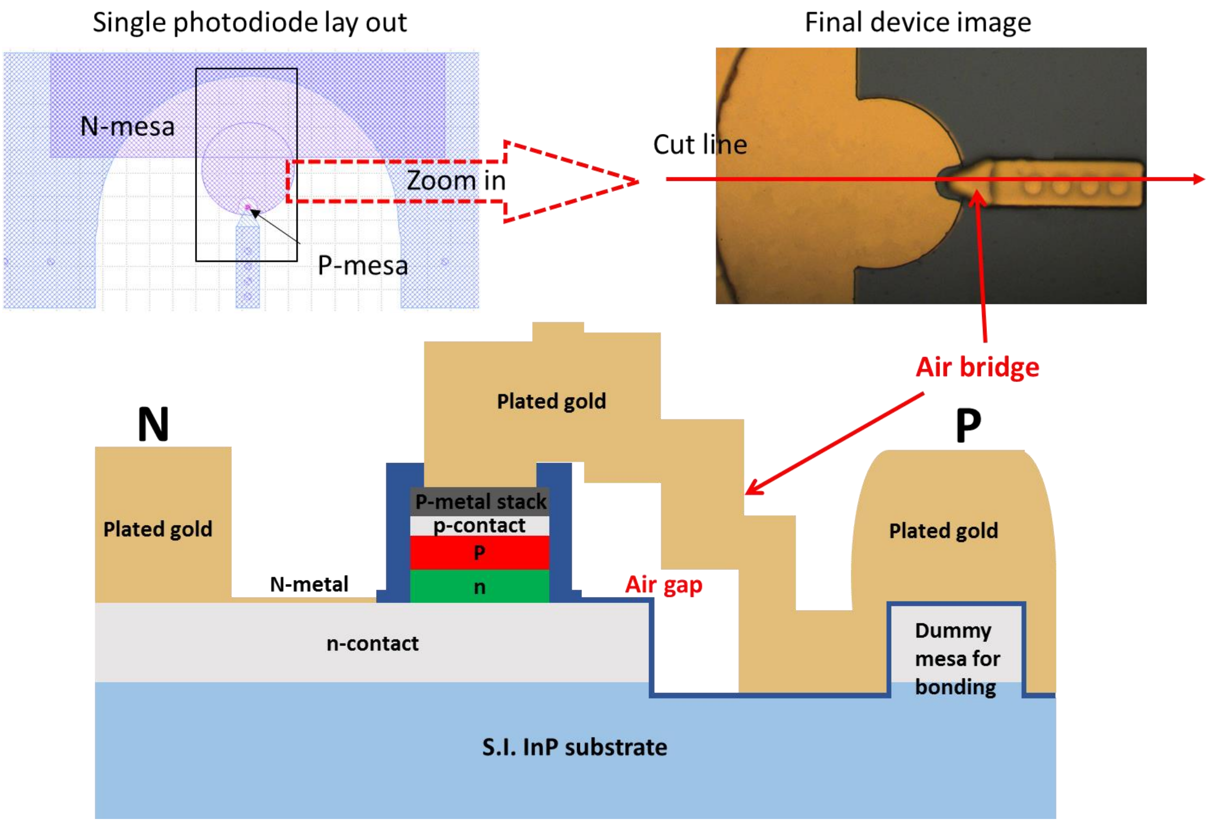

Figure 3-6. Schematic cross section view of an air-bridge. (S.I.: semi-insulating)

3.3 Fabrication of Waveguide Integrated MUTC Photodiode

Most of the fabrication steps for waveguide photodiode are similar to those of normal-incidence photodiodes. Two anditional steps are included to complete the waveguide photodiode fabrication process.

3.3.1 Waveguide etch

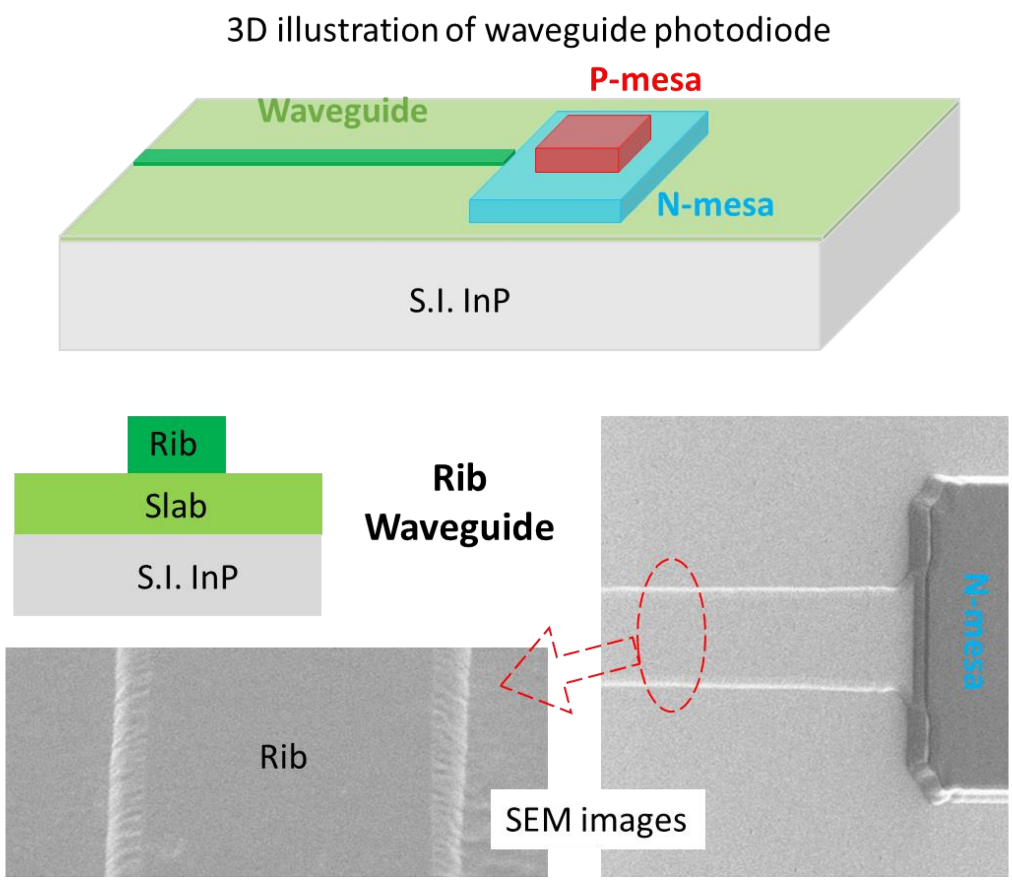

Figure 3-7. Schematic 3D view of a waveguide integrated photodiode. (S.I.: semi-insulating)

The designed optical waveguide is a single mode rib waveguide. A thin rib (~ 300 nm) is fabricated by carefully controlling the dry etch rate. During the lithography, the waveguide layer is patterned with thinner photoresist (~ 1.4 µm) to reduce the degree of side wall taper. After developing, the post bake is skipped in order to maintain the shape of the photoresist, which further reduce the amount of taper. The unbaked photoresist is hardened with a CHF_3 plasma. In order to control the rib thickness, the RIE ICP power is reduced to 100 W to lower the III-V etch rate to ~ 80 nm/min. Figure 3-7 shows a schematic 3D view of a rib waveguide integrated photodiode and SEM images of a fabricated rib wavguide.

3.3.2 Cleaving

In order to better couple light into the single mode rib waveguide, the roughness of the waveguide side wall surface has to be minimized to reduce scattering. Therefore, the cleaved surface with formation of a flat crystal facet is preferable.

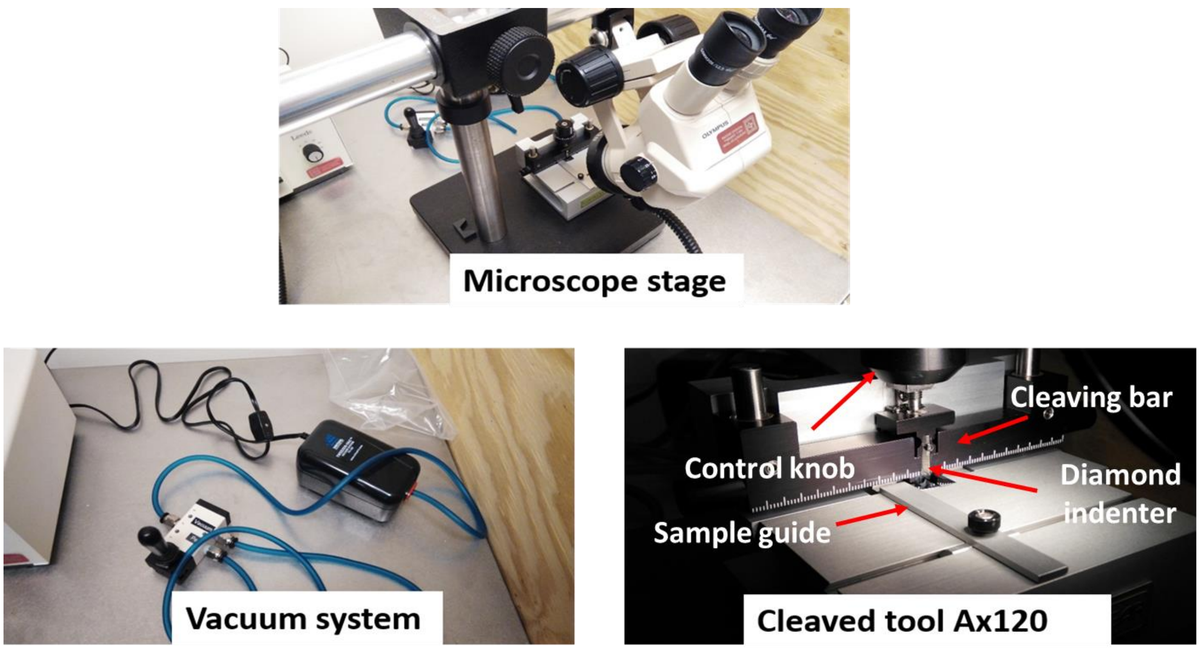

Figure 3-8. Wafer cleaving system.

A Lattice Ax 120 from LatticeGear Corporation is used to perform the cleaving. The cleaved system consists of a microscope, a vacuum system and the main cleaving stage (Ax 120) as seen in Figure 3-8. The Ax 120 includes a diamond indenter with polished face for accurate positioning, position control of indenter with 5 µm step size, cleaving bar with ruled marking and handle, and a sample guide with locking knob.

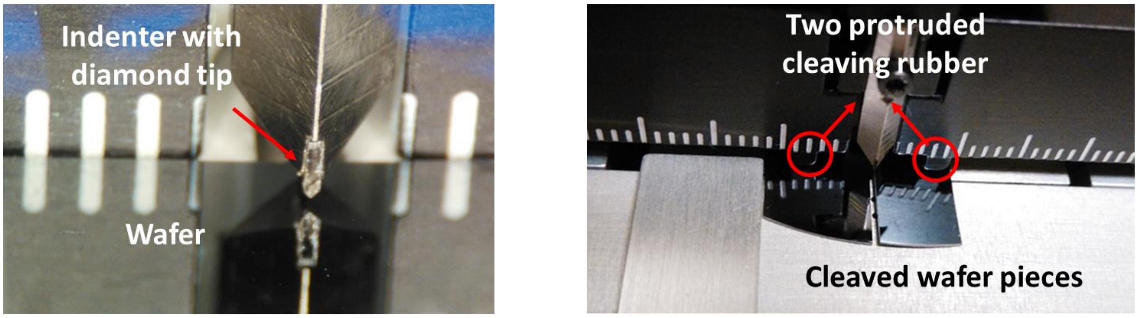

(a) (b)

Figure 3-9. Cleaving processes: (a) Indentation; (b) Cleaving.

During cleaving, the wafer secured to the stage with vaccum. Then, the control kob directs the diamond indenter to indent at a desired location with a little force. After that, the cleaving bar is liftted up and the wafer is extended to sit on top of a metal rod underneath the cleaving bar. There are two protruded cleaving rubber sections on the cleaving bar that are used to break the wafer chips. While the control knob pushes the cleaving bar down to the wafer, the two protruded rubber sections cleave wafer. Figure 3-10 shows InP facet comparison between a cleaved surface and a diced one. Compared with the diced facet, it is obvious that the cleaved surface is flat and free of residues, defects and scratches.

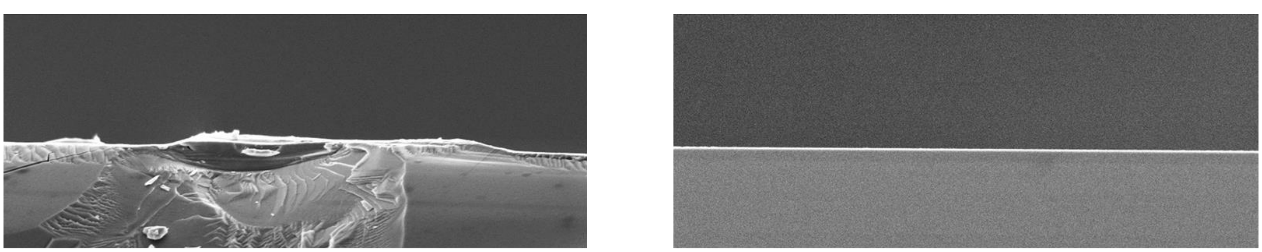

Diced Surface Cleaved Surface

Figure 3-10. Diced and cleaved surfaces comparison.

3.4 Photodiode Characterization

3.4.1 Electrical measurement (Current-Voltage and Capacitance measure)

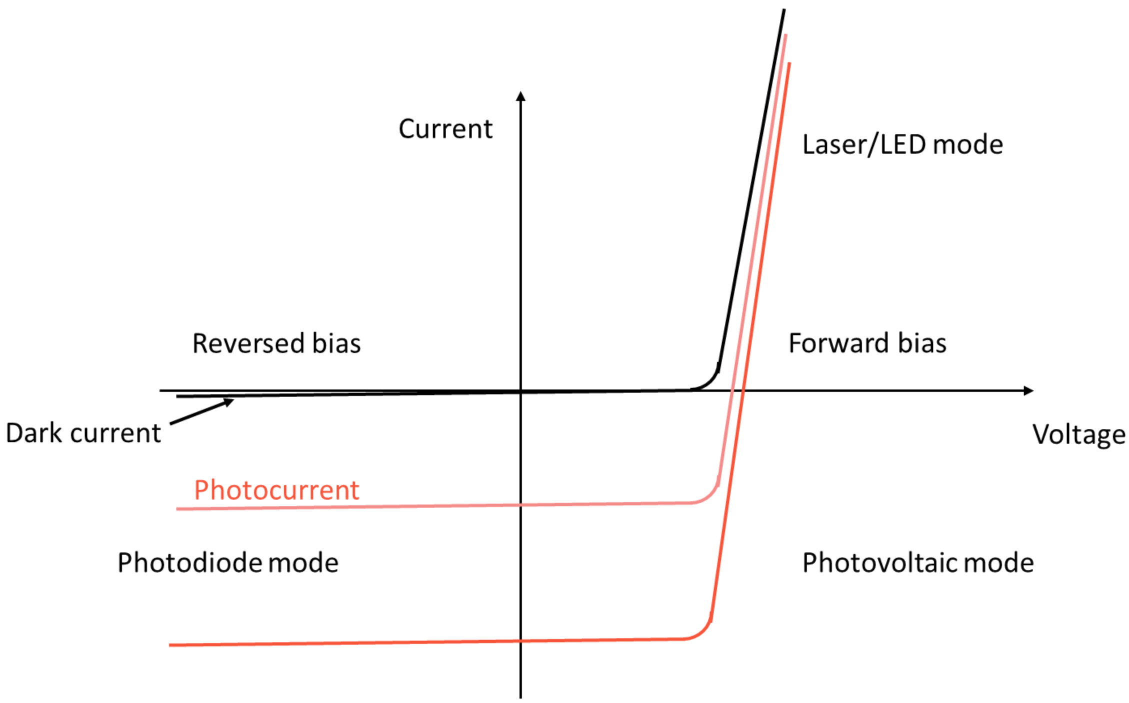

Figure 3-11. Typical diode current voltage curves.

The current voltage (IV) relationship is one of the important charateristices in characterizing a diode. Figure 3-11 shows a typical diode IV curve. Depending on which quadrant a diode operates in, different modes can be achieved including the laser/LED mode, the photodiode mode or the photovoltaic mode. Our photodiode operates under reversed bias and the third quadrant of the IV curve is the region we are interested in. However, the first quardrant can also provide information about the forward current, which yields the photodiode series resistance.

The dark current of the photodiode is the current that flows in the absence of light. Dark current is a noise source. Therefore, low dark current is always preferable. Ideally, the dark current would be zero. However, in practice, at any temperatue above 0 K, there is always generation and recombination current inside the depletion region, which is one component of the dark current. Another primary component of dark current is the surface leakage. Generation/recombination occurs through traps associated with the dangling bonds on the surface after fabrication. Other effects that contribute to dark current are trap-assisted and band-to-band. By analyzing the IV curve of a photodiode, current transport mechanisms can be determined.

The capacitance-voltage (CV) measurement is an effective way to characterize the photodiode junction capacitance since a reverse biased photodiode acts as a capacitor. The junction capacitance C_{pn} is an important parameter. For example, the RC time constant is an important factor in the bandwidth.

(a) (b)

Figure 3-12. IV and CV measurement tools: (a) Parameter analyzer (b) LCR meter.

The IV curve measurement is carried out with HP 4156B semiconductor parmeter analyzer. A quick photo response can be checked with microscopic lamp. The CV measurement is performed with HP 4275A Multi-Frequency LCR meter.

3.4.2 S-parameter measurement

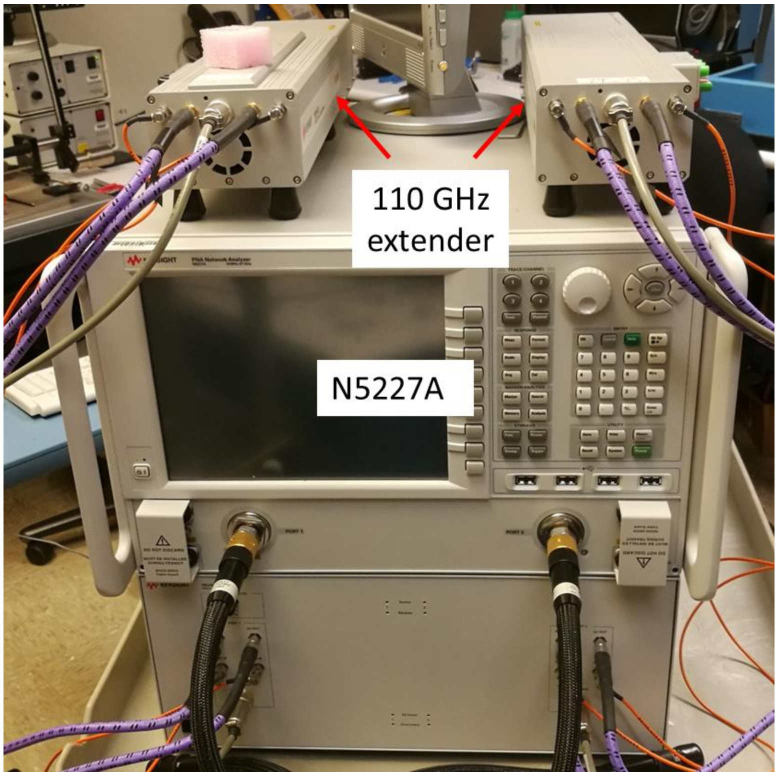

Figure 3-13. Keysight PNA network analyzer.

One-port S parameter measurements are performed with a Keysight PNA network analyzer that is capable of characterizing frequency up to 110 GHz. The network analyzer consist of two parts: the N5227A that measures frequency from 10 MHz to 67 GHz, and the extender arms that can measure frequency from 67 GHz up to 110 GHz. A G-S-G microwave probe along with bias tee, coaxial cables and adapters are used for one-port S11 measurements. Before the measurement, an on-wafer calibritaion is carried out to move the reference plane to the microwave probe tip. The sweep resolution can be adjusted depending on the frequency range. We typically use 1601 points for frequency up to 110 GHz. The on-wafer calibration is conducted with a CS-250 substrate kit which includes open, short and matched load calibration. Then the photodiode is probed with the microwave probe at reversed bias, and the S11 reflection data is received by the network analyzer. With the measured S11 data, the photodiode parameters, such as series resistance, series inductance and junction capacitance can be extracted by fitting the S11 with a circuit model.

3.4.3 Reponsivity

Responsivity measures the photodiode electrical ouput in response to an optical input. For a photodiode with high linearity, the electrical signal always follows the optical signal linearly. The slope of the linear response is the responsivity that is usually expressed in units of amperes per watt (A/W). The responsivity quantifies how efficiently a photodiode converts the optical signal to an electrical signal. The external quantum efficiency (EQE), η_e, denotes the ratio of the number of photogenerated carriers collected to the total number of incident photons. Assuming light travel through an absorber with thickenss of d without reflection back and all the photogenerated carriers are collected , the EQE can be expressed as:

$$\eta_e = (1 - R_{ref})(1 - e^{-\alpha d})$$

where R_{ref} is the surface reflectivity, α is the absorption coefficient of the absorber and d is the absorber thickness. The respsonvity relates to the EQE, η_e, by the relation

$$R = \eta_e \frac{q\lambda}{hc} \approx \eta \frac{\lambda_{(\mu m)}}{1.24}\ (A/W)$$

Eq. 3-1

where q is the elementary charge of $1.6022 \times 10^{-19}\ C$, λ is the light wavelength, h is Planck's constant with value of $6.626 \times 10^{-34}\ J \cdot s$ and $c = 3.0 \times 10^{8}\ m/s$ is the speed of light in vacuum.

Ways to improve the responsivity or EQE include reducing the surface reflection by introducing an anti-reflection coating layer; increasing the absorber thickness; or implementing a resonant-cavity.

The measurement of responsivity will be discussed in section 3.4.3.

3.4.3 Bandwidth and RF Saturation Measurement

The photodiode frequency response and RF saturation performace are characterized with an optical heterodyne setup. Figure 3-14 illustrates the measurement set-up. Two MHz linewidth distributed feed back (DFB) lasers with wavelength near 1550 nm are used to provide a heterdyned RF optical signal. The frequency of one laser is tunable over wide frequency range by controlling the laser temperature. In this way, the optical beat frequency can be swept from DC to hundreds of GHz. To achieve 100% modulation depth, the output power of the DFB lasers needs to be matched by controlling the injection current. Polarization controllers are used to align the two optical signals to ensure that 100 % modulation can be achieved. The mixed optical signal is splitted into two arms. One arm which is further split into two arms is used to monitor the beat frequeny. At frequency lower than 50 GHz, a 50 GHz photodetector along with an HP8565E spectrum analyzer (9 kHz ~ 50 GHz) monitors the beat signal. For RF frequency above 50 GHz, the beat signal can be monitored with an optical wavelength meter with 0.001 nm resolution. In another arm, the heterodyned optical signal is amplified with an Erbium doped fiber amplifier (EDFA), attenuated by Agilent 81577 A optical attenuator and focused through a lens fiber on the photodiode. The electrical signal from the photodiode is detected with GSG microwave probe. Through a bias tee, a source meter can provide a DC bias on the photodiode and reads out the DC photocurrent as well. The AC signal transmitted through the bias tee is detected with a Rohde-Schwarz power meter with frequency up to 110 GHz. A computer with a labview program is responsible for controlling the measurement progress by having standard GPIB cables connected to all the equipment as seen in Figure 3-13.

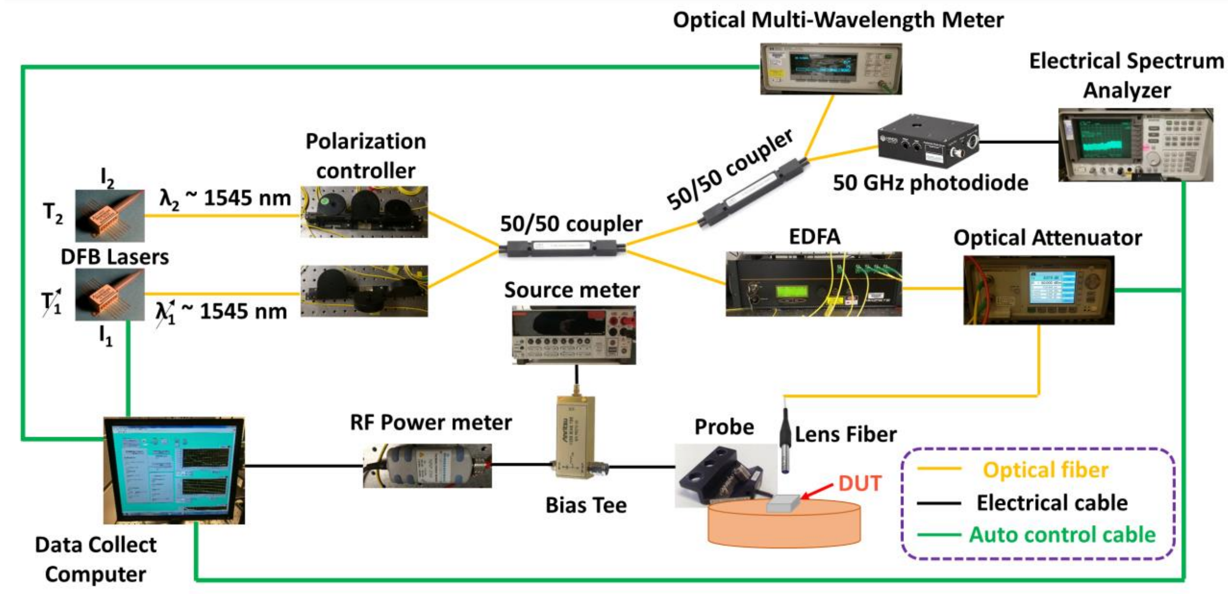

Figure 3-14. Optical heterodyne setup for bandwidth and saturation measurement. (DUT: device under test)

During the bandwidth measurement, the DC responsivity can be calculated by comparing the optical input from the attenuator with the DC photocurrent read from the source meter.

The photodiode RF saturation is measured with the same setup as that used in the bandwidth measurement. 100 % modulation is used during the measurement. Instead of sweeping the RF frequency, the optical beat RF signal is fixed at certain frequency and the RF output power is recorded while the photocurrent gradually increases to the point where 1 dB compression is reached.

Chapter 4. 100 GHz High Power Back-illuminated Normal-Incidence MUTC photodiode

4.1 Introduction

High speed photodiodes over 100 GHz bandwith with large saturation current are key components for high-speed optical communication systems and photonic microwave applications. Photomixing generation of millimeter wave (mmW) with a large-saturation-current photodiode can provide not only extremely wide bandwidth, which enables very high data rates compared with coaxial cables, but also good quality signals with relatively low phase noise compared with mmW electrical oscillators. Therefore, it is essential to design a photodiode with speed over 100 GHz while maintaining large saturation current. The normal incidence MUTC was designed first owing to its advantage of simple epitaxial design, better coupling efficiency and uniform absorption with high saturation current.

In this chapter, the epitaxial design of the back-illuminated MUTC photodiode that achieved 100 GHz bandwidth is discussed. Then, fabrication procedure and experimental results are described. Bandwidth limiting factors are analyzed using an analytical model that employs parameters extracted from S11 measurements. To achieve high speed, a high impedance transmission line was incorparted to form inductive peaking in order to improve the bandwidth. With the extracted parameters, an optimized CPW was designed to flatten the frequency response as well as to improve the power performance at 100 GHz. To improve the thermal dissipation capacity, all devices were filp-chip bonded onto high thermal conductivity Aluminum nitride substrate.

4.2 Device Epitaxial Design

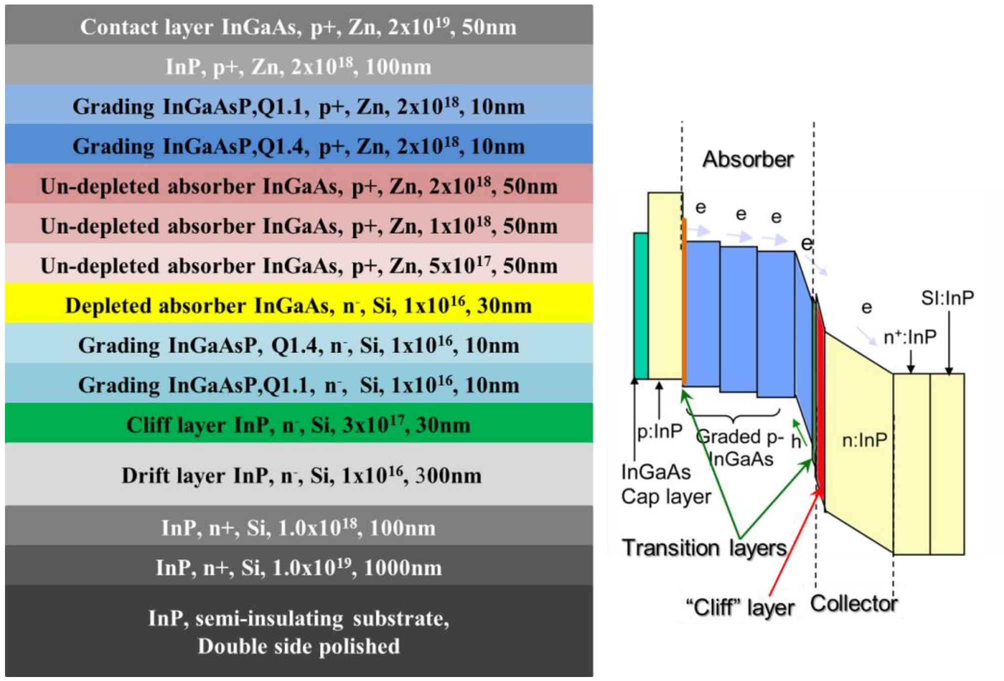

Figure 4-1. Epi-layer design and band diagram of MUTC. (SI: semi-insulating)

Back-side illuminated photodiodes were fabricated on a 2 inch InGaAsP/InP wafer. The epitaxial layer design together with the band diagram is shown in Fig. 4-1. The layers were deposited and in situ-doped with zinc (p-type) and silicon (n-type) by metal organic chemical vapor deposition on semi-insulating InP substrate. First, a 1000 nm heavily doped n-type InP contact layer was deposited followed by a 300 nm lightly n-doped (1×10^{16} cm^{-3}) charge compensated drift layer. A 30 nm-thick n-doped (3×10^{17} cm^{-3}) InP cliff layer in combination with two 10 nm-thick lightly n-doped InGaAsP quaternary layers were used to maintain high electric field in the depleted absorber and to suppress charge accumulation at the heterojunction interfaces [4-1]. This was followed by a 30 nm unintentionally doped depleted absorber. Three 50 nm p-type undepleted absorber layers with step grading of 5×10^{17} cm^{-3}, 1×10^{18} cm^{-3}, 2×10^{18} cm^{-3} create a quasi-electric field that aids electron transport. Finally, two 10 nm-thick lightly p-doped InGaAsP quaternary layers were deposited to assist hole collection and block electrons. The p-type contact was formed using 150 nm heavily p-doped InP and InGaAs. In contrast to the charge-compensated MUTC reported in [4-1], the absorber layer and drift layer were decreased to 180 nm and 300 nm, respectively, for the purpose of reducing the electron transit time.

4.3 Device Fabrication

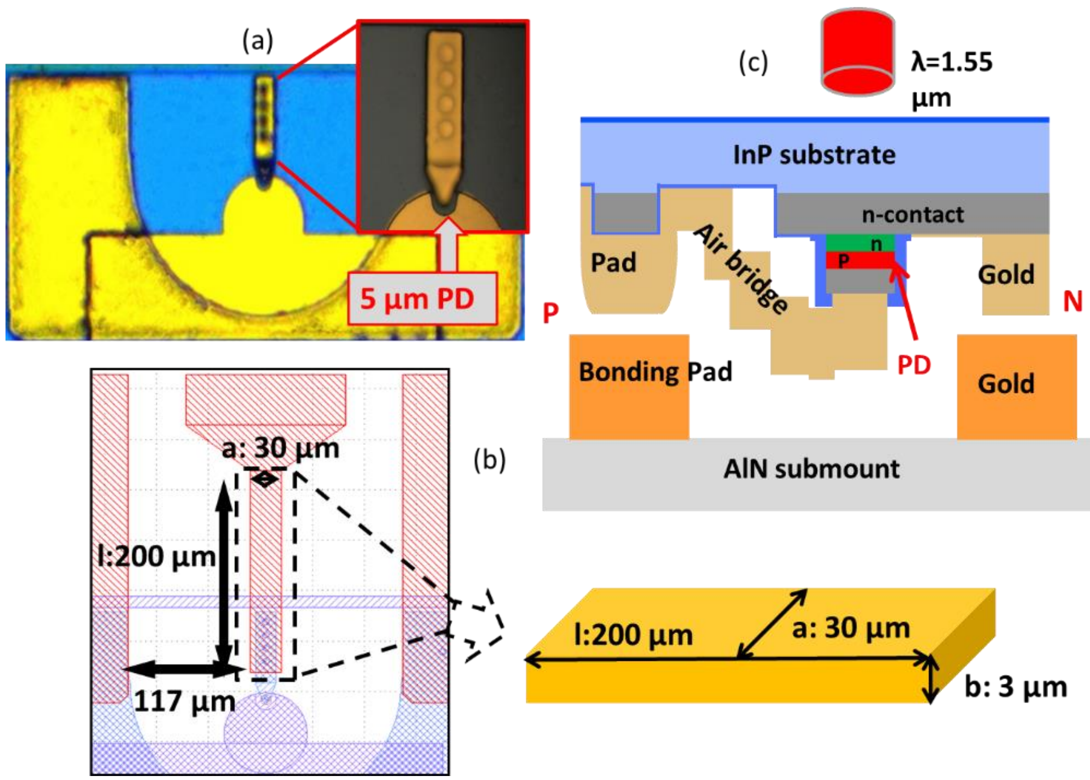

Figure 4-2. (a) Photodiode with 5 µm-diameter (b) Layout of high impedance transmission line on sub-mount and a rectangular bar for illustration of transmission line dimensions (c) Flip-chip bonding scheme.

The MUTC photodiodes were fabricated with diameters from 5 µm to 20 µm. Figure 4-2 (a) shows an optical microscopic picture of a 5 µm-diameter photodiode before flip-chip bonding. A double mesa process was used to fabricate the devices. The first mesa-etch stopped at the heavily doped InP n-contact layer in order to define the p-mesa. The n-mesa was formed later by dry etching into the semi-insulating InP substrate. AuGe/Ni/Au and Ti/Pt/Au were used for n-metal and p-metal contacts, respectively. The Ti and AuGe layers provide good adhesion to InGaAs and InP. The Pt and Ni layers prevent Au penetration into the semiconductor. The photodiodes were connected to gold-plated bonding pads through an airbridge. After back-side polishing, a 250 nm-thick SiO_2 anti-reflection coating was deposited to reduce reflection at 1.55 µm. Fig. 4-2 (c) illustrates flip-chip bonding. In the flip-chip bonding process, a chip with 6 photodiodes was bonded onto an AlN submount by Au-Au thermo-compression at 340 °C. Previously, our group showed that flip-chip bonded devices on AlN exhibited 200% improvement in DC power dissipation compared to similar devices that were not bonded to high-thermal-conductivity submounts [2-12]. To further increase the bandwidth, a high impedance transmission line, which also incorporates the bonding pads, was fabricated on the chip and the submount as seen in Fig. 4-2 (b). The characteristic impedance of the transmission line is 96 Ω. The inductive peaking provided by the transmission line increases the bandwidth for a given device area.

4.4 Device Characterization

4.4.1 Electrical parameters

The dark current versus bias voltage characteristics are shown in Fig. 4-3. Typical dark currents were in the range 10^{-8}~10^{-7} A at -5 V bias. The fact that the dark current scales with photodiode diameter suggests that it is dominated by a surface leakage current, that, most likely, originates from surface damage during dry etch.

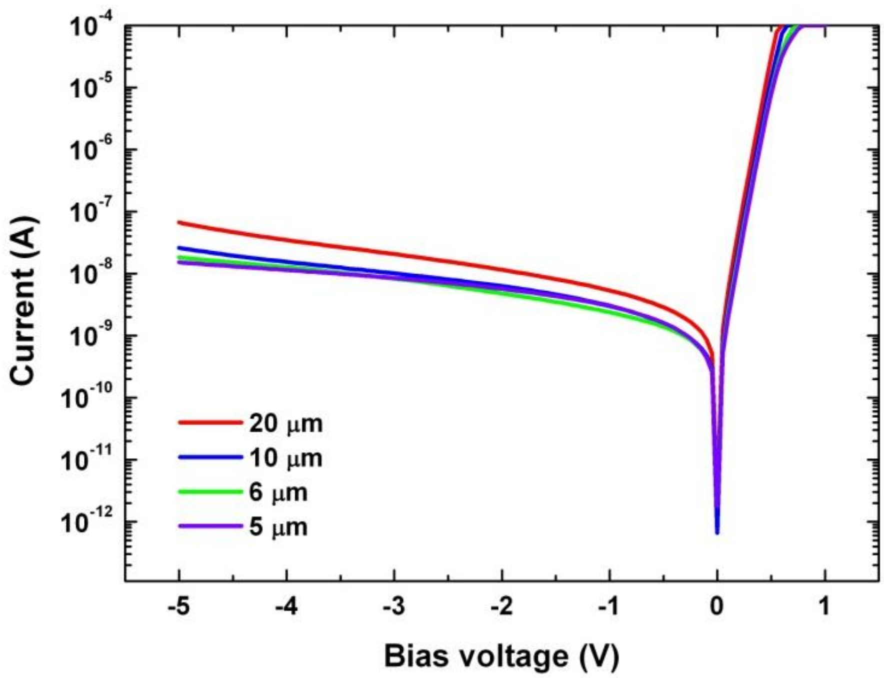

Figure 4-3. Dark current versus voltage for photodiodes with diameters from 5 µm to 20 µm.

After the chips were flip-chip bonded, the photodiode capacitance ($C_{photodiodes}$), i.e. the sum of the junction capacitance, C_{pn}, and the parasitic capacitance, C_{st}, was measured at 100 KHz using a multi-frequency LCR meter. As seen in Fig. 4-4 (a), as the reversed bias increases, $C_{photodiodes}$ initially decreases and then saturates when the drift layer is fully depleted (above 2 V reverse bias).

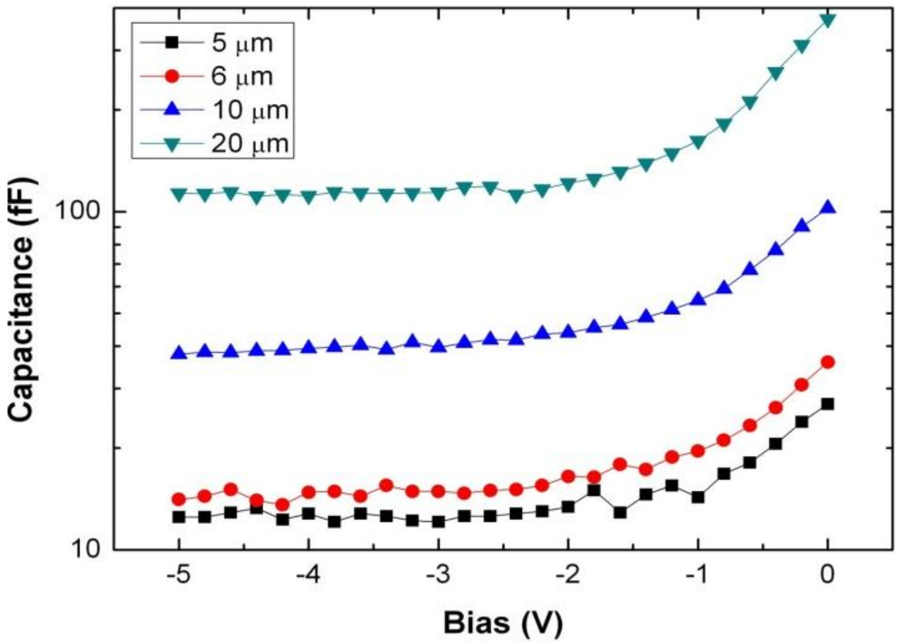

(a)

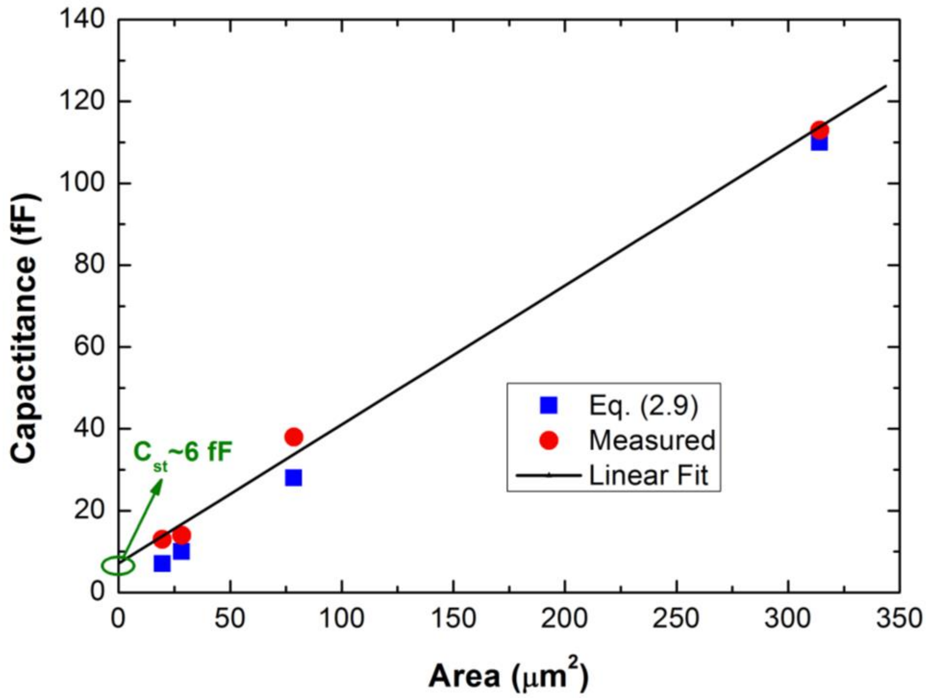

(b)

Figure 4-4. (a) Measured capacitance as a function of bias voltage for different device diameters; (b) Comparison of measured and estimated capacitances.

The parasitic capacitance was extrapolated by plotting the measured capacitances versus normalized areas (Fig. 4-4 b). A C_{st} of 6 fF was determined from the intercept of the linear fit. The parasitic capacitance is almost as large as C_{pn} of a 5 μm-diameter photodiodes, which suggests that parasitics limit the RC component of the bandwidth in the smallest photodiodes. Eq. (2.9) was used to calculate the C_{pn} with dielectric constant of InP (13.9), photodiode active area, and depletion width (350 nm), respectively. After subtracting C_{st} from the measured capacitance, the C_{pn} shows good agreement with the values predicted by Eq. (2.9).

4.4.2 Parameter extraction with S11

The scattering parameter S11 of flip-chip bonded devices was measured using a PNA Network Analyzer up to 100 GHz. Parameter fitting was done using advanced design system (ADS) software with the equivalent circuit shown in Fig. 4-5. R_s and R_p represent the series resistance and the junction resistance, and L_s denotes the series inductance, which arises primarily from the air bridge that connects the p-mesa and the bonding pads. The electromagnetic simulator in ADS was used to compute the S parameters of the high-impedance coplanar waveguide (CPW), which was added in the circuit model to fit the device design (Fig. 4-2 b).

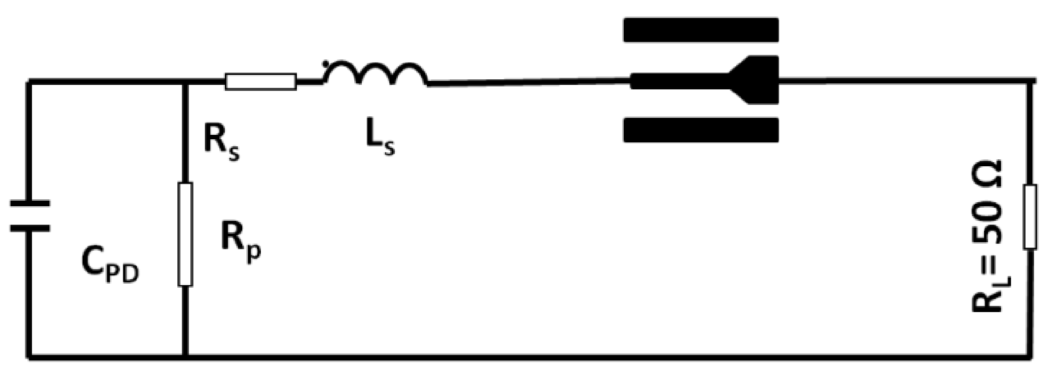

Figure 4-5. Circuit model of flip-chip-bonded photodiodes for S11 fitting.

Table 4-1. Measured and calculated parameters. (Note that C_{st} was subtracted from the measured and extracted capacitances)

Diameter (μm)	Eq.(1) C_{pn} (fF)	Measured C_{pn} (fF)	Extracted from S11 fitting		
			C_{pn} (fF)	R_s (Ω)	L_s (pH)
5	7	7	6	6	66
6	10	8	8	6	60
10	28	32	27	6	40
20	110	107	106	5	15

Figure 4-6 shows the measured S11 on Smith charts and the fitting results for four photodiodes with different diameters under a reverse bias of 3.5 V. Table 4-1 summarizes the fitted parameters as well as the measured and calculated C_{pn} (from Eq. (2.9)). Note that R_p extracted from S11 is typically on the order of 200 MΩ and is not listed in the table. From Table 4-1, R_s is independent of device diameter, which indicates small contact resistance and that bulk resistance may dominate the total series resistance. The low value of R_s may be attributed to the 340 °C anneal prolonged to improve contact resistance during flip-chip bonding. The extracted inductances, L_s, decrease as device diameter increases. This is expected, since the width of the air bridge scales with photodiodes diameter. A similar trend is expected for a single wire as its diameter increases.

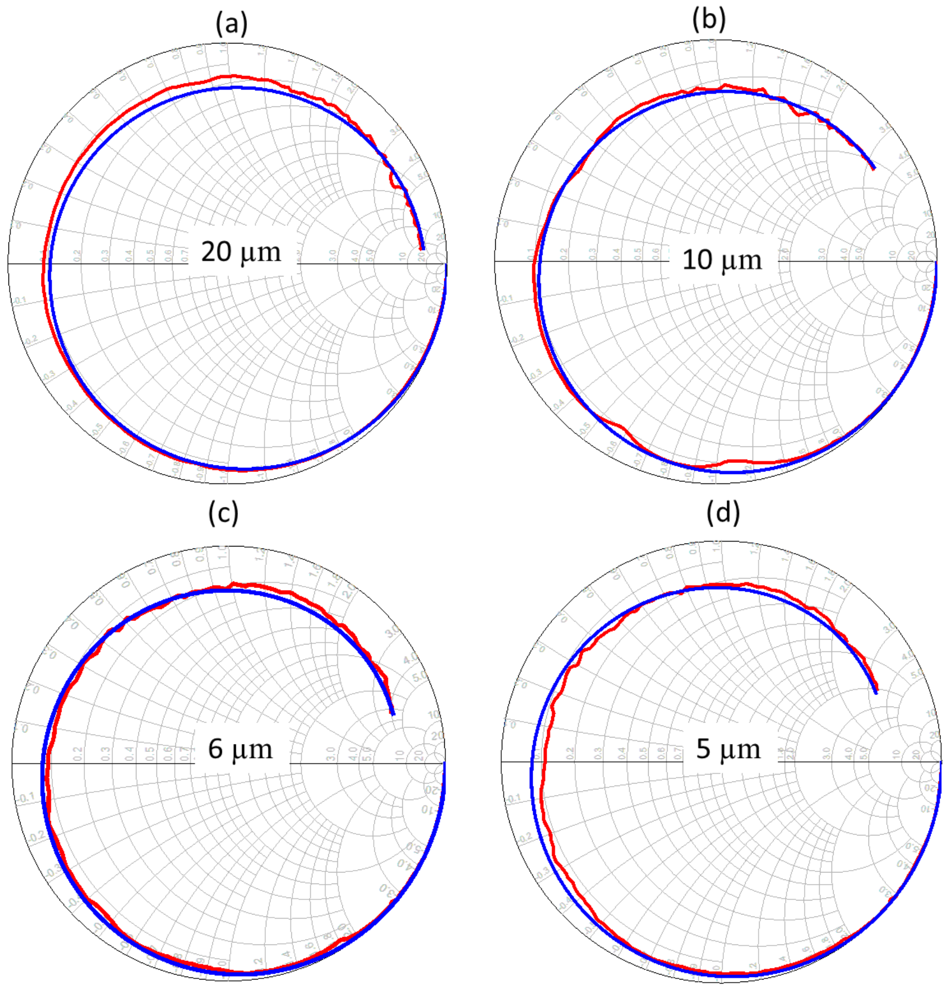

Figure 4-6. Measured and fitted (smooth line) S11 data for devices diameters of a: 20 μm (fitted 10 MHz ~ 80 GHz), b: 10 μm (fitted 10 MHz ~ 80 GHz), c: 6 μm (fitted 10 MHz ~ 100 GHz), d: 5 μm (fitted 10 MHz ~ 100 GHz) at -3.5 V bias.

4.4.3 Device Frequency Response

The setup in Fig. 3-14 is used for bandwidth measurement. Additionally, A lensed fiber with 8 µm spot diameter was used to couple light into the photodiodes. The RF power was detected using a calibrated R&S power meter NRP-Z58 with a frequency range from DC to 110 GHz. A calibrated 110 GHz bias tee and a W-band 1.00 mm semi-rigid coaxial cable were used. The typical responsivity was 0.17 A/W at 1.55 µm wavelength and did not depend on the photodiode diameter. During the measurements, the lensed fiber was pulled back to a point where the responsivity dropped by ~ 50% in order to achieve uniform illumination. To prevent premature thermal failure, both bandwidth and saturation measurements were carried out on a thermo-electric (TE) cooler at 0 °C.

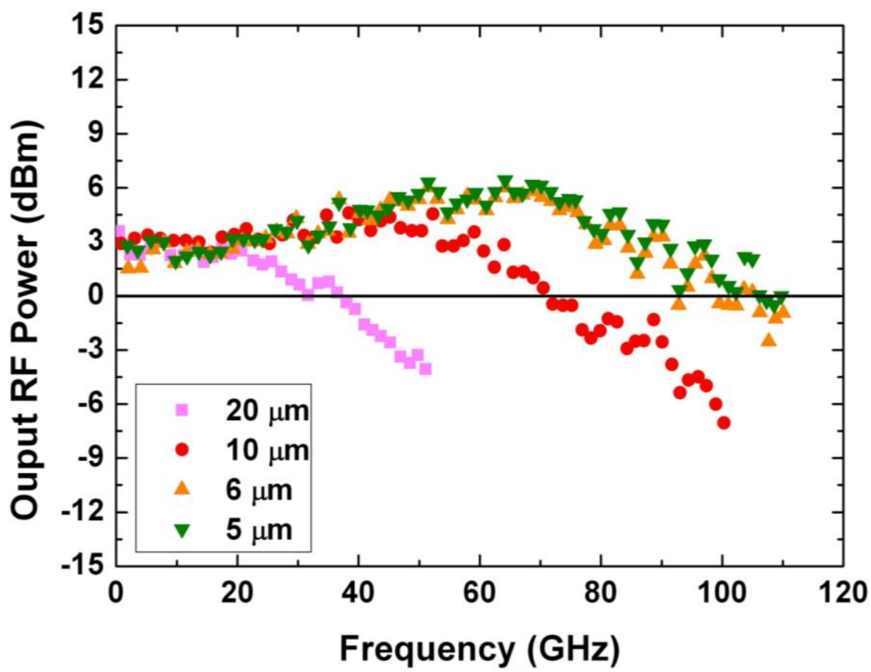

(a)

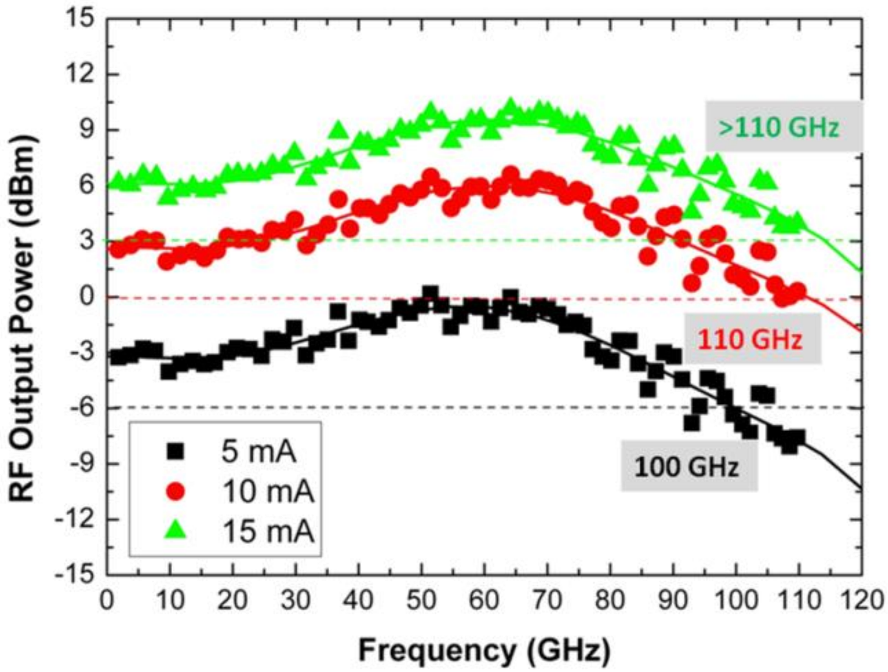

(b)

Figure 4-7. Measured frequency responses: (a) 5, 6, 10, and 20 μm-diameter photodiodes; (b) a 5-μm diameter photodiode with different photocurrent (solid lines are polynomial fitting curves).

The bandwidth of photodiodes with various diameters measured at 10 mA average photocurrent and 4 V reverse bias is shown in Fig. 4-7 (a). Larger bandwidth was observed for smaller diameter photodiodes due to increased RC limited bandwidth. Fig. 4-7 (b) shows the frequency responses of a 5 μm-diameter device at reverse bias of 3.5 V with 5 mA, 10 mA, and 15 mA photocurrent; the bandwidth is greater than 110 GHz at 15 mA. As reported in [2-8], at high current levels, bandwidth enhancement is observed. This is attributed to the fact that the photo-generated carriers induce an electric field that assists electron transport in the undepleted absorber. The peaking effect from the high impedance transmission line was observed in the range 60 ~ 70 GHz, which improves the power level up to 4 dB at 65 GHz.

To assess the bandwidth limiting factors, the frequency response model including both the RC time-limited and transit time-limited components was calculated using:

$$\frac{I(\omega)}{I(0)} = \underbrace{\left(\frac{1}{1-\omega^2 L_{total} C_{PD} + j\omega C_{PD}(R_L + R_S)}\right)}_{\text{RC component}} \times \underbrace{\left(\left[1-\exp(j\omega\tau)\right]\frac{2}{\omega^2\tau^2} - \frac{2}{j\omega\tau}\right)}_{\text{Transit time component}}$$

Eq. (4.1)

In the RC term, R_L is the load resistance (50 Ω). R_s was assumed to be small compared with the load resistance. L_{total} is the total series inductance including both the inductance from the air-bridge, L_s, and the transmission line, L_{HTRL}. A self-inductance model for a rectangle bar was used to estimate the inductance of the center line (Fig. 4-2 b) of the transmission line [4-2]:

$$L_{HTRL} = \frac{\mu_0}{2\pi} l \left(\ln\left(\frac{2l}{R}\right) + \frac{R}{l} - 1\right)$$

Eq. (4.2)

where l is the length of the transmission line (200 μm), μ_0 is the vacuum permeability. R represents the geometric mean of the transmission line cross section and is proportional to the lengths of the two sides:

$$R = 0.2235(a + b)$$

Eq. (4.3)

where a and b are the width (30 μm) and thickness (3 μm) of the transmission line, as illustrated in Figure 4-2 b. Here R = 7.15 μm and, therefore, L_{HTRL} = 122 pH.

For the transit time-limited frequency component in Eq. (4.1), τ=3.45 ps is the time for an electron to transit the depletion width (380 nm), assuming a constant electron drift velocity of 1.1×10^7 cm/s, corresponding to an electric field of 80 kV/cm, [4-3]. Since holes in the depleted absorber travel a very short distance (~30 nm in the depleted absorber) compared with that of the electrons, only the electron transit time is considered in order to simplify the analysis.

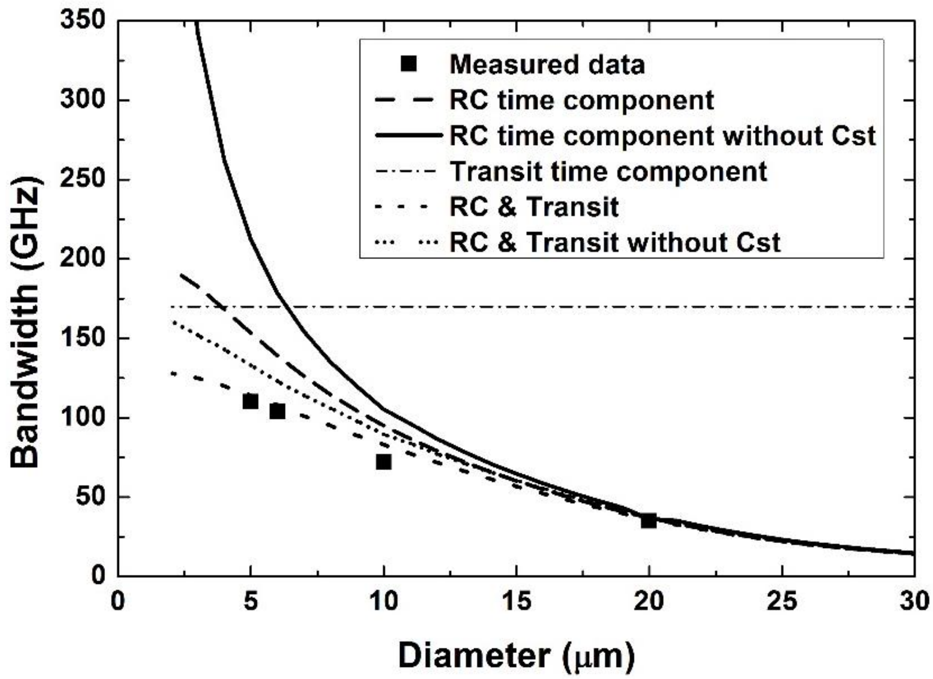

Figure 4-8. Measured and simulated bandwidths.

The simulated and measured 3 dB bandwidths are plotted in Fig. 4-8. Even without consideration of carrier transport in the un-depleted absorber, good agreement between measured and modeled bandwidths is obtained. We note that the RC limitation prevails for all diameters. If parasitic capacitance is excluded from the model, as illustrated in Fig. 4-8, larger devices are still constrained by RC limited bandwidth, while the carrier transit time is the primary limitation for photodiodes with diameters less than 10 μm. If the parasitic capacitance can be reduced, greater than 130 GHz bandwidth can be achieved for a 5 μm-diameter device. Therefore, as suggested from the model, two ways can be utilized to enhance the overall bandwidth. The first way is to optimize the flip-chip bonding process to reduce the parasitic capacitance. For example, the p-mesa can be directly bonded onto the sub-mount without an air-bridge. The second approach is to improve the transit time-limited bandwidth through reducing the absorber thickness and slightly adjusting the drift layer thickness.

4.4.4 RF Saturation Characteristics

Table 4-2. Bandwidth and RF power for different size photodiodes.

<table>
<tr><th rowspan="2">Size (µm)</th><th rowspan="2">Max Bandwidth (GHz)</th><th colspan="4">Max RF Output Power (dBm)</th></tr>
<tr><th>50 GHz</th><th>75 GHz</th><th>100 GHz</th><th>110 GHz</th></tr>
<tr><td>5</td><td>112</td><td rowspan="3">×</td><td>×</td><td>6.9</td><td>5.5</td></tr>
<tr><td>6</td><td>106</td><td>×</td><td>9</td><td>7.8</td></tr>
<tr><td>10</td><td>78</td><td>13</td><td>9.6</td><td rowspan="2">×</td></tr>
<tr><td>20</td><td>40</td><td>14.3</td><td colspan="2">×</td></tr>
</table>

Using the above described bandwidth measurement set-up, saturation was characterized by measuring the RF output power as a function of average photocurrent at a fixed frequency. Table 4-2 summarizes the maximum bandwidths and RF output powers at different frequencies for various photodiodes diameters. Note that the RF power of the 20 µm-diameter photodiodes did not reach saturation at 50 GHz due to the limited input optical power in the experimental setup. Figure 4-9 shows the RF output power of 6 µm- and 10 µm-diameter photodiodes versus average photocurrent. Photodiodes of 10 µm-diameter achieved 9.6 dBm at 100 GHz and 13 dBm at 75 GHz, while the 6 µm-diameter photodiodes reached 9 dBm at 100 GHz and 7.8 dBm at 110 GHz. We observe that the power increases superlinearly with increasing photocurrent before it saturates. This is due to the self-induced field that enhances the bandwidth at higher photocurrent. The 10 µm-diameter device saturates at 49 mA photocurrent. At 100 GHz, the 6 µm-diameter device exhibited lower saturation photocurrent of 27 mA.

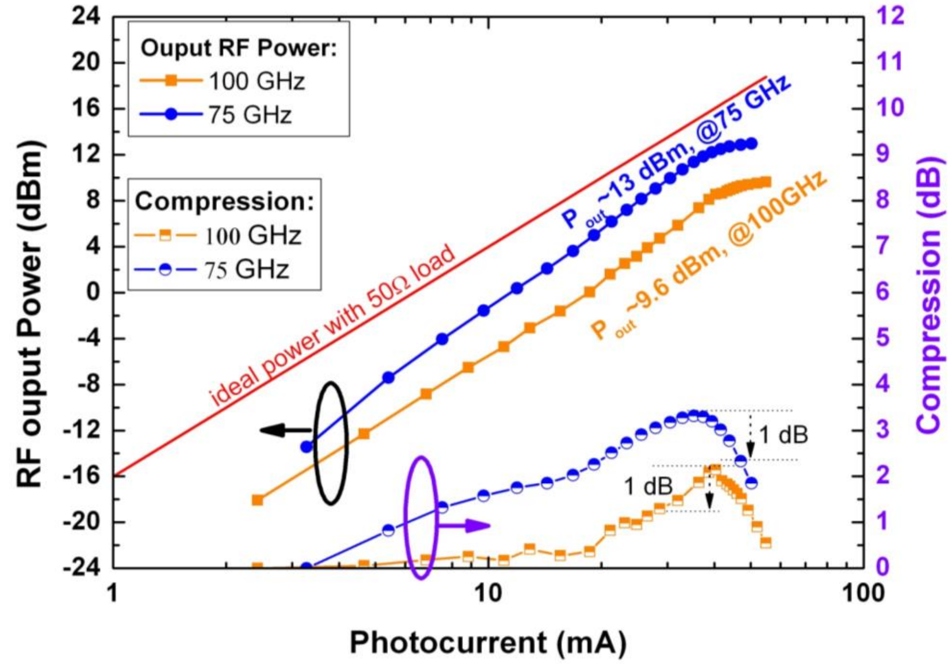

(a)

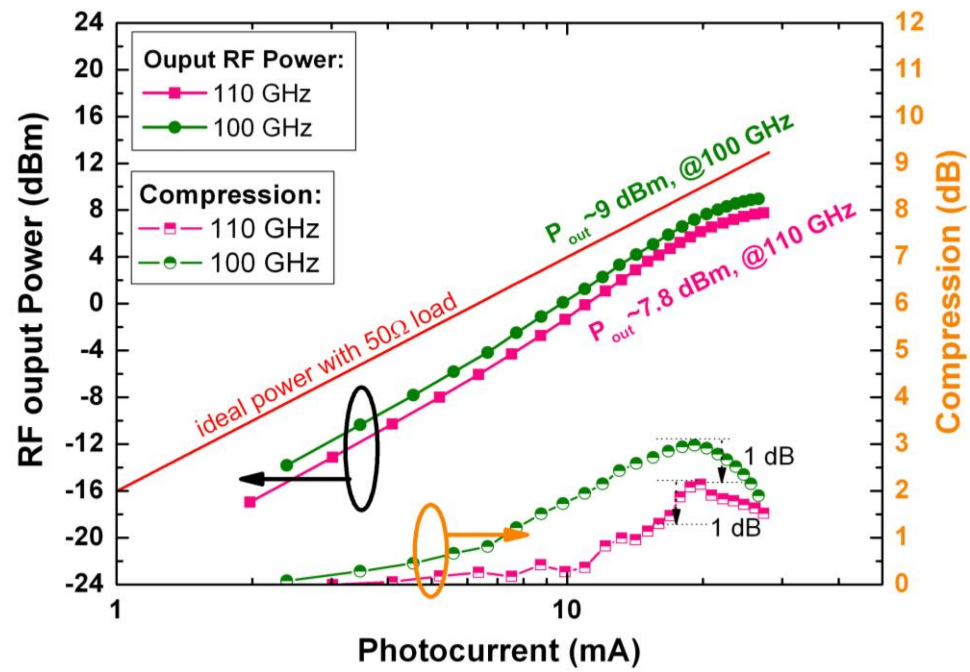

(b)

Figure 4-9. RF output power and RF power compression versus average photocurrent for (a): 10 μm at 3.5 V; (b) 6 μm at 4 V.

The voltage dependence of the RF output power was investigated by measuring saturation at different reverse bias as seen in Fig. 4-10. As photocurrent increases, the space-charge effect causes an electric field reduction in the depletion region, which impedes carrier transport and ultimately leads to saturation. To mitigate the space-charge effect the reverse bias voltage can be increased to the point where either thermal failure or junction breakdown occurs [4-4]. 5-μm diameter photodiodes suffered thermal failure when the average DC photocurrent was ~20 mA under reversed bias of 3.5 V.

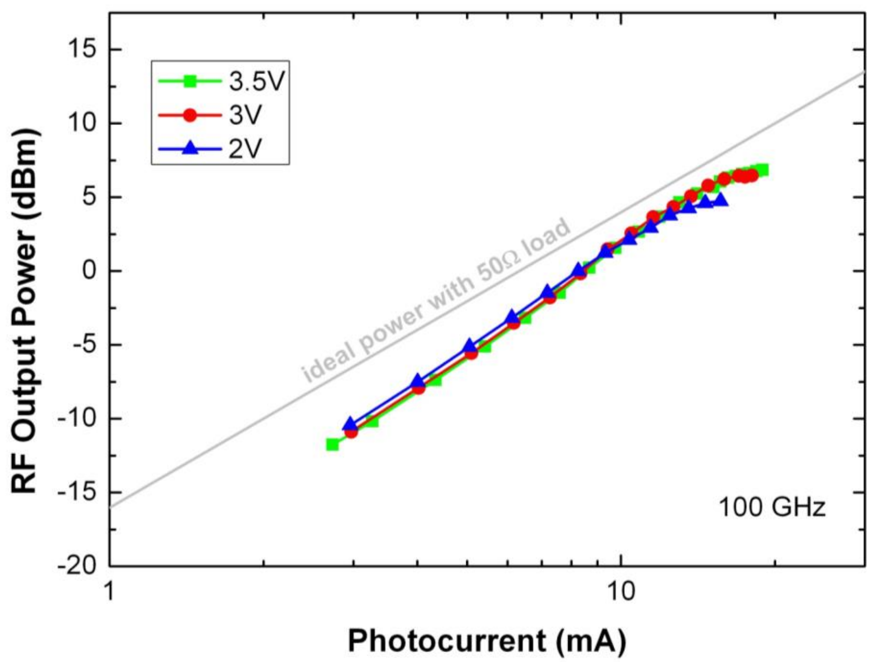

Figure 4-10. RF power versus average photocurrent at different bias for a 5 μm-diameter device at 100 GHz.

4.5 Optimized CPW for bandwidth improvement

As seen in Fig. 4-7, with the initial CPW design, the frequency response of the 5 and 6 μm devices peaks near 70 GHz, which can create issues for the applications that require a photodetector with relatively constant output power across the operating frequency range. The reason for the frequency peak is due to inductive peaking in the CPW.

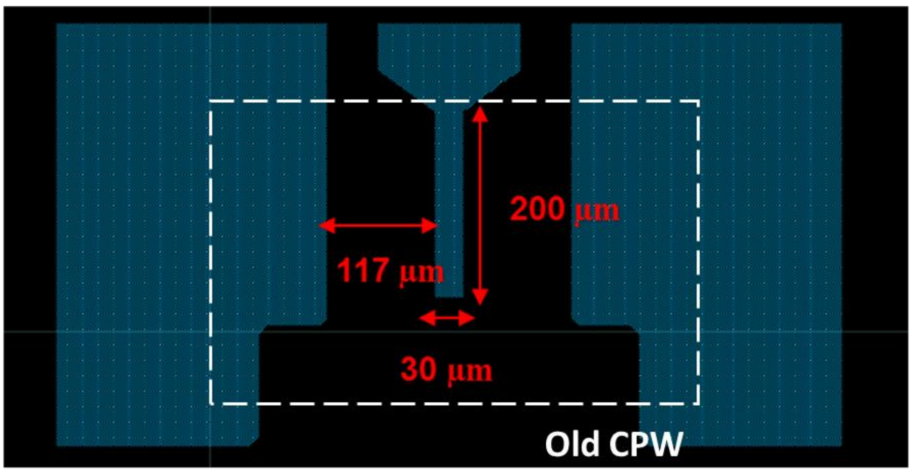

(a)

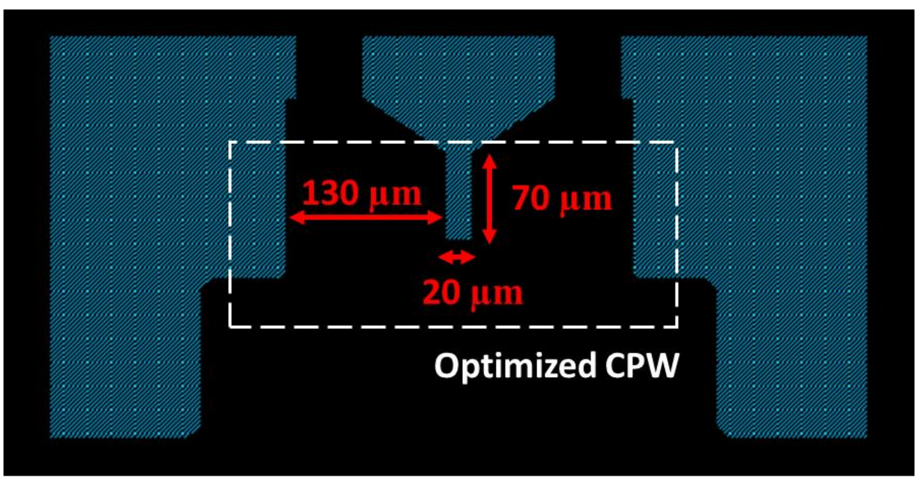

(b)

Figure 4-11. Old and optimized high impedance CPW layout for a 5 μm-diameter photodiodes.

With the photodiode equivalent circuit and extracted parameters from the S11 measurement. ADS circuit and EM simulators were used to optimize the CPW design. It follows that by tuning the characteristic impedance of the CPW, the frequency response can be flattened and larger device bandwidths can be achieved and higher output power can be delivered at high frequency. Figure 4-11 b shows the new CPW that I have designed for a 5 µm-diameter device. In order to reduce the inductance, a shorter transmission line was incorporated and optimized to achieve flat response with high bandwidth.

(a) (b) (c)

Figure 4-12. (a) Model 110 H probe; (b) Model 170 Probe; (c) VDI Erickson PM5 power meter.

The 5 µm-diameter and 6 µm-diameter devices were flip-chip bonded on the new CPW and device frequency responses were measured. To measure the RF output power, the Rohde Schwarz power meter together with GGB Model 110 H coaxial microwave probe were used to measure frequency up to 110 GHz. Above 110 GHz RF freqeuncy, a calibrated VDI Erickson PM5 and a GGB Model 170 waveguide microwave probe with an integrated bias tee were used. The PM5 power meter comes with a sensor head that has a WR10 waveguide input, while the Model 170 probe has a WR6 waveguide input. Therefore, there is a waveguide transition from WR6 to WR10. Figure 4-12 shows the probes images and VDI power meter. The cutoff frequency of the lowest order mode and the upper mode for WR6 is 90.791 GHz and 181.583 GHz. The starting frequency with the PM5 was chosen to be 100 GHz in order to provide a good overlap between the two setups in order to verify the accuracy of the measurements. The connetions for power measurement above 110 GHz are shown in Figure 4-13.

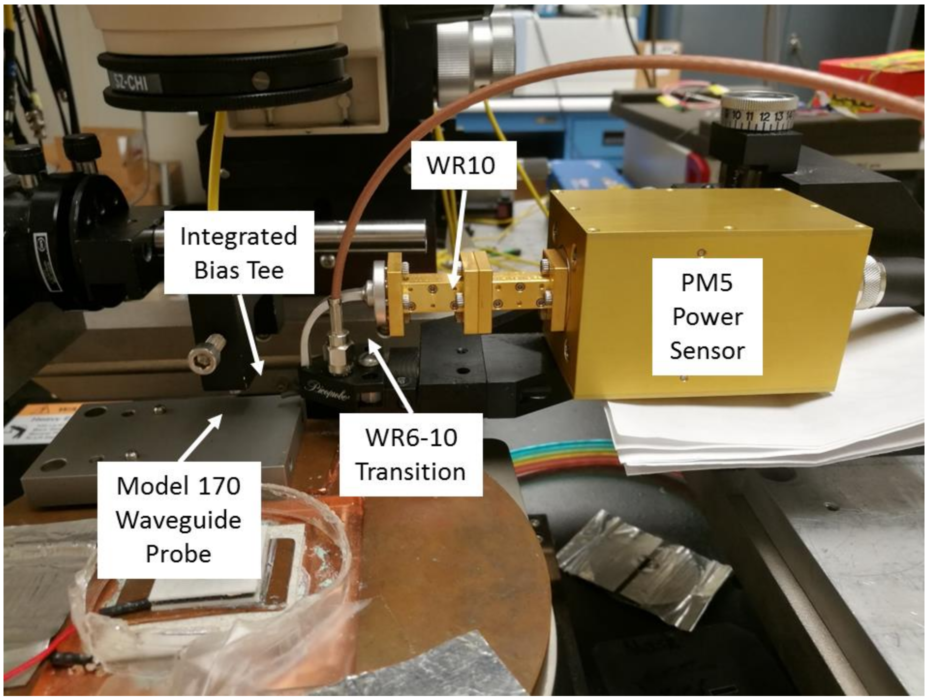

Figure 4-13. Power meter measurement setup for frequency above 110 GHz.

Normalized bandwidth plots of 5 µm-diameter and 6 µm-diameter photodiodes are shown in Figure 4-14. The black and red dots represents the power measurement with Rohde Schwarz and PM5 power meters, respectively. The power in the overlap frequency range (~100 GHz to ~110 GHz) is fairly consistent. From the plots, we can see that the bandwidth become flat across a large frequency range and no obvious peaking is observed in the new design. As expected, the bandwidths are improved to 125 GHz and 110 GHz for the 5 and 6 µm-diameter photodiodes, respectively, with the optimized CPW design.

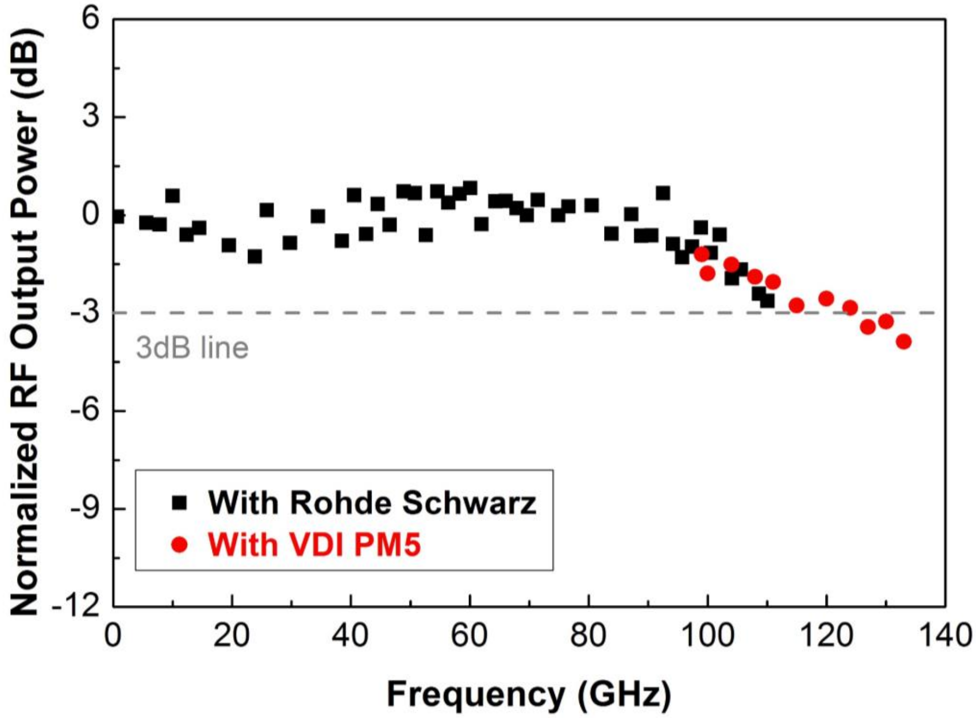

(a)

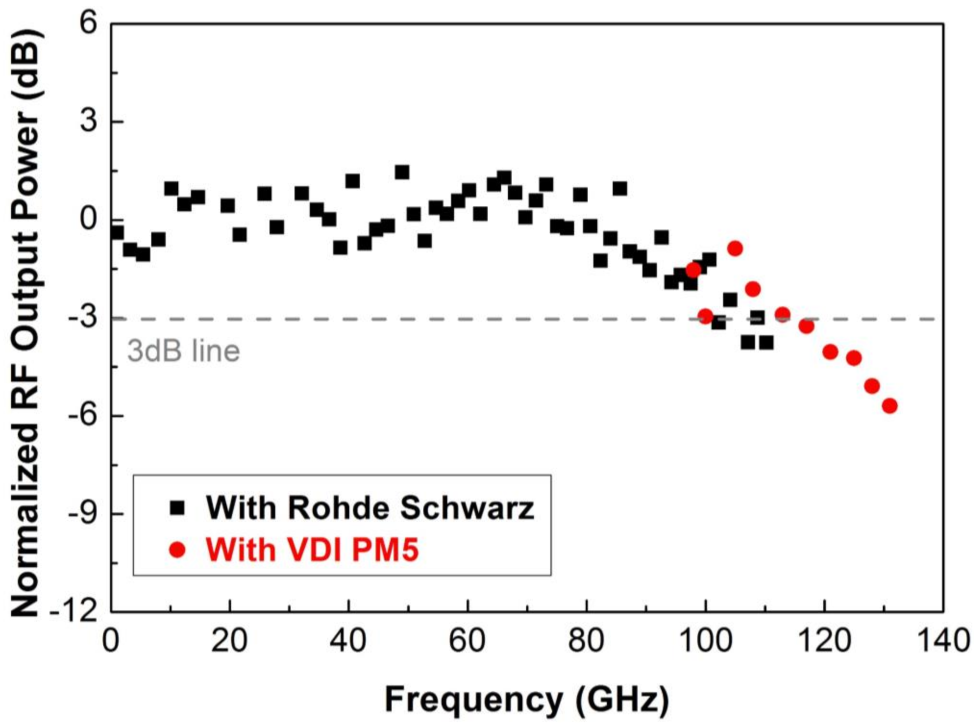

(b)

Figure 4-14. Bandwith of photodiodes. (a) 5 µm-diameter; (b) 6 µm-diameter.

With the above 110 GHz power measurement setup, RF saturation of 6 µm-diameter photodiode was measured at 130 GHz and 150 GHz with reversed bias of 3.5 V. Figure 4-15 shows the RF output trend with varying photocurrent. For a 6 µm-diameter photodiode, the RF output power was as high as 3.3 dBm and 0.83 dBm at 130 GHz and 150 GHz, respectively, with 50 ohms load. The device died because of thermal failure and the space charge effect was not observed. We suspect that the reason of early thermal failure is due to poor mesa side wall passivation as an indication of high device dark current which was in the µA range.

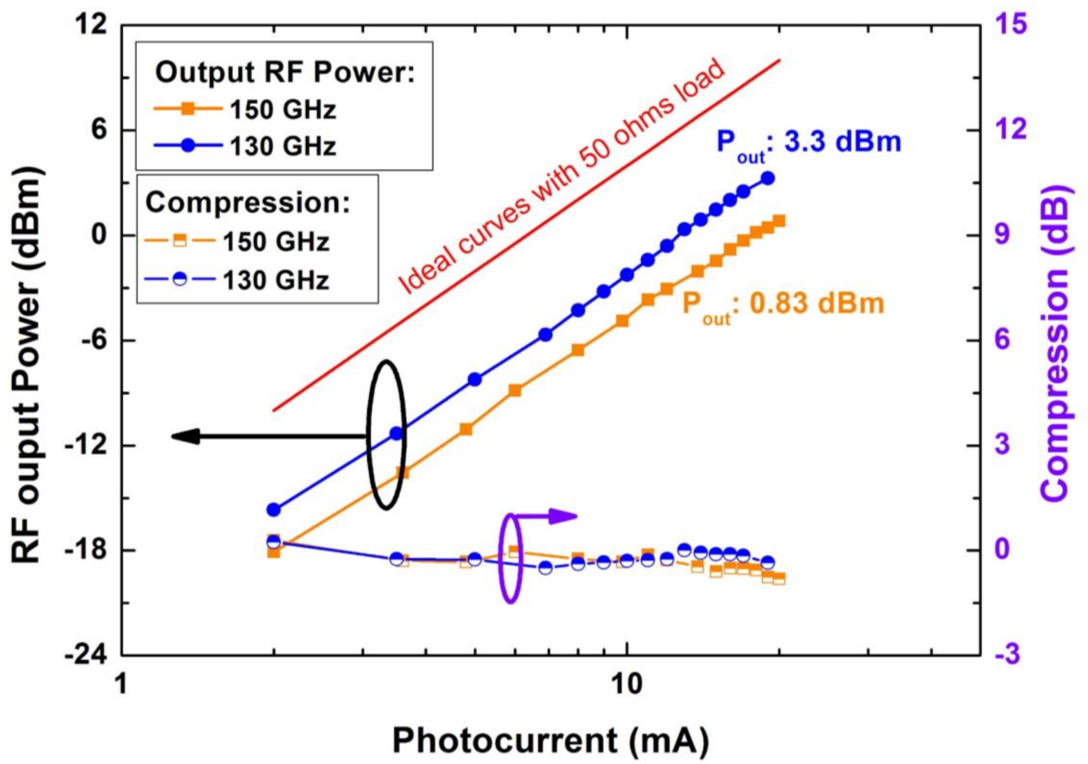

Figure 4-15. 6 µm-diameter device RF saturation.

4.6 Summary

High-speed, high-power flip-chip bonded MUTC photodiodes with 110 GHz bandwidth were realized by incorporating a high impedance transmission line for inductive peaking. The photodiodes have a typical responsivity of 0.17 A/W at 1.55 μm wavelength. In 6 μm-diameter PDs, the RF output power levels reach 7.8 dBm at 110 GHz and 9 dBm at 100 GHz. Photodiodes of 10 μm-diameter achieved RF output power of 13 dBm and 9.6 dBm at 75 GHz and 100 GHz, respectively. The O/E power conversion efficiency was 3.2%. Analysis using a simple equivalent circuit model based on extracted parameters from S11 fitting data suggests that the bandwidths of the PDs are limited by the *RC* component and the parasitic capacitance is the primary bandwidth limitation for 5- and 6 μm-diameter devices.

Based on the extracted parameters and a circuit model, photodiodes with an optimized CPW were fabricated and characterized. Bandwdith of 125 GHz with flat frequency response was achieved with 5 µm-diameter which is 12 % improvement compared with that from the old CPW design. A 6 µm-diameter photodiode can deliver as much as 3.3 dBm and 0.83 dBm RF output power at 130 GHz and 150 GHz, respectively.

Chapter 5. 100 GHz High Power Waveguide Integrated MUTC Photodiode

5.1 Introduction

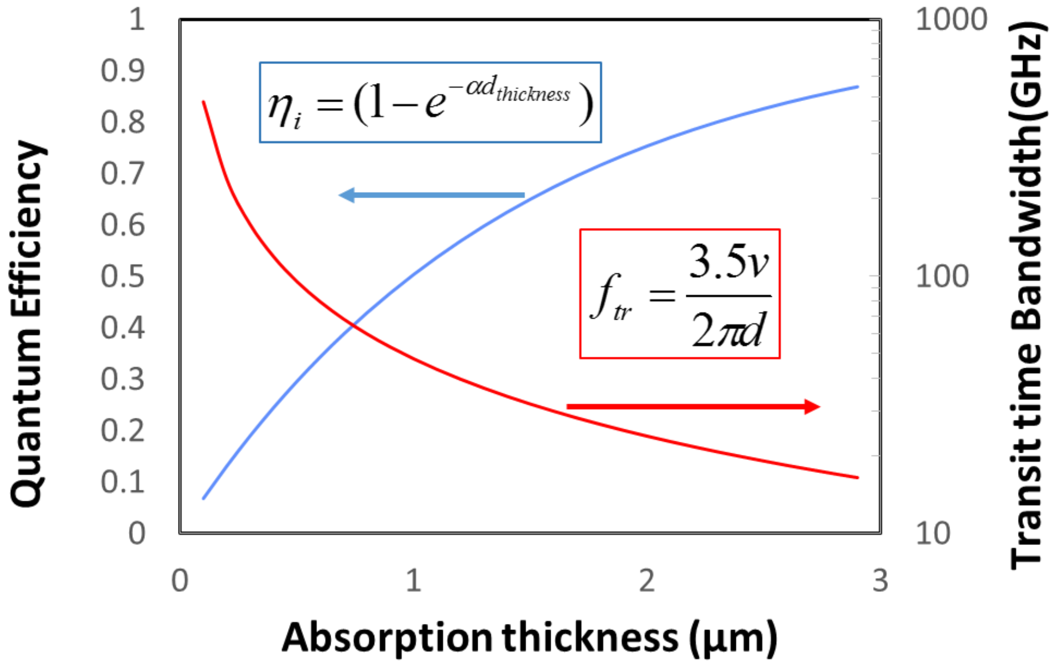

Figure 5-1. Normal incidence photodiode efficiency and bandwidth trade off (PIN photodiode).

A conventional lumped-element photodiode acts as a low pass filter; RF power decreases as frequency increases. As mentioned before, the speed of the device is limited by the carrier transit time and the resistance-capacitance (RC) time constant. Therefore, downscaling the dimensions of the photodiode including the depletion width and the device area in order to minimize carrier transit time and capacitance, respectively, increases the device frequency response. For normal-incidence photodiodes, this approach can achieve high bandwidth, however, at the price of low responsivity [5-1]. The bandwidth-efficiency trade-off of normal-incidence photodiodes prevents achieving high speed and high efficiency simultaneously as seen in Figure 5-1. To overcome this limitation, the first edge-coupled waveguide photodiode with 28 GHz bandwidth was demonstrated by J. E. Bowers in 1986 [5-2]. Figure 5-2 illustrates the two types of photodetector. In contast to normal-incidence photodiodes with light absorption and carrier collection in parallel , the carrier collection direction of waveguide photodiodes is perpendicular to the light absorption. In this way, the absorber can be thinner to reduce carrier transit time with longer absorption length to increase efficiency. By decoupling efficiency and speed, the waveguide photodiode can provide high quantum efficiency with short carrier transit times. In addition, the waveguide-photodiode can be heterogeneously integrated on InP or Si for photonic integrated applications [5-3].

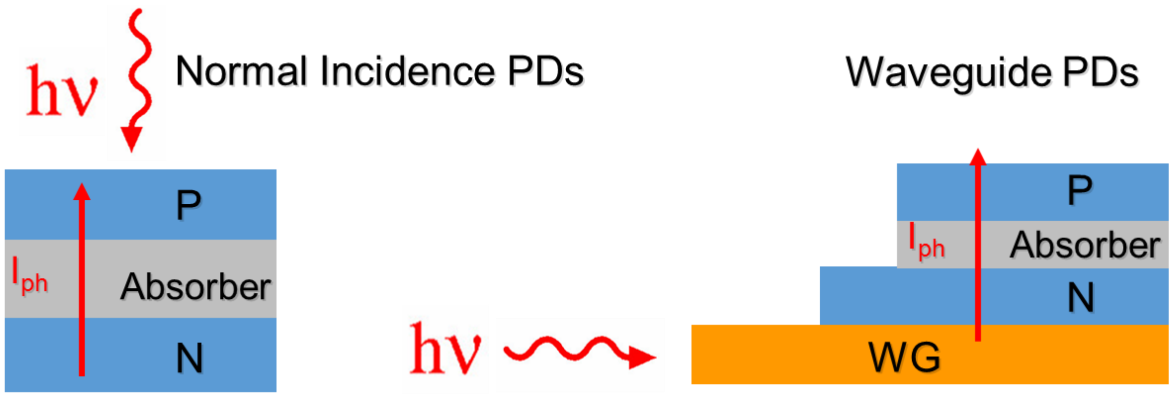

(a) (b)

Figure 5-2. (a) Normal incidence photodiode; (b) Waveguide integrated photodiode.

In this chapter, the epitaxial design of the waveguide integrated MUTC photodiode that has achieved greater than 100 GHz bandwidth is discussed. This is followed by a description of device design, fabrication procedure, and experimental results. Bandwidth limiting factors are investigated and an improved design that achieved 30 % higher bandwidth with the same external responsivity is described.

5.2 Device design and fabrication

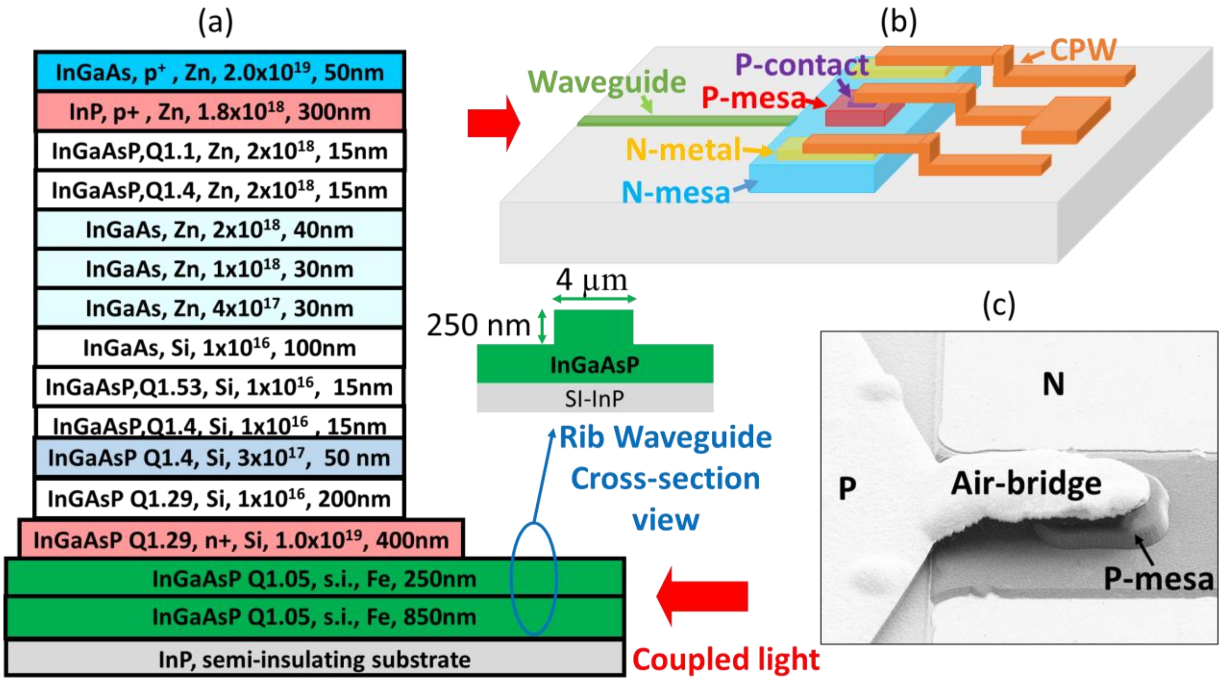

Figure 5-3. (a) Epitaxial layers of the InGaAs/InP photodiode. Doping concentration are given cm^{-3}. (b) Illustration of a waveguide photodiode structure for the 1st group of devices. (c) SEM image of the fabricated PDs (1st group).

Evanescently-coupled waveguide MUTC photodiodes were fabricated on a 3 inch-diameter InGaAs/InP wafer. Figure 5-3 (a) shows a schematic cross section of the epitaxial layer structure. The epitaxial layer design consists of three primary parts: a narrow-bandgap InGaAs absorber layer, a wide-bandgap InGaAsP drift layer, and a wide-bandgap InGaAsP waveguide layer. The use of InGaAsP in the drift layer instead of InP can result in better evanescent coupling at the expense of lower electron saturation velocity.

64

The epitaxial layers were deposited and in situ-doped with zinc (p-type) and silicon (n-type) dopants by metal organic chemical vapor deposition on semi-insulating InP substrate. A 1.1 µm–thick iron-doped InGaAsP quaternary layer was first deposited as the waveguide layer. Then, a 400 nm heavily doped n-type InGaAsP contact layer was deposited followed by a 200 nm lightly n-doped (1×10^{16} cm^{-3}) charge compensated drift layer. The reduced thickness of the contact layer compared with that of a surface normal device enabled high evanescent coupling efficiency [2-10]. A 50 nm-thick n-doped (3×10^{17} cm^{-3}) InGaAsP charge layer in combination with two 15 nm-thick lightly n-doped InGaAsP quaternary layers is used to maintain high electric field in the depleted absorber and to suppress charge accumulation at the heterojunction interfaces. A 100 nm unintentionally doped depleted absorber was added to improve quantum efficiency and bandwidth. Owing to concern about zinc diffusion during the growth, the p-type absorber was deposited on top, even though this resulted in lower responsivity compared to an "n-up" structure. Step grading of the 100 nm p-type undepleted absorber creates a quasi-electric field that aids electron transport. Two 15 nm-thick lightly p-doped InGaAsP quaternary layers were deposited to assist hole collection and block electrons. The p-type contact was formed using 300 nm heavily p-doped InP and 50 nm InGaAs.

Two groups of MUTC waveguide photodiodes were designed and investigated. The 1st group had areas in the range of 70 μm^2 to 370 μm^2. Figure 5-3 (b) shows a schematic of the input waveguide, the photodiode, and the electrode configuration of the 1st group. A double mesa process was used to fabricate these devices. The first etch, which defined the p-mesa, stopped at the n-contact layer. The n-mesa was formed later by dry etching to the iron-doped InGaAsP quaternary layer. The 4 µm-wide rib waveguide was then formed by dry etching another 250 nm. The n contact layer extended 8 µm toward the input waveguide in order to facilitate coupling from the input waveguide into the absorber and maximize the confinement factor. This extended n contact provides a gradual increase in the optical refractive index from the waveguide to the absorber, which enhances the quantum efficiency. AuGe/Ni/Au and Ti/Pt/Au were used for n-metal and p-metal contacts, respectively. The photodiodes were connected to gold-plated coplanar waveguide (CPW) RF pads through an air-bridge, as clearly seen in the SEM image in Figure 5-3 (c). A high impedance transmission line was incorporated into the CPW to provide inductive peaking in order to increase the device bandwidth. The completed wafer was cleaved to expose the waveguide facet for efficient light coupling.

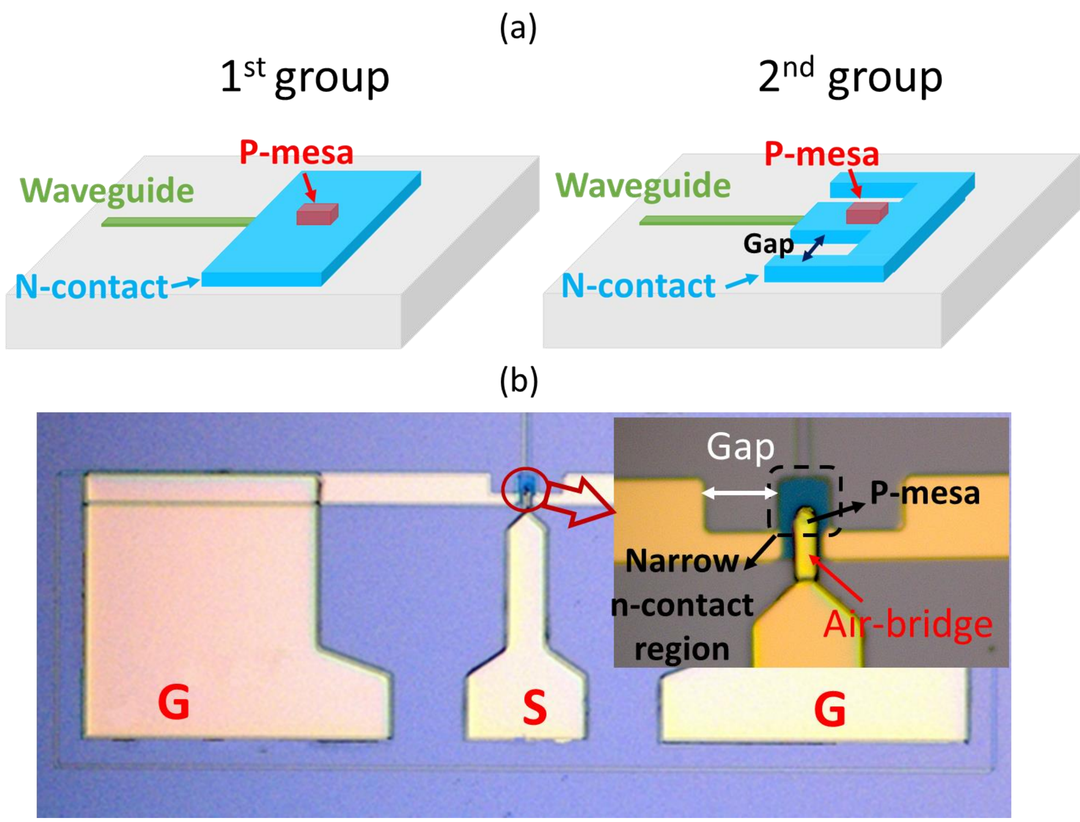

Figure 5-4. (a) 2nd group of photodiodes (S: signal G: ground), inset: gaps on each side of P-mesa; (b) Schematic comparison of 1st group and 2nd group.

Based on frequency analysis from the 1st group, the 2nd group was designed with smaller areas of 24 μm^2, 35 μm^2 and 50 μm^2 to reduce the RC time constant in order to achieve higher bandwidths. The 2nd group device structure was also modified to improve responsivity. The two structures are shown in Fig. 5-4 (a). For the 2nd group design, a small gap was created on each side of the p-mesa by removing the InGaAsP n-contact layer (Fig. 5-4 (b)). In this way, the optical field can be better confined along the narrow n-contact which results in higher responsivity.

5.3 Device Characterization

5.3.1 1st group of waveguide photodiodes

5.3.1.1 Electrical parameters

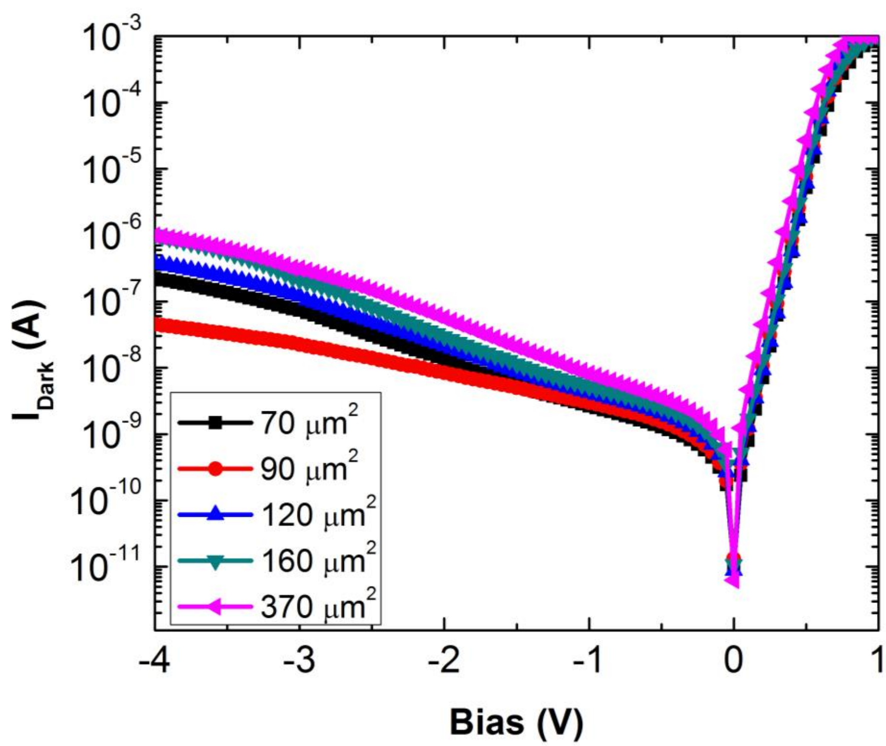

Figure 5-5. 1st group dark current.

Table 5-1. Measured Capacitance Summary.

C(fF)\A(μm²)	70	90	120	160	370
$C_{photodiode}$	44	51	60	71	138
C_t	8	9	10	10	10

As shown in Figure 5-5, the dark currents are < 1 μA at reverse bias up to 4V. The photodiode capacitance, $C_{photodiode}$, which is the sum of the junction capacitance, C_{pn}, the parasitic capacitance, C_{st}, and the CPW capacitance, C_t, was measured at 100 kHz using a multi-frequency LCR meter. In the mask design, CPW pads without a photodiode were also included in order to decouple C_t from $C_{photodiode}$. Table 5-1 summarizes $C_{photodiode}$ and C_t of the different device areas. The C_{st} was extrapolated by plotting the measured ($C_{photodiode}$-C_t) versus normalized area as the square dots shown in Figure 5-6. A C_{st} of 13 fF was determined from the intercept of the linear fit. A simple analytical equation was used to calculate the junction capacitance, C_{pn}. The measured C_{pn} ($C_{pn} = C_{photodiode}-C_t-C_{st}$) (round dots) agrees with the predicted values (triangle dots), where ε_0, ε_r, A, d are the permittivity of free space, the dielectric constant of InGaAsP, the photodiode active area, and the depletion width (380 nm), respectively. This enables the measured C_{pn} to be used in a circuit model to extract other parameters. Also note that for a 70 μm^2 photodiode the parasitic capacitance is greater than half C_{pn}, which suggests that parasitics limit the RC component of the bandwidth in the smallest photodiodes.

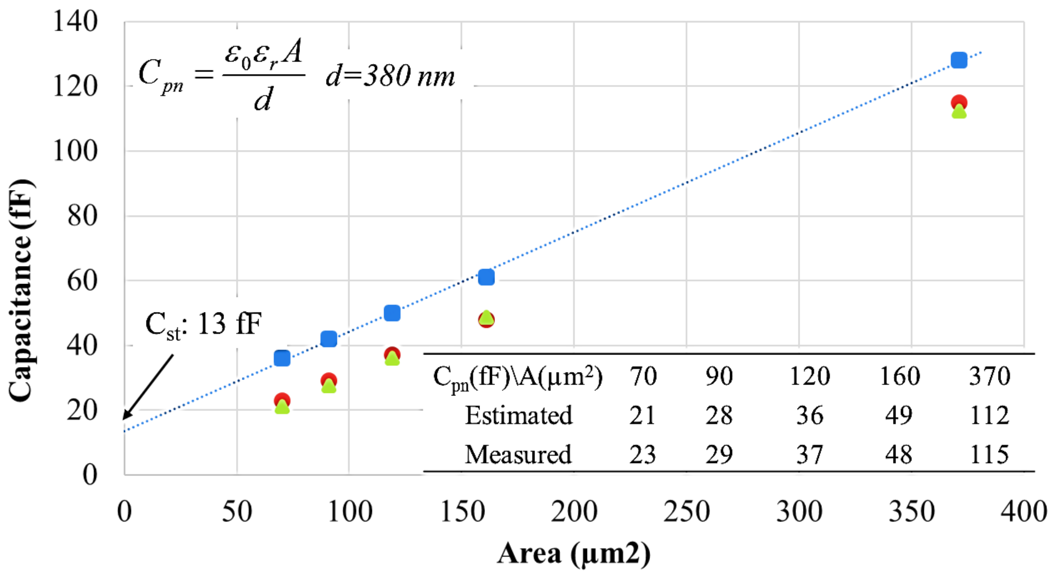

Figure 5-6. Capacitances versus normalized area. (Square dots: $C_{photodiode}$-C_t, round dots: $C_{photodiode}$-C_t-C_{st}, triangle dots: predicted C_{pn}).

5.3.1.2 Frequency Response

The setup in Figure 3-14 was implemented to measure the RF response. Additionally, a single-mode tapered fiber, with 2.4-µm spot diameter and 12-µm working distance, was used to couple light into the waveguide-photodiodes. The RF power was detected using a calibrated 50 Ω RF power meter with frequency range from DC to 110 GHz. A calibrated 110 GHz bias tee and an 8-inch W-band 1.00 mm semi-rigid coaxial cable were used in the setup. Their associated losses were calibrated out with a 110 GHz network analyser.

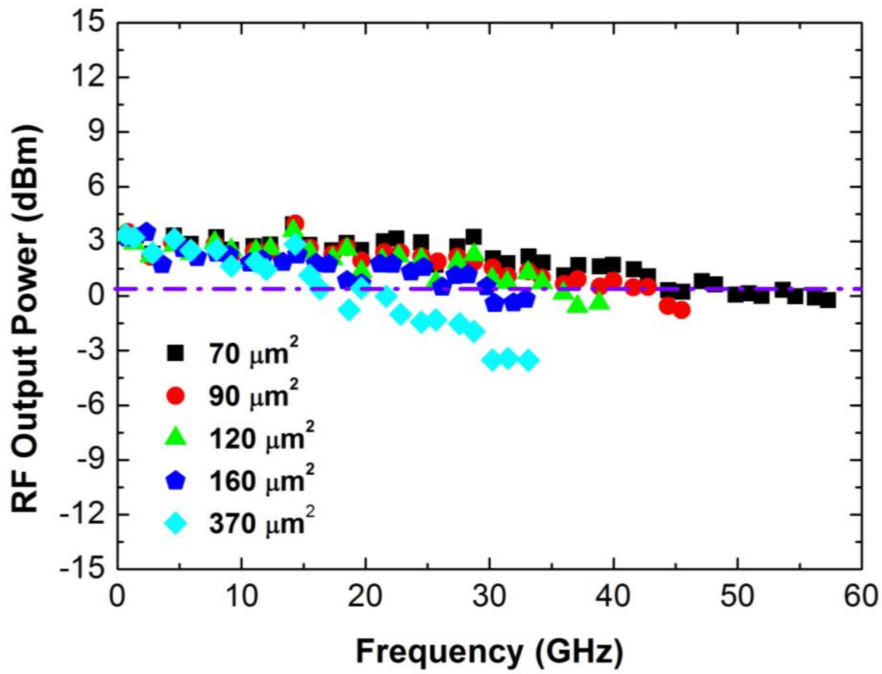

(a)

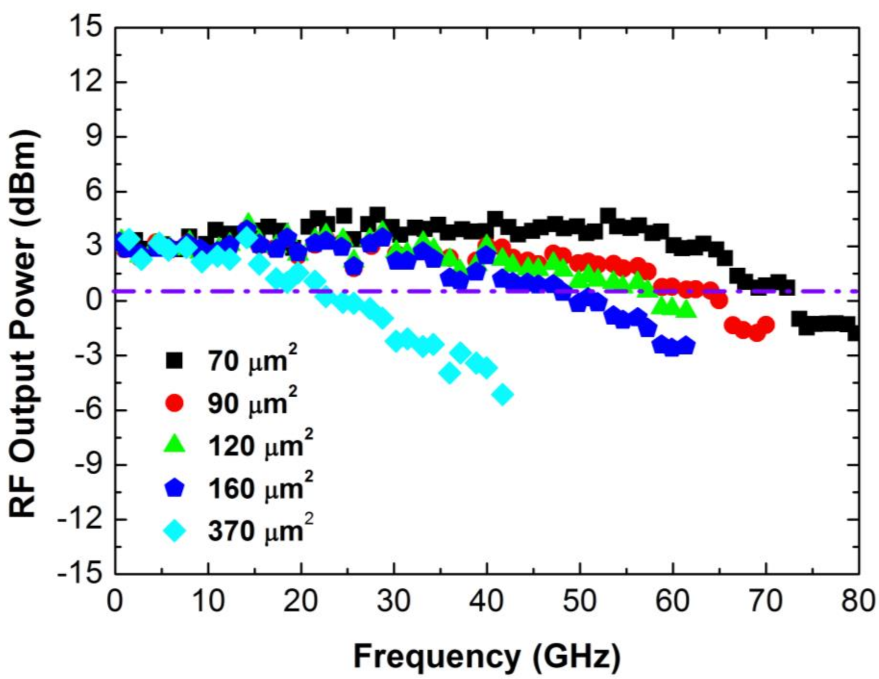

(b)

Figure 5-7. Measured frequency responses of devices with different area: (a) with 50 ohms CPW line; (b) with high impedance CPW lines.

A short section of transmission line with a large characteristic impedance can be approximately treated as a series inductor. Instead of using a discrete inductor, which cannot be easily incorporated in a photodiode design, a short-section high-impedance CPW was implemented in our design to improve the RC-limited bandwidth. To achieve the best peaking effect, an electromagnetic simulator in ADS was used to compute the S parameters of the high-impedance CPW, which was later incorporated into the photodiode model to simulate the frequency response in ADS. The characteristic impedance of our designed CPW is ~ 102 ohms.

Figures 5-7 (a) and 5 (b) summarize the frequency responses of the devices without and with inductive peaking, respectively. The devices were measured at 10 mA photocurrent with reverse bias of 4 V. 3dB bandwidth as high as 70 GHz was achieved with the 70 μm^2 device with a 50 Ω load. Table 5-2 shows the responsivity and bandwidth summary. An average of 50 % increase in bandwidth was obtained with inductive peaking. The device external responsivity including the coupling loss, reflection loss and the waveguide loss was in the range 0.15 ~ 0.3 A/W at 1550 nm wavelength. The facet of the 370 μm^2 device was damaged during cleaving which resulted in lower responsivity.

Table 5-2. Measured responsivity and bandwidth summary.

Area (μm^2)	**External Responsivity (A/W)**	**Bandwidth (GHz)**		**Increase (%)**
		No inductive Peaking	**Inductive Peaking**	
70	0.15	47	70	*49%*
90	0.21	43	64	*49%*
120	0.24	36	57	*58%*
160	0.30	31	48	*55%*
370	0.20	17	24	*41%*

71

5.3.1.3 Parameter extraction

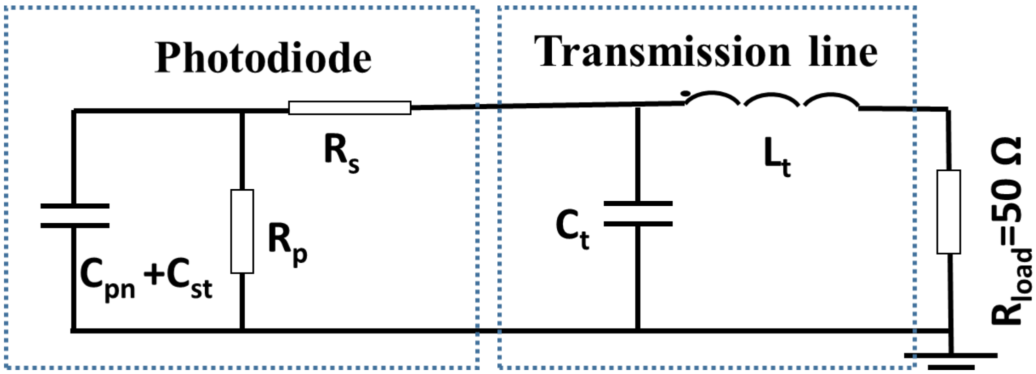

Figure 5-8. Waveguide-photodiode circuit model for S11 fitting.

On-wafer network analyzer measurements were performed to measure the S11 parameters up to 80 GHz. The diode circuit model (Figure 5-8) was determined from S-parameters using ADS software by parameter fitting. R_s and R_p represent the series resistance and the junction resistance, and C_t, L_t denote the capacitance and inductance of the high impedance CPW line, respectively.

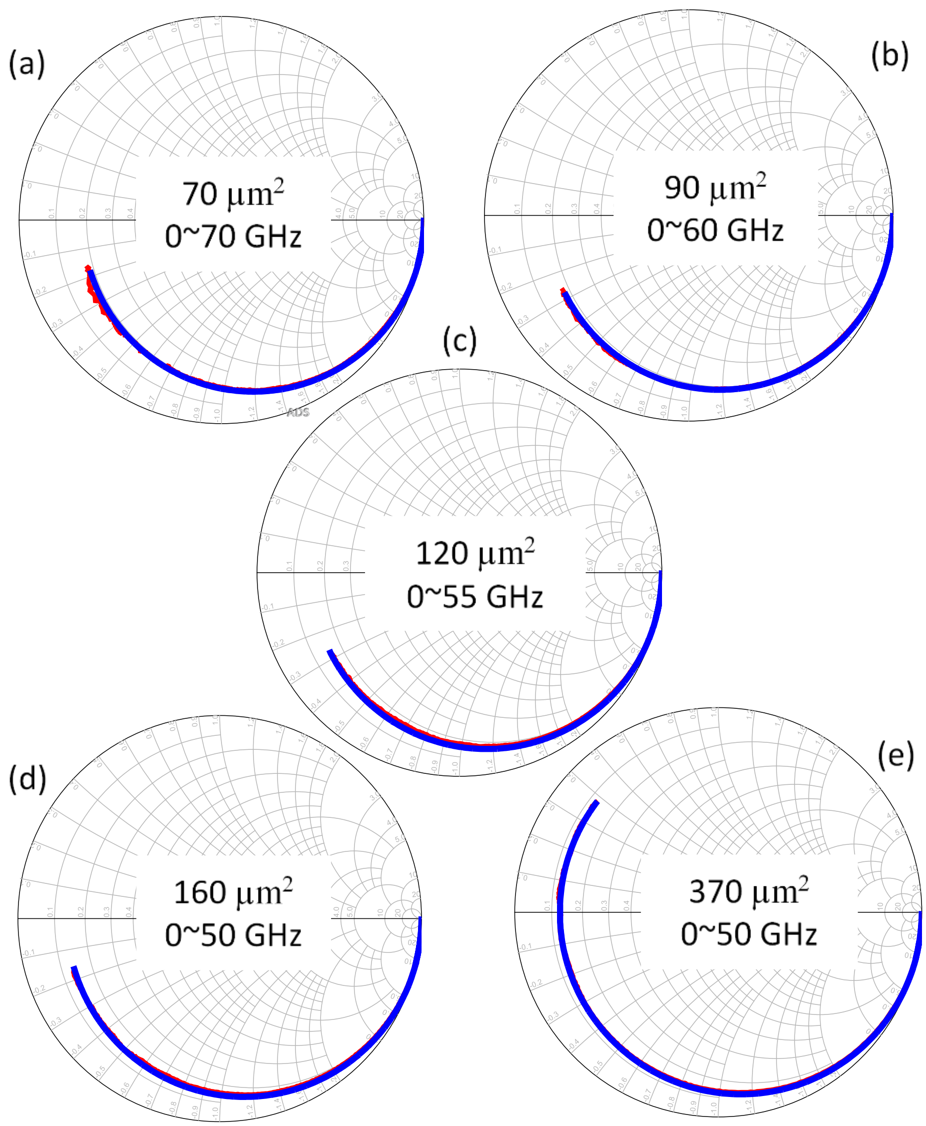

Figure 5-9. Measured (solid line) and fitted (dot line) S11 data for different devices (a ~ e) with corresponded frequency range (measured at -4 V bias).

In Figure 5-9, the measured S11 (solid line) and the fitted results (dot line) coincide well on the Smith Charts. The extracted parameters and the measured capacitances are summarized in Table 5-3. Note that on the Smith chart, the measured S11 values all start at the open circuit point, which indicates a large junction resistance, R_p. The extracted R_p is typically on the order of Gig-Ω and therefore, we did not include it in the table. From Table 5-3, R_s does not scale with device area, which indicates small contact resistance and that the bulk resistance dominates the total series resistance. The extracted inductances of the CPW line, L_t, increase as the device area increases, which matches our initial high impedance CPW design, since for inductive peaking, a larger inductor is preferred for larger devices with lower resonance frequencies.

Table 5-3. Extracted and measured parameters.

Extracted from S11 fitting (4V)				CV measurement	
Area (μm^2)	C_{tot} (fF)	R_s (ohms)	L_t (CPW) (pH)	C_{tot} (fF)	C_t (CPW) (fF)
70	39	14	89	36	8
90	44	13	97	42	9
120	50	11	100	50	10
160	62	9	115	61	10
370	130	7	132	128	10

Using the extracted parameters in the RC-limited model and transient-time-limited model in Eq. (4.1), the bandwidth was estimated and compared with the measured data. The results are plotted in Figure 5-10. There is good agreement between the simulated and measured results. For the smallest device in the 1st group, a 79 GHz RC-limited bandwidth was simulated, which indicates that the bandwidth (70 GHz) is limited by the RC time constant. For this epitaxial design, the transit-time-limited bandwidth is estimated to be approximately 117 GHz, assuming an electron saturation velocity of 8×10^6 cm/s in InGaAsP. Therefore, as the mesa area further scales down to 25 μm^2, the device bandwidth is expected to be greater than 100 GHz which will be confirmed in the 2nd group devices.

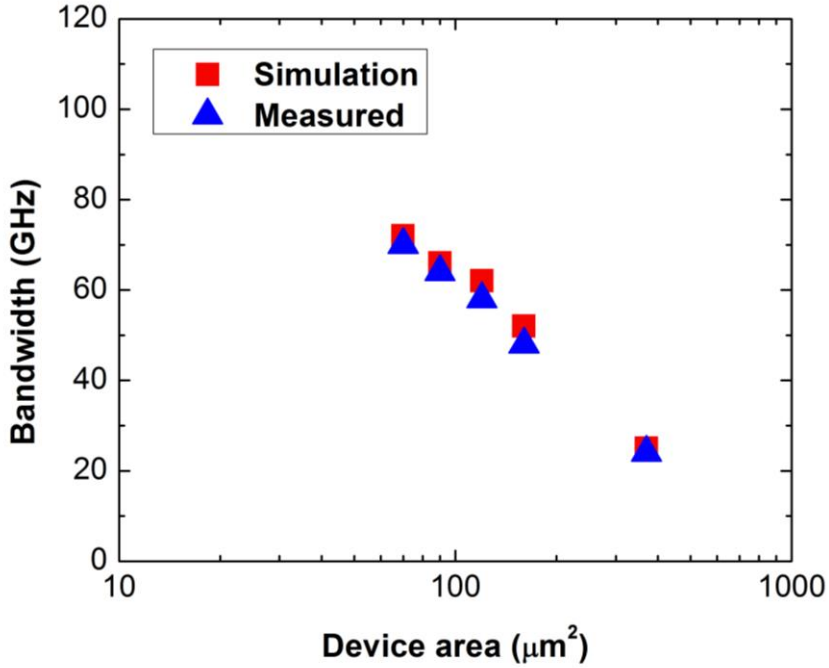

Figure 5-10. Comparison of simulated bandwidth with measured bandwidth.

5.3.1.4 RF power saturation

With a similar set-up as the bandwidth measurement described above, the RF saturation was characterized by measuring the RF output power as a function of the average photocurrent at a fixed frequency. Figures 5-11 a and b show the RF output power of 90 μm^2 and 70 μm^2 devices at 60 GHz and 70 GHz with different reverse bias, respectively. The 70 μm^2 device delivered 6.1 dBm RF output power at 3 V and 3.8 dBm when biased at 2 V. The 90 μm^2 devices achieved 7.8 dBm RF power at 3 V, which decreased to 7.0 dBm at 4 V and 5.8 dBm at 2 V. The 70 μm^2 device saturated at ~22 mA and ~28 mA when biased at 2 V and 3 V. For the 90 μm^2 device, saturation occurred at ~25.5 mA for both 2 V and 3 V bias and at ~ 20 mA with 4 V bias. We observe that the RF power was larger with higher reverse bias at a fixed photocurrent before saturation. This indicates that device bandwidth was enhanced as the bias increased from 2 V to 4 V before saturation.

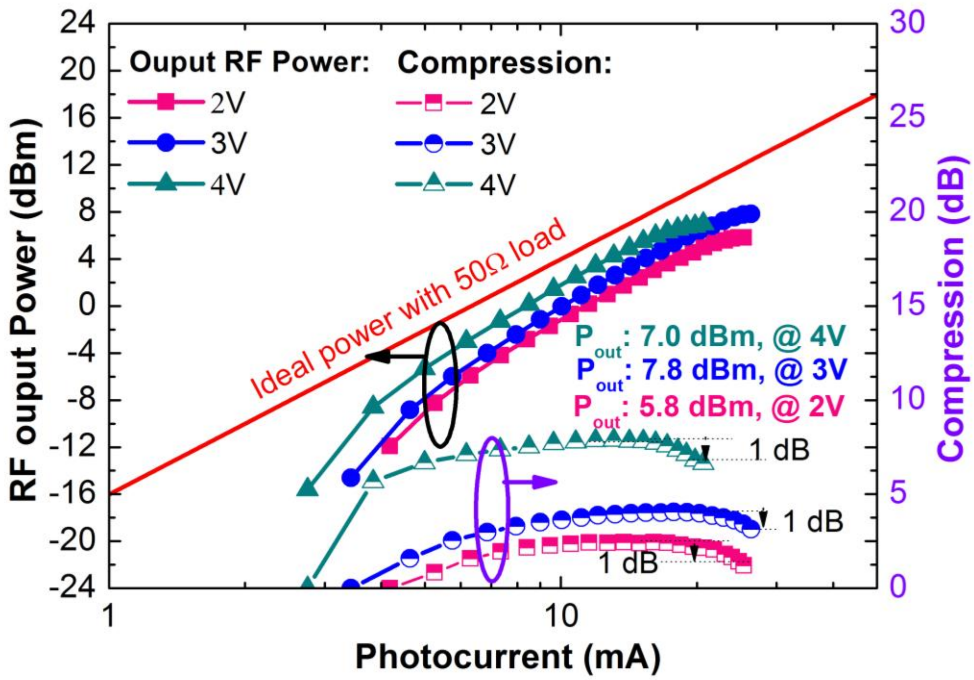

(a)

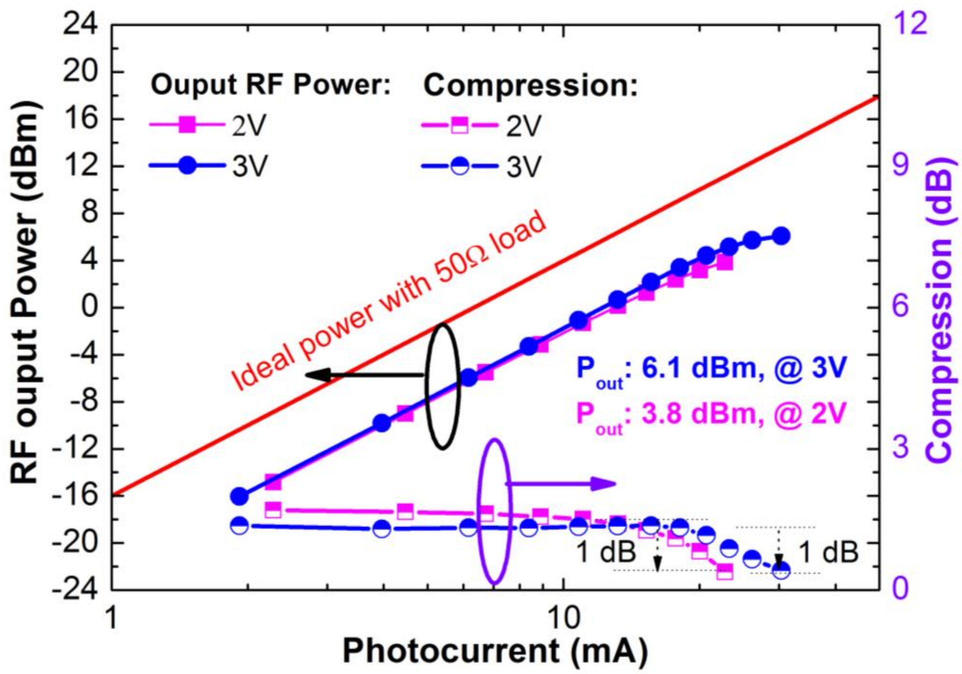

(b)

Figure 5-11. RF output power and RF power compression versus average photocurrent. (a): 90 μm^2 @ 60 GHz; (b): 70 μm^2 @ 70 GHz.

5.3.2 2nd group of waveguide photodiodes

5.3.2.1 Dark current and responsivity

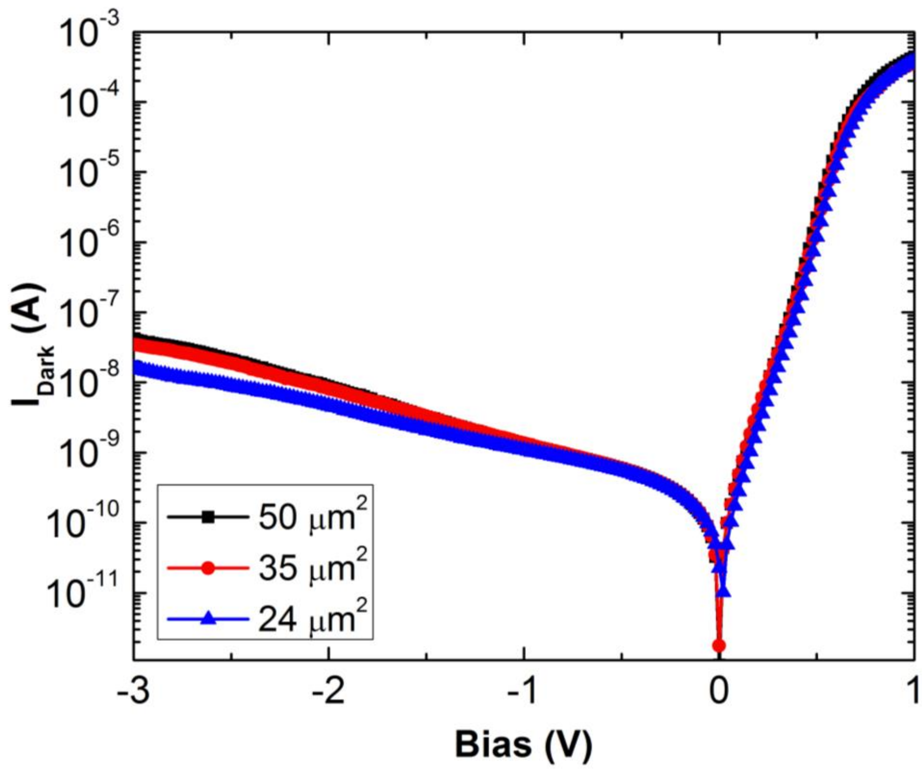

Figure 5-12. 2nd group dark current.

The 2nd group of photodiodes exhibited similar dark current (in Fig. 5-12) as the 1st group and the responsivities measured at 1.55 µm are summarized in the Table 5-4. The external responsivity was measured using a tapered fiber with 5.2 µm-diameter spot size and 24-µm working distance. The internal responsivity was estimated taking into account 1.5 dB reflection loss and 4 dB mode matching loss that was calculated using Beamprop software. The simulated internal responsivity is slightly higher than the responsivity estimated from measurements which can be attributed to losses in the long waveguides (0.7 mm ~ 1 mm) caused by side wall roughness.

Table 5-4. Responsivity summary.

Size (μm²)	R (A/W)		
	External R	Internal R	Simulated Internal R
24	0.1	0.35	0.38
35	0.12	0.42	0.48
50	0.15	0.52	0.64

5.3.2.2 Frequency response

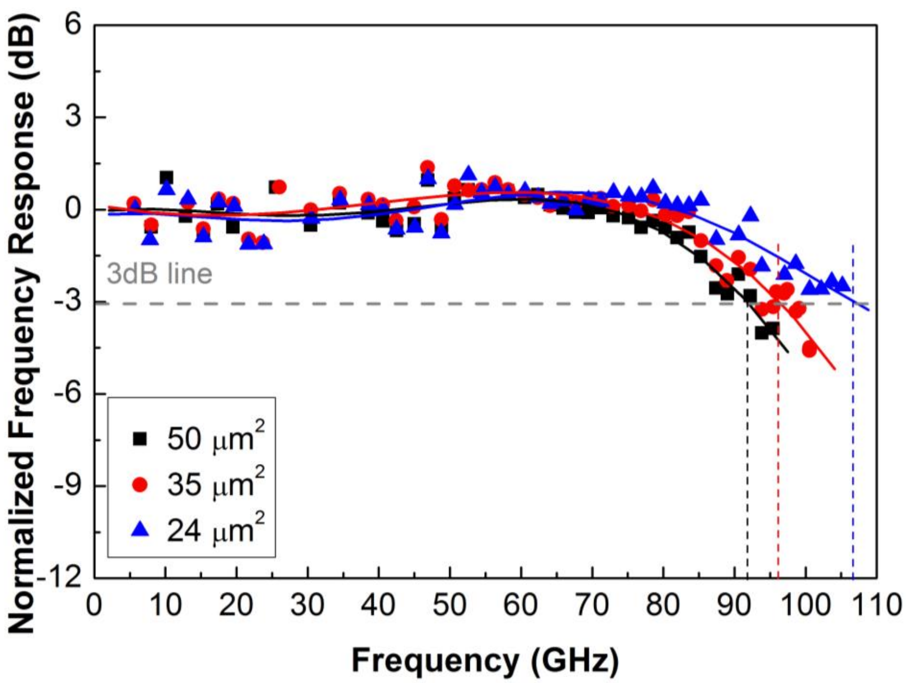

Figure 5-13. Frequency responses at -3 V bias. (Solid line: polynomial fitted)

The frequency responses of the 2nd group with various areas are shown in Fig. 5-13. The 24 μm² device was measured up to 110 GHz at reverse bias of 3 V. Owing to the inductive peaking, all three devices show flat response up to 80 GHz and they all exhibit 3 dB bandwidths over 90 GHz. The 24 μm² photodiode exhibits a bandwidth over 105 GHz, as predicted by the frequency analysis from the 1st group. The bandwidth approaches the estimated transit-time-limited bandwidth of 117 GHz. One important figure of merit is the bandwidth efficiency product (BEP). Photodiodes with 24 μm^2, 35 μm^2 and 50 μm^2 active areas have BEPs of 29 GHz, 32 GHz and 38 GHz, respectively. It is worth mentioning, that owing to the 2nd group design with narrow n-contact region at the waveguide feed section, the 50 μm^2 photodiode with bandwidth of 92 GHz has an external responsivity of 0.15 A/W, which is comparable to that of a 70 μm^2 photodiode having a bandwidth of 70 GHz in the 1st group, i.e., the new structure achieves 30% higher bandwidth at the same responsivity. To further improve device external responsivity, future PDs will incorporate an anti-reflection coating and a spot size converter [5-4].

5.3.2.3 RF power saturation

The highest RF output powers of a 50 μm^2 device in the 2nd group are shown in Fig. 5-14 (a) measured at 75 GHz, 80 GHz, 90 GHz, 100 GHz and 105 GHz as a function of average photocurrent. Note that bandwidth of 50 μm^2 is ~ 90 GHz. Therefore, the power curves measured at higher frequency, like 100 GHz, were constantly a few dB lower than that of lower frequency, like 75 GHz. Overall, it could achieve 5.1 dBm, 4.4 dBm, 3.5 dBm, 2.0 dBm and 1.3 dBm at 75 GHz, 80 GHz, 90 GHz, 100 GHz and 105-GHz, respectively. RF powers of smaller area devices are shown in Fig. 5-14 (b). The 35 μm^2 photodiode can deliver as high as 0.5 dBm and -0.4 dBm at 90 GHz and 100 GHz frequency, respectively, with saturation current of 10 mA. Note that the 24 μm^2 device died at 5.5 mA photocurrent with output power of -4.8 dBm at 105 GHz, while 1 dB compression was not observed. This is an indication that the cause of device failure was thermal. By incorporating a high-thermal-conductivity heat sink coupled with a flip-chip bonding technique, it is anticipated that higher RF power can be extracted from photodiodes with small dimensions.

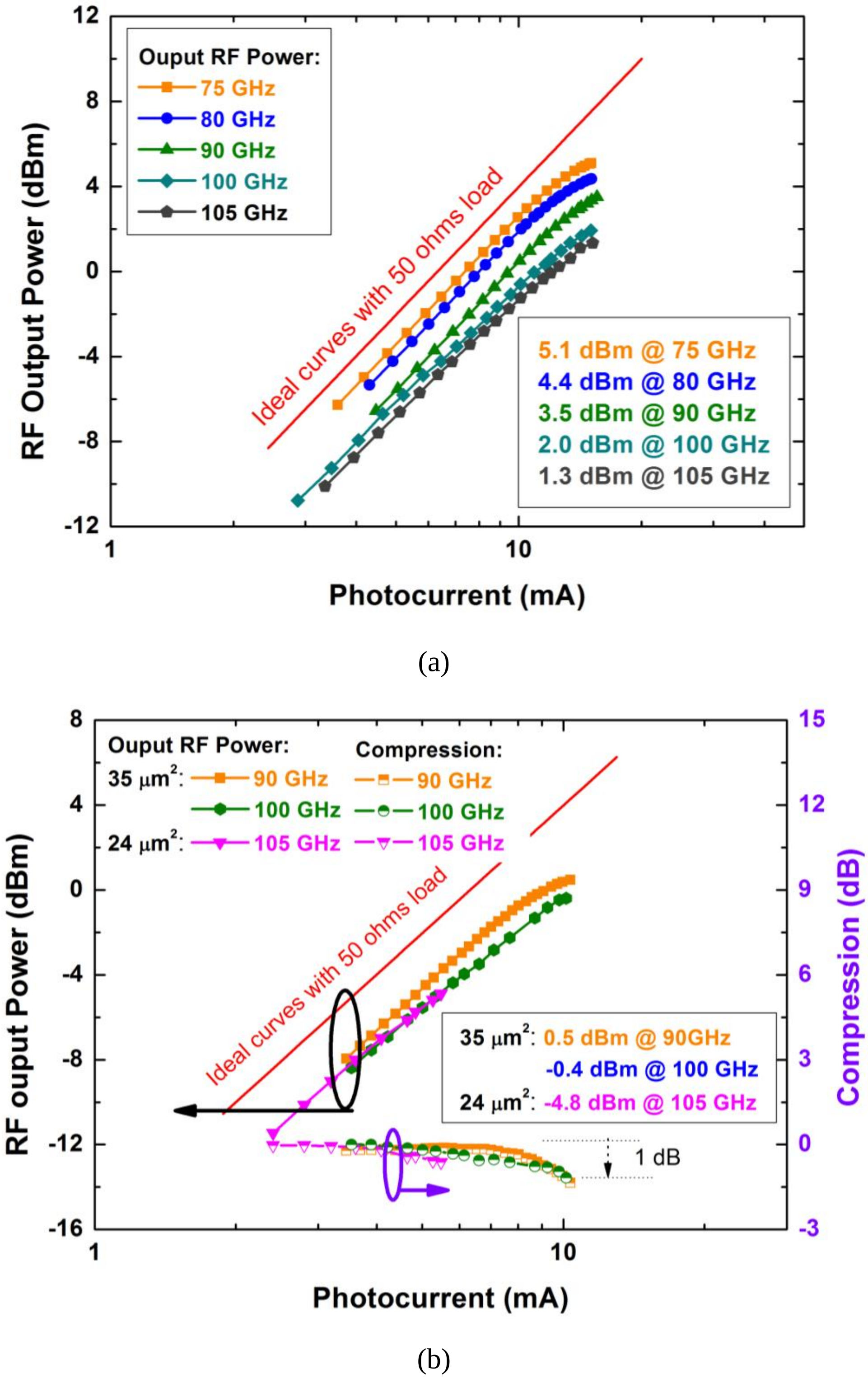

Figure 5-14. RF output power and RF power compression versus average photocurrent measured at -3 V: (a) 50 μm^2; (b) 35 μm^2 and 24 μm^2.

5.4 Summary

To improve efficiency while maintaining high bandwidth, and for better integration in photonic circuits, high-power evanescently-coupled waveguide integrated MUTC photodiodes were designed and characterized. Two groups of devices were designed and investigated. The photodiodes in the 1st group achieved bandwidth of 70 GHz with high RF output power of 7.8 dBm and 6.1 dBm at 60 GHz and 70 GHz, respectively. Using the results the 1st device group, the redesigned 2nd group showed > 105 GHz bandwidth. The 50 μm^2 devices in the 2nd group exhibited bandwidth efficiency product of 38 GHz with over 90 GHz bandwidth, which is more than twice the bandwidth efficiency product of the normal-incidence photodiodes discussed in Chapter 4. With the improved gap design in terms of better optical field confinement along the narrow n-contact, the photodiode achieved 30% higher bandwidth with the same external responsivity compared with the 1st group. The RF output power from these photodiodes were 2 dBm and 1.3 dBm at 100 GHz and 105 GHz, respectively.

Chapter 6. W-Band Emitter by Photomixing with High Power MUTC Photodiode

6.1 Introduction

There are many applications of high power high speed photodiodes in analog links. For instance, the high power W band photodiodes can be used for long-distance antenna remoting in combination with a wide-band high-power source signal. For military radar, an analog optic link that utilizes a high-power W band photodiode provide higher resolution in detecting and targeting objects (like drone), as well as enabling wider radar coverage area. Also, for satellite communications, high-power W band photodiodes can provide high-speed communications with high signal to noise ratio.

Recently, with the emergence of the Internet of Things (IoT) and the exponential increase of smart wireless devices, the demand for high-speed wireless data transmission necessitates that the wireless network be able to support extremely high data rates. Since the low-frequency band is too crowded for high-speed wireless link applications, it becomes inevitable to extend carrier frequencies to the millimeter-wave (MMW) band above 60 GHz (V-band) or even to 100 GHz (W-band) [6-1], [6-2]. Realization of such high-speed systems in electronics has intrinsic drawbacks such as high propagation loss in coaxial cables and narrow bandwidth of electronic circuits, which are incompatible with high-performance operation at both V and W frequency bands. Developing MMW wireless links using photonic techniques seems advantageous due to the low loss of optical fibers and inherent large bandwidth of photonic microwave components. Recently, significant interest has been paid to microwave photonic wireless emitters that tightly integrate a high-speed photodiode and an antenna.

The MUTC photodiode I developed can be quite suitable for W band photonic wireless emitters due to its bandwidth performacnce and high power capability. The other essential component of an emitter is the antenna that radiates EM waves. In order to compensate for the attenuation of MMW radiation in the atmosphere, antennas with high directional gain are desired in order to concentrate the beam in a certain direction. Planar structures including slot, log-periodic toothed, Vivaldi and bow-tie antennas as well as traveling-wave antenna structures are preferred for the purpose of system miniaturization, planar integration and wide bandwidth compared with the bulky and incompatiable commercial horn antennas or Si lenses that have been used for this purpose [6-3], [6-4].

In this chapter, W-band photonic emitters are achieved by integration of planar Vivaldi antennas with the flip-chip-bonded high-power high-speed MUTC photodiodes discussed in chapter 4. The high gain of the Vivaldi antenna and the usage of a superstrate eliminate the need for the horn antenna or Si lens. An impedance matching network was designed to achieve conjugate impedance matching between the MUTC PD and the antenna. Owing to these improvements, a record high effective isotropic radiated power (EIRP) of 5 dBm was achieved. This work is in collaboration with Dr. Steven Bowers group who provided the impedance matching network and Vivaldi design.

6.2 Vivaldi Antenna and matching network

The Vivaldi antenna was chosen for its wide RF bandwidth, highly directive end fire beam and planar profile, all of which are suitable for integration into large-scale phased arrays. The Vivaldi antenna is a tapered slot-line antenna, which has similar impedance characteristics to continuously tapered slot-line matching networks. It presents an approximately real impedance over a very broad range of frequencies. A simple method for distortion suppression is to place a superstrate on top of the antenna for distortion suppression by equalizing the electromagnetic wave propagation velocity in air and the substrate.

In order to maximize the radiation power from the antenna, a resonant impedance matching technique was employed where the DC bias lines for the PD were used in conjunction with a quarter-wavelength RF short circuit to synthesize an inductance, which resonates out the PD junction capacitance. This resonance was optimized between 100 and 110 GHz for maximum extraction of RF power generated by the PD.

AlN was used for the antenna substrate due to its high thermal conductivity, which significantly increases the dc power dissipation of the PD [2-12]. The antenna and impedance matching network pattern were fabricated on AlN substrate using electron-beam metal deposition, photolithography and dry etching processes. Similar to PDs flip-chip bonded on CPW submount, the PDs were flip-chip bonded onto the attenna and matching network using a Au-Au thermo-compression bonding process at 340 ºC. Fig. 6-1 (a), (b) show an optical image and 3D schematic of the integrated photonic emitter, respectively.

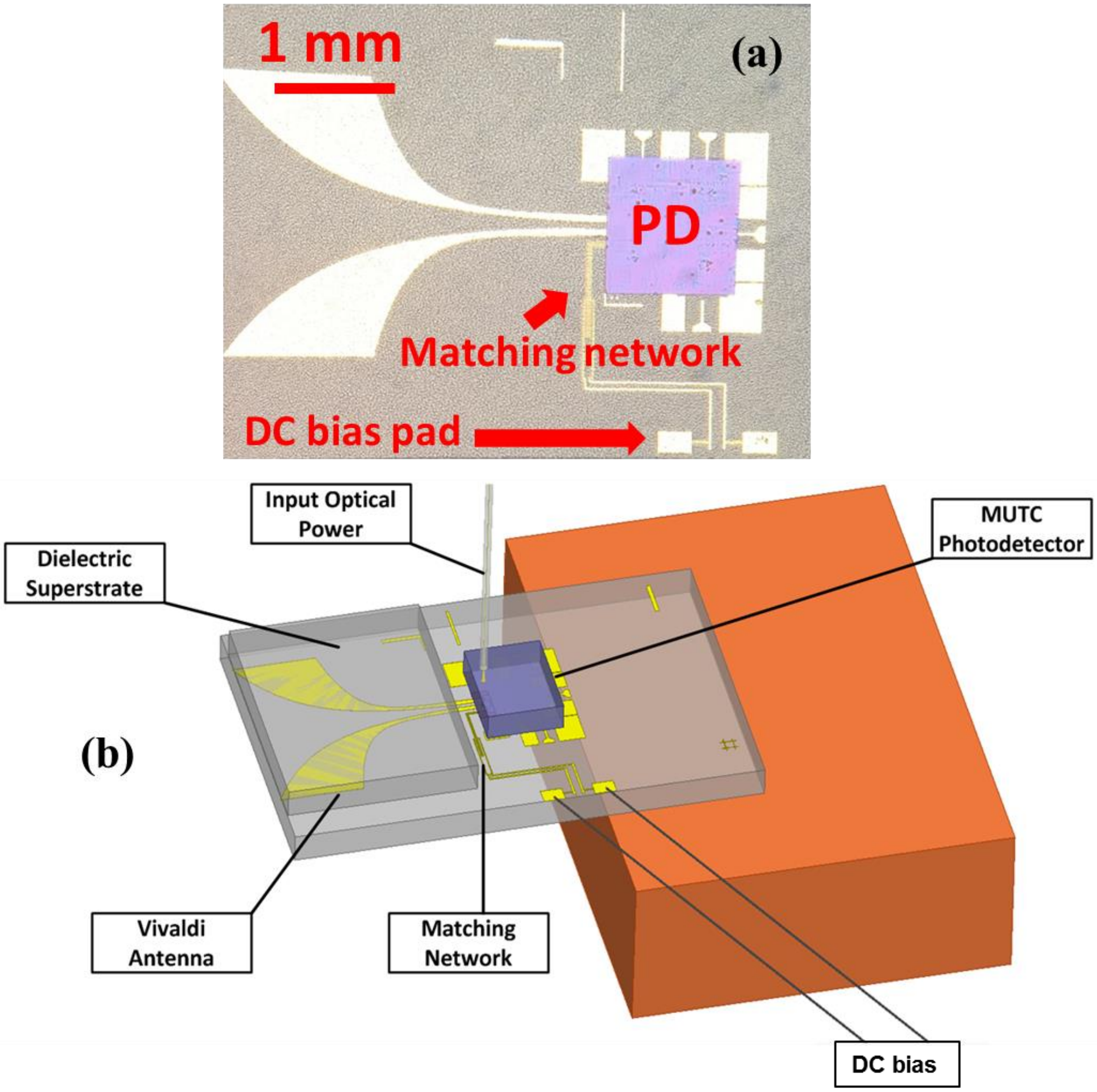

Figure 6-1. (a) Optical image of the photonic integrated emitter; (b) 3D schematic of the integrated photonic emitter.

6.3 Experimental Results

6.3.1 Experimental setup

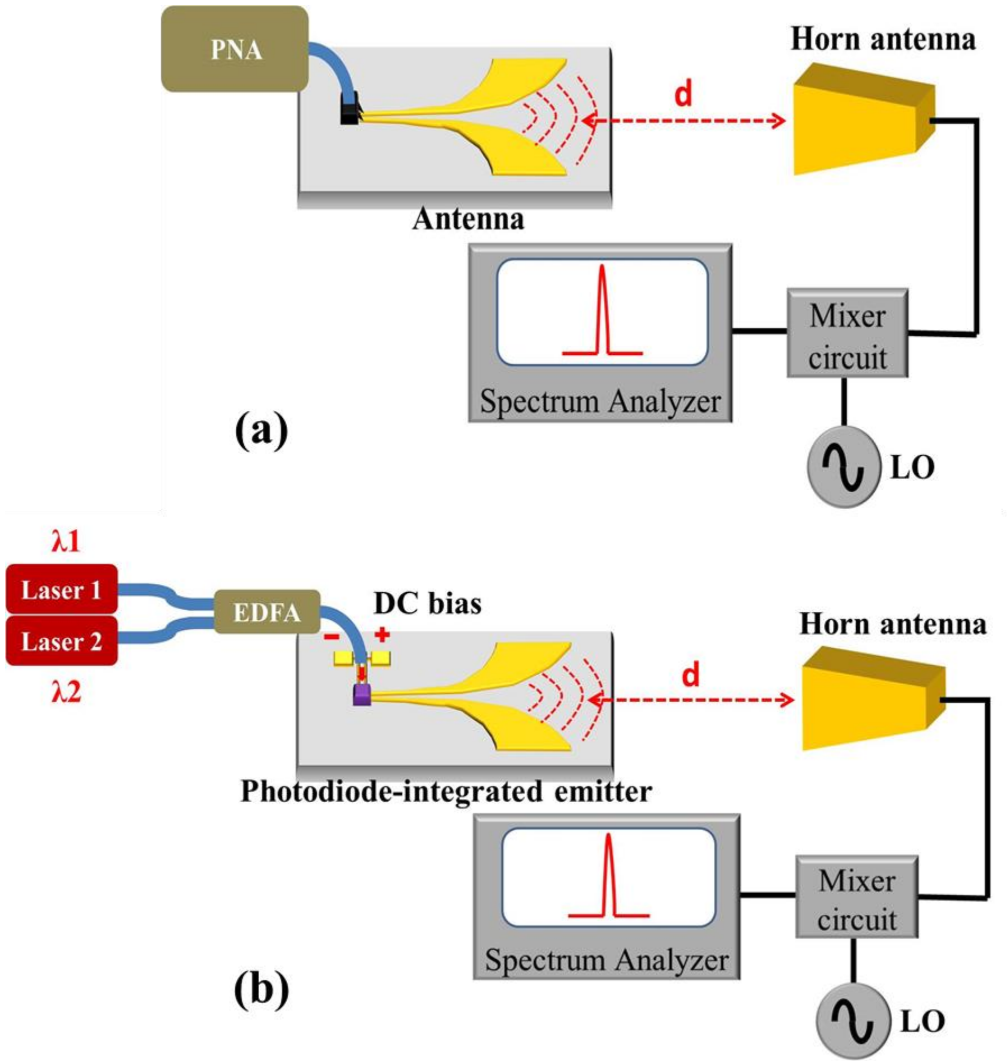

Figure 6-2. Experimental setup for (a) Antenna gain measurement; (b) integrated photonic emitter radiation measurement.

The experimental setups for measuring the antenna gain and the radiation characteristics of the integrated photonic emitter are shown in Fig. 6-2 (a) and (b), respectively. For the antenna gain measurement, a constant CW power was fed into the antenna from a PNA network analyzer equipped with 110 GHz frequency extender module. For the photonic emitter radiation measurement, an optical beat signal was generated similar to the signal from the bandwidth measurement discussed in Chapter 3.4.3. The wavelengths of the two laser diodes was monitored by a multiwavelength meter. An erbium doped fiber amplifier (EDFA) was used to amplify the optical signal. The output optical signal incident on the PD was adjusted by a variable optical attenuator following the EDFA. A commercial horn antenna (QuinStar, QGH-WPRR00) with 23 dB gain was used as the receiving antenna. A W-band mixer (Pacific Millimeter, WM harmonic mixer) was used to convert the W-band RF signal down to an IF frequency around 2 GHz. The IF signal was fed into a spectrum analyzer (Agilent, E4440A) from which the power was read.

6.3.2 Antenna with impedance network

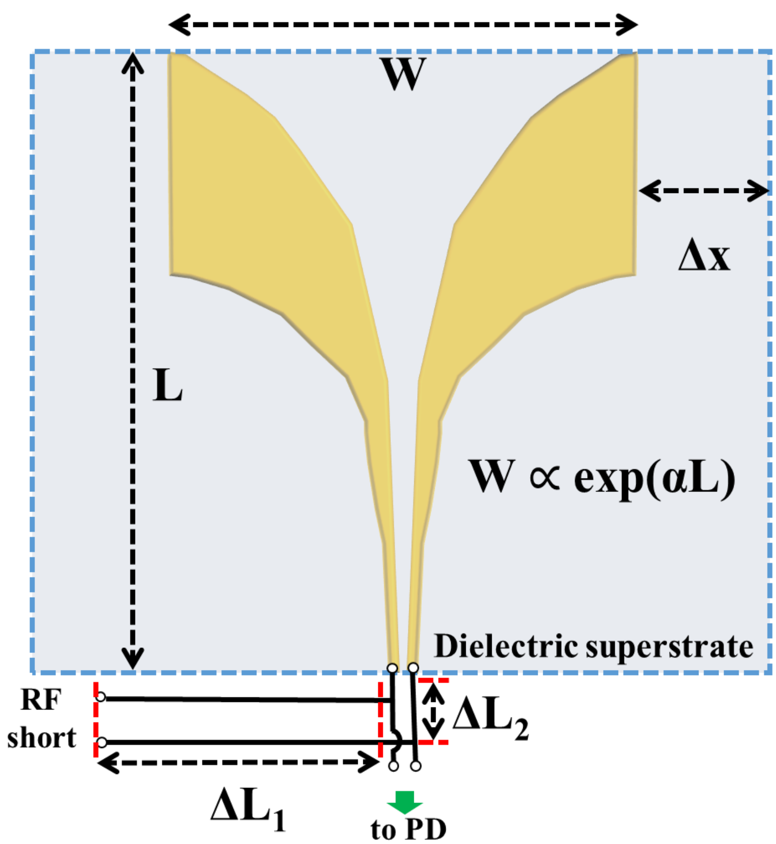

Figure 6-3. Schematic and dimension of the antenna plus matching network.

A schematic of the antenna connected to impedance matching network is shown in Fig. 6-3. The RF short is realized by a quarter-wavelength open stub. The transmission line of length $\Delta L_1 + \Delta L_2$ after the RF short is effectively an inductor to resonate with the PD junction capacitance. Since the 5 and 6 μm-diameter PDs have capacitive impedances in this frequency range, the antenna with matching network should have an inductive input impedance to achieve conjugate matching. The physical dimensions of the antenna and matching network are given in Table 6-1:

Table 6-1. Diminsions of the antenna and matching network.

W (mm)	L (mm)	Δx (mm)	α (mm^{-1})	ΔL_1 (μm)	ΔL_2 (μm)
2.4	2.7	0.2	1.4	509	185

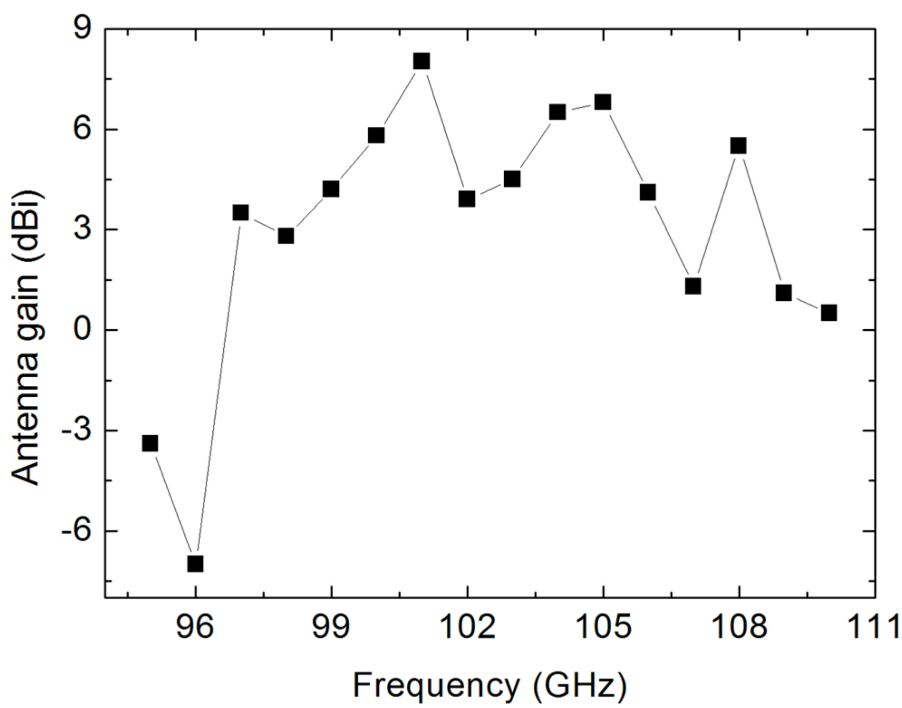

Figure 6-4. The measured directional gain of antenna between 95 and 110 GHz.

The directional gain of the antenna design was measured in the far field at a distance of 57 cm. The gain was calculated from the path loss, mixer loss and receiving horn antenna gain using the Friis equation [6-5]. Figure 6-4 shows a plot of the directional gain of this antenna over the frequency band from 95 to 110 GHz. The antenna gain reaches 3 dBi or more over a bandwidth of 10 GHz around 100GHz.

6.3.3 Effective isotropic radiated power (EIRP) of integrated photonic emitter

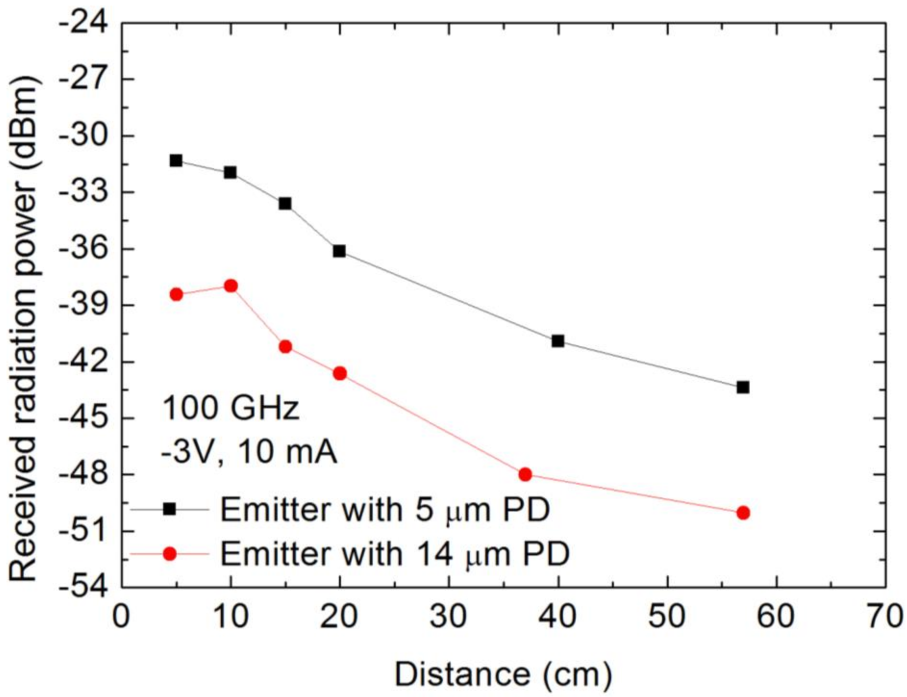

Figure 6-5. Received radiation power versus distance at 100 GHz for 5 and 14 µm-diameter PDs at 10 mA photocurrent and -3 V bias voltage.

The radiation power at 100 GHz from the integrated photonic emitters with 5 and 14 µm-diameter PDs biased at -3 V and 10 mA photocurrent was measured at different distances from the emitter. As shown in Fig. 6-5, the received radiation power decreases with increasing distance due to a larger path loss and enters the far field at 57 cm. The received power for the emitter with the 5 µm-diameter PD is 8 dB higher than the one with the 14 µm-diameter PD at the same photocurrent which can be explained by an improved impedance matching. The EIRP at different photocurrents was measured in the far field. The results are shown in Fig. 6-6. The EIRP increases with increasing photocurrent as expected. The EIRP from the emitters with the 5 and 6 µm-diameter PDs is 7.5 and 6 dB higher than the power from the emitter with the 14 µm-diameter PD, respectively. The higher power is attributed to the better impedance matching between the 5 and 6 µm-diameter PDs and the antenna. The emitter with 5 µm-diameter PD has an EIRP approximately 1.5 dB higher than the emitter with 6 µm-diameter PD does. Based on the fact that the impedance matching condition for the 5 and 6 µm-diameter PDs are similar, the possible reason for this difference is that the 5 µm-diameter PD has a slightly higher 3 dB bandwidth than the 6 µm-diameter PD. The EIRP does not increase linearly at high photocurrent, an indication of power compression due to the space charge effect in the PD at high photocurrent.

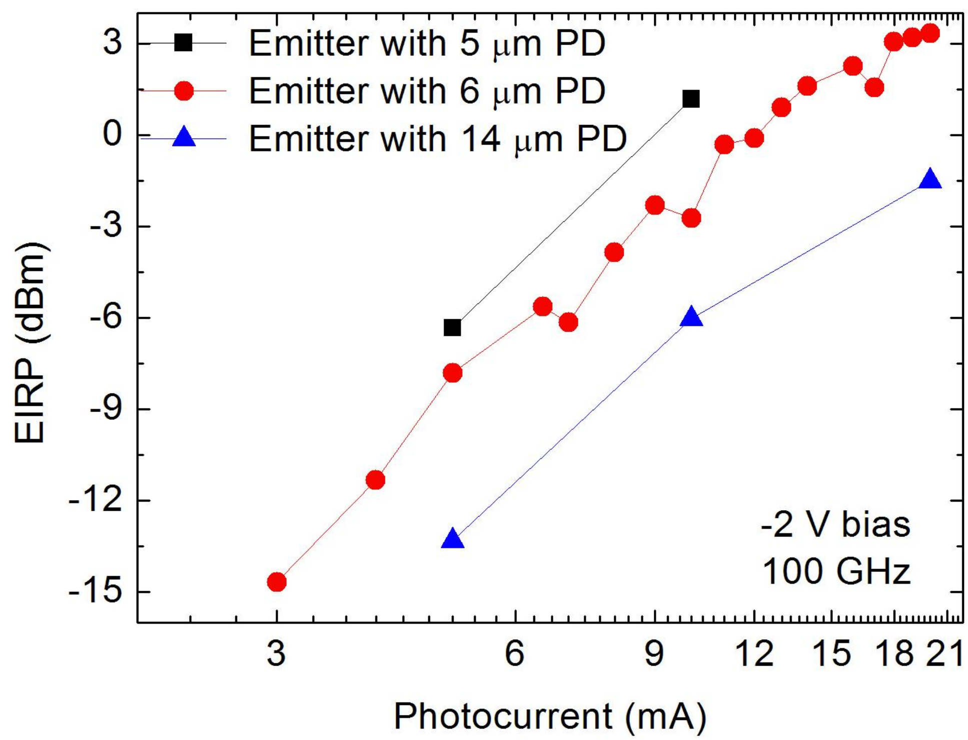

Figure 6-6. EIRP vs photocurrent at 100 GHz from the emitters with 5, 6 and 14 µm PDs at -2 V.

6.3.4 Radiation bandwidth and pattern of the integrated photonic emitter

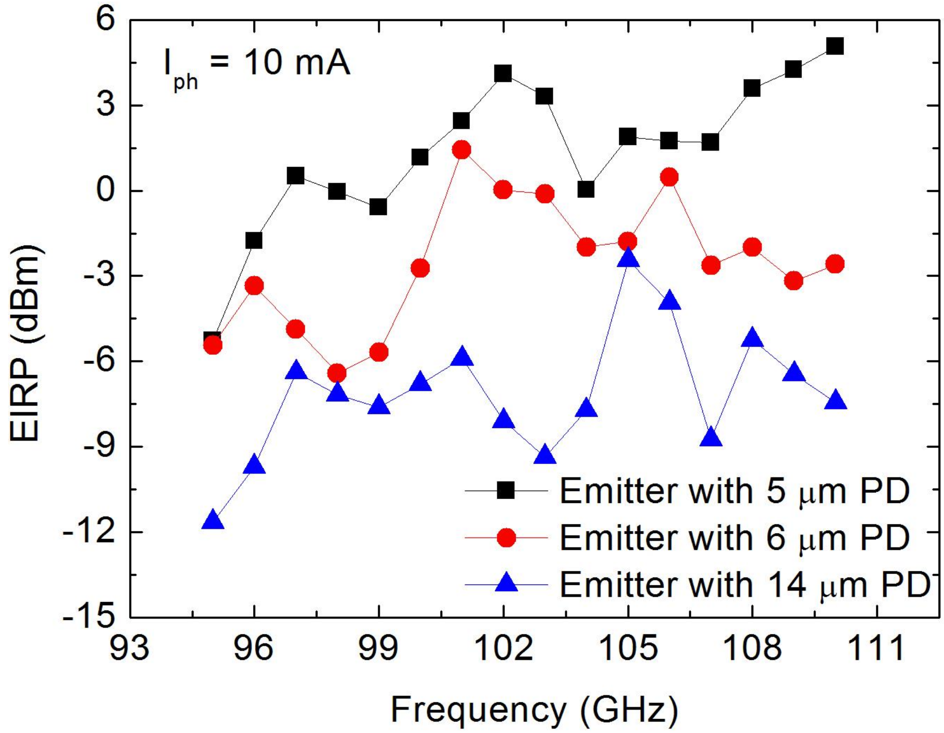

Figure 6-7. The EIRP of different PDs biased at 10 mA photocurrent from 95 to 110 GHz.

The radiation bandwidths of the integrated photonic emitters were measured by tuning the temperature of one laser diode to sweep the beat signal frequency from 95 to 110 GHz. The results are shown in Fig. 6-7. The EIRP is approximately 3, -3 and -7 dBm for the photonic emitters with 5, 6 and 14 µm-diameter PDs, respectively. The difference of the EIRP from the emitters with different PDs is due to the impedance matching condition. Moreover, the EIRP varies by several dB for each photonic emitter across the frequency band. This variation might result from the varying input impedance of the antenna plus matching network.

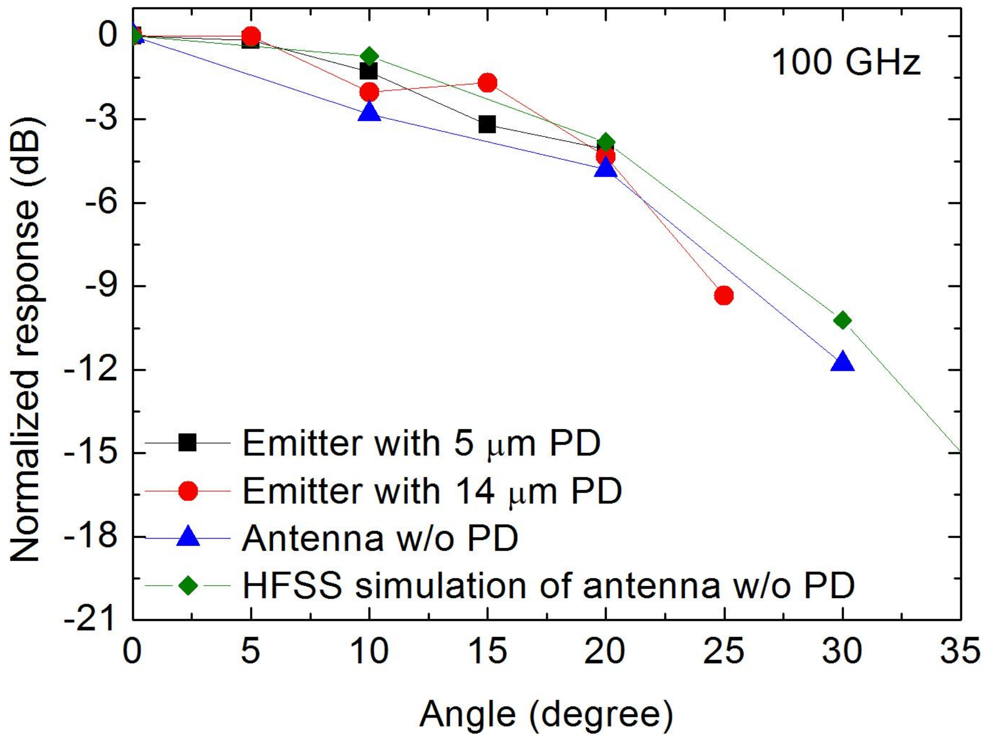

Figure 6-8. The E-plane radiation patterns of the integrated photonic emitters with 6 and 14 μm-diameter PDs, the antenna without PD and the HFSS simulation results.

The E-plane radiation patterns of the integrated photonic emitters were measured by changing the receiving horn antenna position in the far field. The results are shown in Fig. 6-8. Also shown in the figure is the E-plane radiation pattern of only the Vivaldi antenna for comparison. All measurements revealed a half main lobe of about 15 degrees. As expected, the antenna radiation pattern does not change when the PD is integrated. The HFSS simulation of the antenna radiation pattern on the E-plane is included in the figure for comparison. The simulation and measurement results agree reasonably well.

6.3 Summary

A W-band photonic emitter was successfully realized by integration of high-power flip-chip bonded MUTC PD and Vivaldi antenna. An EIRP as high as 5 dBm has been achieved at 110 GHz. The impedance matching has a large effect on the EIRP. The emitter has a wide -6 dB radiation bandwidth of approximately 10 GHz. The main lobe of the radiation pattern is 30º. The compact integrated photonic emitter is fully compatible with planar integration. The EIRP is among the highest that have been reported around 100 GHz in the literature.

Chapter 7. Conclusion and Future work

7.1 Conclusion

Back-illuminated flip-chip-bonded MUTC photodiodes with bandwidths in excess of 110 GHz have been achieved. Photodiodes with 10 µm- and 6 µm-diameters can deliver RF output power levels as high as 9.6 dBm at 100 GHz and 7.8 dBm at 110 GHz, respectively. The photodiodes have a typical responsivity of 0.17 A/W at 1.55 μm wavelength. The O/E power conversion efficiency was 3.2%. Analysis using a simple equivalent circuit model based on extracted parameters from S11 fitting data suggests that the bandwidths of the PDs are limited by the *RC* component and the parasitic capacitance is the primary bandwidth limitation for 5- and 6 μm-diameter devices. Through optimization of impedance of the CPW line together with the extracted parameter and circuit model, photodiodes with an optimized CPW were fabricated and characterized. Bandwidths of 125 GHz with flat frequency response were achieved with 5 µm-diameter, which is 12 % improvement compared with that from the previous CPW design. A 6 µm-diameter photodiode achieved 3.3 dBm and 0.83 dBm RF output power at 130 GHz and 150 GHz, respectively.

With the benefit of high speed along with high efficiency from a waveguide integrated photodiode, I demonstrated over 100 GHz-bandwidth, high-power evanescently-coupled waveguide MUTC photodiodes with 38 GHz bandwidth efficiency product compared with normal incidence devices of 15 GHz. Two groups of devices were designed and investigated. The photodiodes in the 1st group achived bandwidth of 70 GHz with high RF output power of 7.8 dBm and 6.1 dBm at 60 GHz and 70 GHz, respectively. Using results from the 1st device group, the redesigned 2nd group showed over 105 GHz bandwidth. With the improved gap design in terms of better optical field confinement along the narrow n-contact, these photodiodes achieved 30% higher bandwidth with the same external responsivity compared with the 1^{st} group. The RF output power from the photodiodes were 2 dBm and 1.3 dBm at 100 GHz and 105 GHz, respectively.

A W-band photonic emitter fabricated by integrating the normal-incidence with a Vivaldi antenna and matching network designed by Dr. Bower's group, was successfully realized. As high as 5 dBm EIRP has been achieved at 110 GHz, which is among the highest that have been reported in this frequency range. The emitter has a wide 6 dB radiation bandwidth of approximately 10 GHz with main lobe of 30º. The compact integrated photonic emitter is fully compatible with planar integration.

7.2 Future work

7.2.1 Dual waveguide input photodiode design

For waveguide photodiodes, one factor that limits the device saturation is nonuniform light absorption across the photodiode length. As seen in Figure 7-1 (a), as light propagates along the waveguide, the light is evanescently coupled and absorbed by the absorber. More light is absorbed at the front end and absorption decreases exponentially. Therefore, the front end saturates earlier and this localized saturation of waveguide photodiodes limits their ability to deliver high RF power comparable to normal-incidence photodiodes.

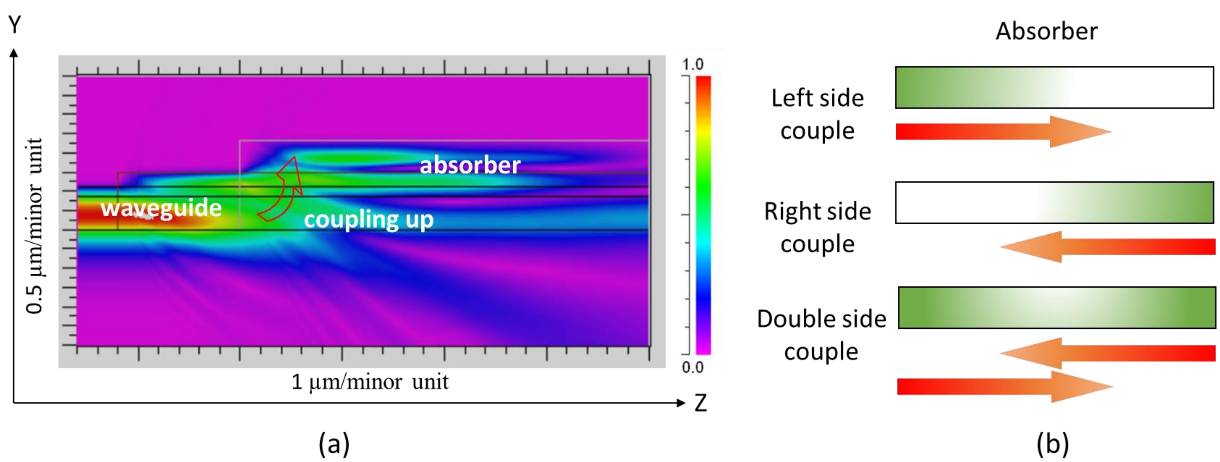

Figure 7-1. (a) Ununiform absorption through regular evanescently coulpling; (b) Doule side coupling regime.

In order to improve the performance, I propose a new waveguide photodiode design with dual waveguide input. As shown in Fig. 7-2 (a), for the new structure the input waveguide is divided into two waveguides using a 1 x 2 multimode interference (MMI) coupler. The two waveguides couple the light from two sides of the photodiode. As illustrated in Figure 7-1 (b), more uniform absorption can be achieved with double-side coupling compared with single-side coupling and high saturation current can be expected by this way.

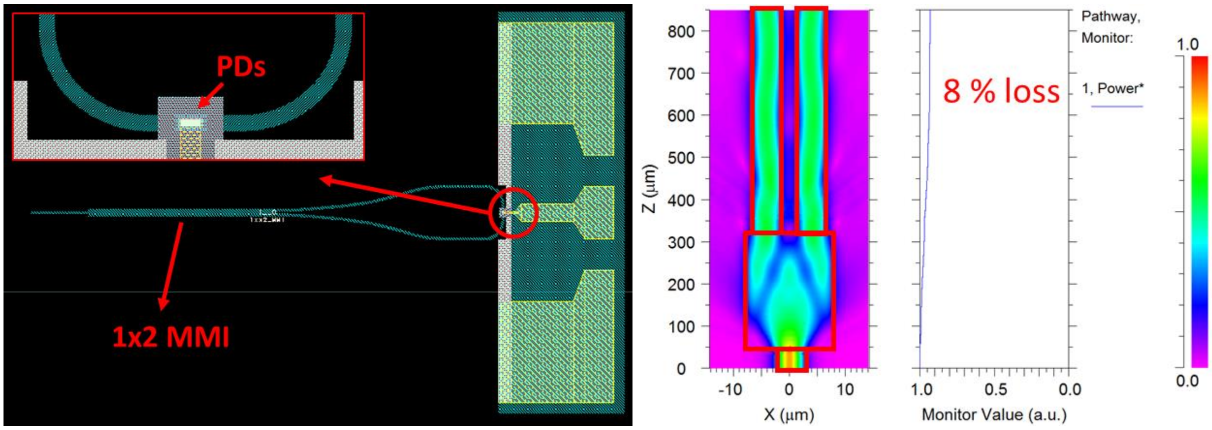

(a) (b)

Figure 7-2. (a) Layout design of dual-input waveguide photodiodes; (b) Simulation of 1x2 MMI optical absorption.

7.2.2 Bias Dependent RF Output Power

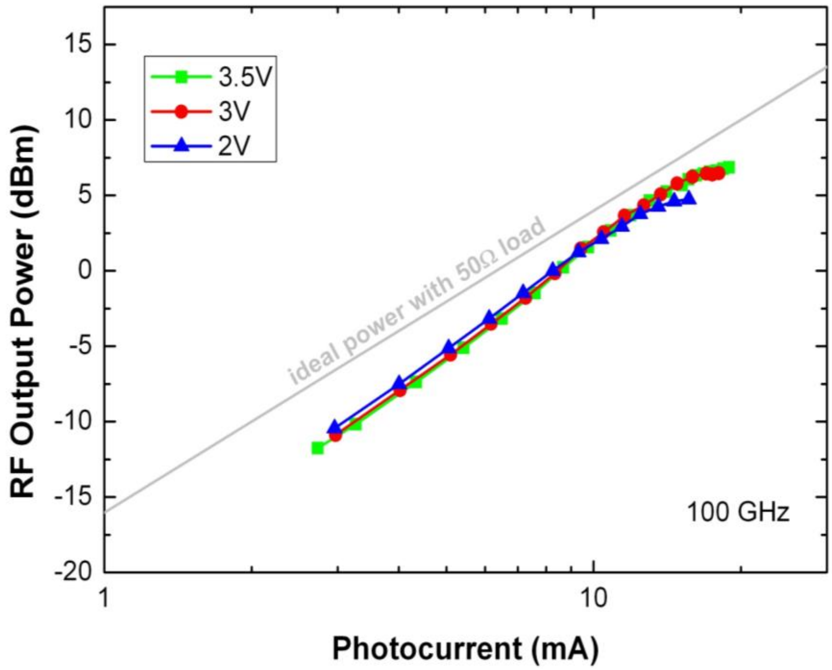

(a)

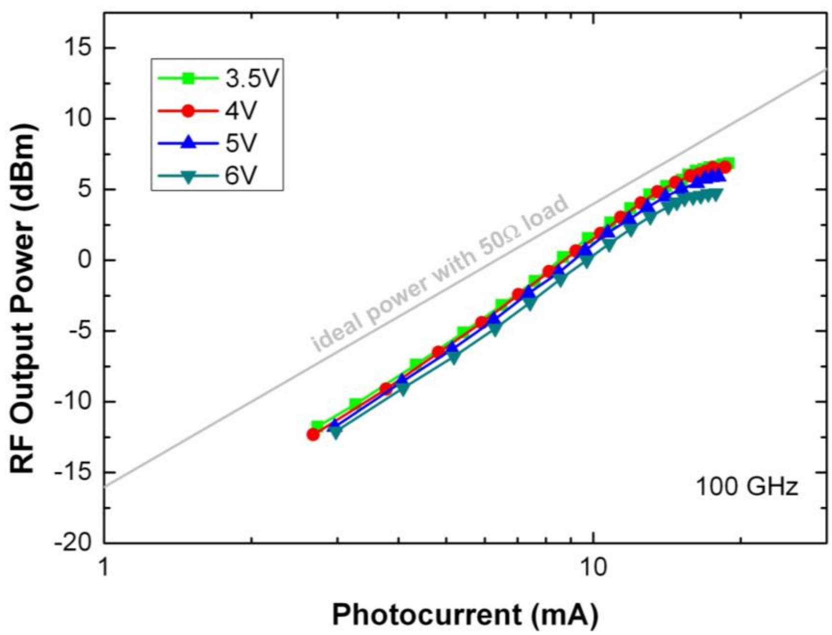

(b)

Figure 7-3. RF power versus average photocurrent at different bias for a 5 µm-diameter device at 100 GHz: (a) from 2 ~ 3.5 V; (b) from 3.5 ~ 6 V.

It is well known that, as more optical power is injected into the photodiode, higher photocurrent can result in a space-charge field that opposes the bias field. The result is reduced carrier velocity and, therefore, decreased bandwidth with lower RF output power. By increasing the bias voltage, the space-charge effect can be mitigated in terms of postponing the collapse of electric field and higher RF output power can be achieved.

The RF saturation of a 5 μm-diameter normal-incidence photodiode at 100 GHz with different reversed bias is shown in Fig. 7-3. Initially, the saturation RF power and saturation photocurrent increase as the bias increases from 2 V to 3.5 V as shown in Fig. 7-3 (a). However, as higher bias is applied, the output RF power decreases as seen in Fig. 7-3 (b), which is counter to what is usually observed. This phenomenon has also been observed on the waveguide photodiodes as shown in Fig. 5-11 (a).

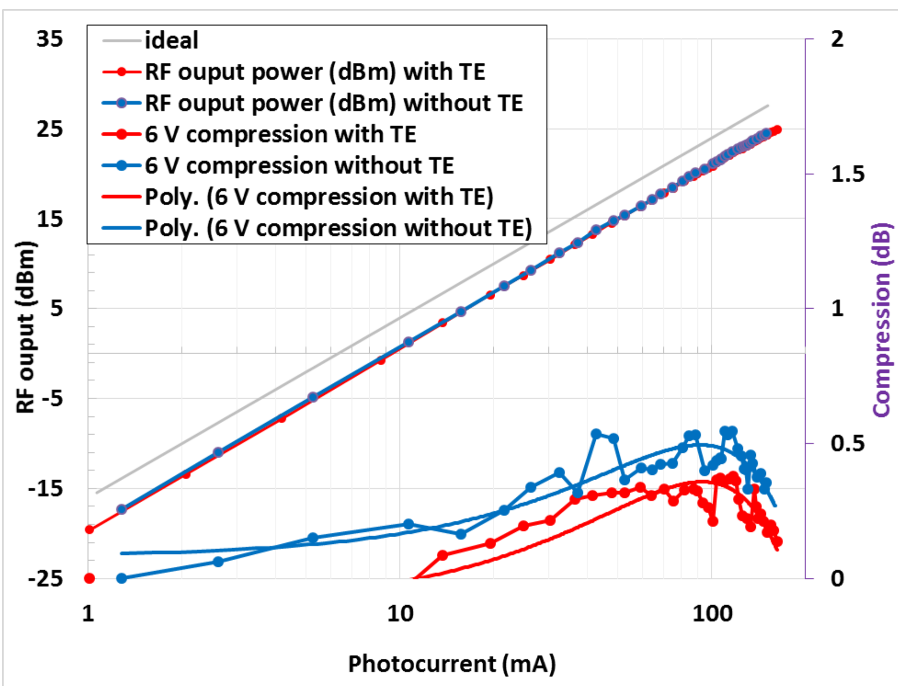

Figure 7-4. RF saturation of same MUTC device with and without TE cooler (-6 V reversed bias @ 8 GHz).

One possible explanation is that the device junction temperature increases when high bias is applied under the same photocurrent. The increased temperature affects the drift velocity of carriers, which leads to earlier saturation of the devices. To test the temperature effect, I measured the RF saturation with one of MUTC devices both at room temperature and with a thermoelectric (TE) cooler (set to 0 ºC). Figure 7-4 shows the saturation results of the same device with and without a TE cooler under -6 V bias. There is no apparent change in saturation compression, which indicates that the temperature does not have a significant impact on the RF saturation.

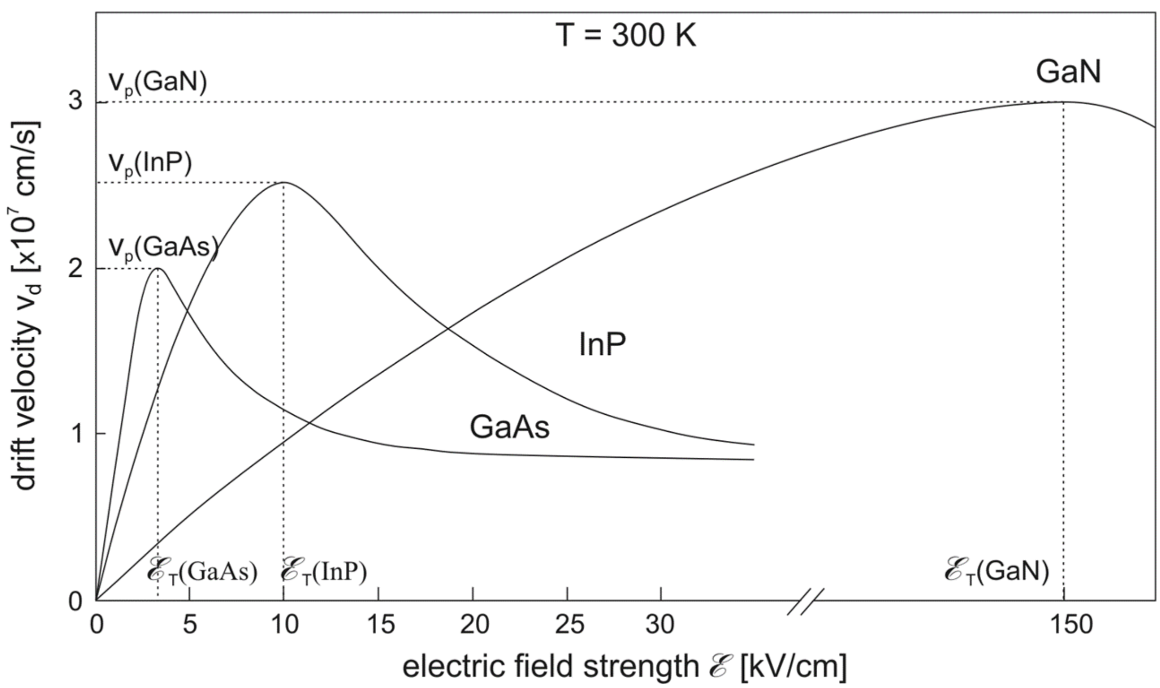

Figure 7-5. Steady state electron drift velocity vs E-field in GaAs, InP and GaN at room temperature.

Carrier velocity overshoot may be another possible reason. Figure 7-5 shows the average electron drift velocity at 300 K as a function of applied electric field for three different III-V materials [7-1]. A peak drift velocity is observed around 10 kV/cm for InP which is the drift layer material in the MUTC photodiodes that I have studied. The band structure needs to be considered in order to explain the velocity drop from its peak value. The Γ valley located in the center of the Brillouin zone has higher electron mobility than that of the L valley which is 0.59 eV higher in energy because of smaller electron effective mass in the Γ valley. As the electric field increases, the electrons in the Γ valley gain more average energy and the drift velocity increases. At a point where the electric field is high enough, the electrons in the Γ valley can be excited to the normally unoccupied L valley with lower drift velocity, resulting in a drop in the drift velocity. This is called inter-valley transfer. The peak of GaAs starts earlier because the energy difference between the Γ valley and L valley is 0.29 eV which is smaller than 0.59 eV of InP. Therefore, it requires less average energy for GaAs to initiate the inter-valley transfer, as shown in Figure 7-6 [7-2].

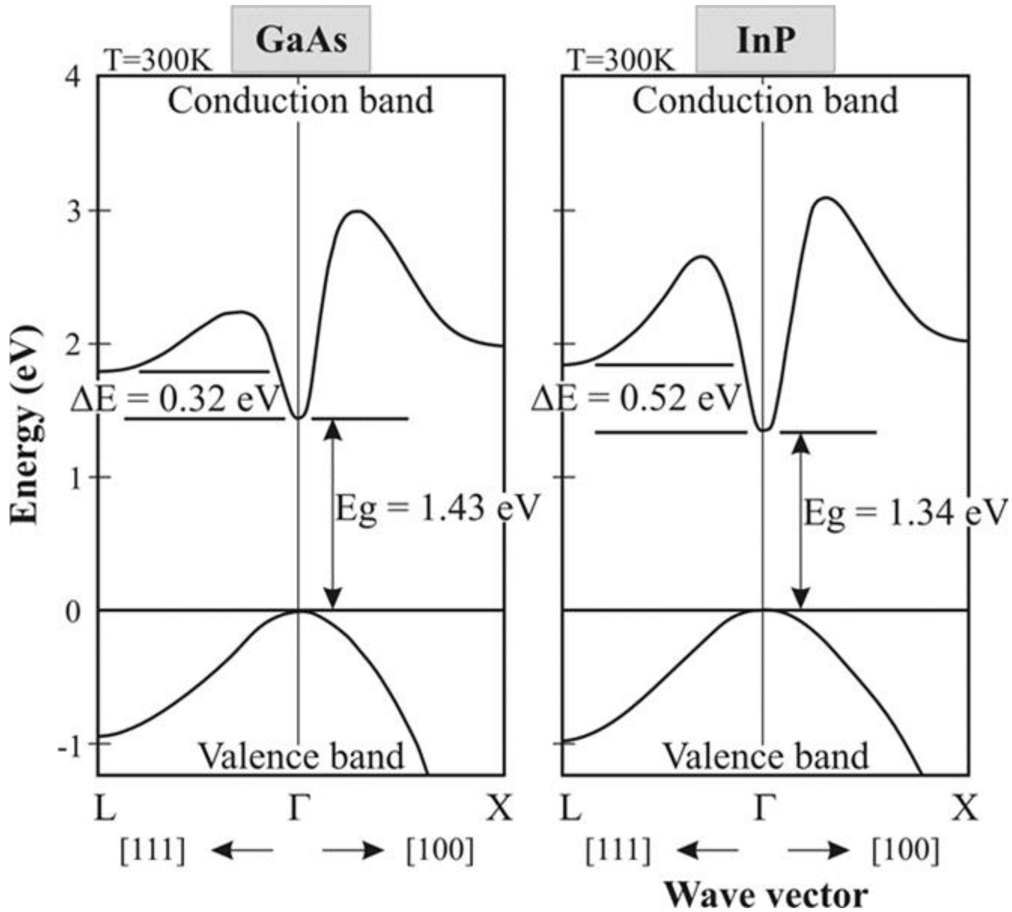

Figure 7-6. Simplified band structure of GaAs, InP.

Therefore, under illumination the electric field across the depletion region changes and there is a probability that the low reversed bias could result in overshoot drift velocity for the electrons, which leads to lower transit time, larger bandwidth and higher RF output power. This needs to be confirmed by software simulation with a drift velocity model taking the overshoot effect into consideration.

References

[1-1] V. J. Urick, J. D. McKinney and K. J. Williams, "Fundamentals of Microwave Photonics," Wiley Series in Microwave and optical engineering, first edition, published in 2015.

[1-2] Williamson, R.C. and R.D. Esman, "RF Photonics*,"* *Lightwave Technology, Journal of*, 2008. **26**(9): p. 1145-1153.

[1-3] Stephan Dill, *et al.*, "SUMIRAD-a fast imaging MMW radiometer for security and safety applications." *Proceeding of the 43rd European Microwave Conference*, pp. 1635 -1638, Oct. 2013.

[1-4] Angela S. Cacciapuoti, "Mobility-Aware User Association for 5G mmWave Networks." *IEEE Access*, Vol.5, pp. 21497-21507, Sep. 2017.

[1-5] Mike Kohler, *et al.*, "Considerations for Future Automorive Radar in the Frequency Range Above 100 GHz." *German Microwavve Conference Digest of Papers*, pp. 284-287, Mar. 2010.

[1-6] Sasan Bakhtiari, *et al.*, "Compact Millimeter-Wave sensor for Remote Monitoring of Vital Signs." *IEEE Transactions on Instrucmentation and Measreument*, Vol. 61, No. 3, Mar. 2012.

[1-7] IEEE 802 LAN/MAN Committee, *IEEE Standard for Information Technology—Telecommunications and Information Exchange Between Systems—Local and Metropolitan Area Networks—Specific Requirements. Part 15.3: Wireless Medium Access Control (MAC) and Physical Layer (PHY) Specifications for High Rate Wireless Personal Area Networks (WPANs) Amendment 2: Millimeter-wave-based Alternative Physical Layer Extension*, IEEE Standard 802.15.3c, IEEE Inc., New York (2009).

[1-8] Jeffrey A. Nanzer, Patrick T. Callahan, Michael L. Dennis and Thomas R. Clark Jr., "Photonic Signal Generation for Millimeter-Wave Communmicatons." *John Hopkins APL Techinical Digest*, Vol. 30, No.4, 2012.

[1-9] Alwyn Seeds, *et al.*, "Microwave Photonics: Present Status and Future Outlook." *International Topiocal Meeting on Microwave Photonices*, pp. 1-6, Oct. 2015.

[1-10] H. Shams, *et al.*, "100 Gb/s Multicarrier THz Wireless Transmission System With High Frequency Stability Based On A Gain-Switched Laser Comb Source." *IEEE Photonics Journal*, Vol.7, No.3, June 2015.

[2-1] http://www.ioffe.ru/SVA/NSM/Semicond/GaInAs/thermal.html.

[2-2] K. Kato, et al., "Design of Ultrawide-Band, High-Sensitivity p-i-n Photodiodes", IEICE Trans. Electrons., Vol.E76-C, No.2, Feb. 1993.

[2-3] David M. Pozar, *Microwave Engineering third edition*, Wiley-John Wiley & sons, TK7876.P69 2005.

[2-4] X. Li, N. Li, S. Demiguel, J. C. Campbell, D. Tulchinsky, K.J.Williams, "High–saturation-current InP-InGaAs photodiode with partically depleted absorber." IEEE Photonic Techonolgy Letters, Vol.15, pp. 1276-1278, Aug. 2003.

[2-5] T.Ishibashi, *et al.*, "Uni-traveling-carrier photodiodes," *Tech. Dig. Ultrafast Electronics Optoelectronics OSA Spring Topical Meeting*, pp.166-168, 1997.

[2-6] N. Li, et al., "High-saturation-current charge-compensated InGaAs/InP uni-travelling-carrier photodiode." *The 16th Annual Meeting of the IEEE, Lasers and Electro-Optics Socienty*, pp.790-791, Oct. 2003.

[2-7] D.H. Jun, J.H. Jang, Ilesanma Adeseda, J.I. Song, "Improved efficiency bandwidth product of Modified Uni-traveling Carrier Photodiode Structure using an undoped Photo-absorption Layer," *Janpanese Journal of Applied Science*, vol. 45, no. 4B, pp. 3475-3478, 2006.

[2-8] N. Li, X. Li, S. Demiguel, X. Zheng, J.C. Campbell, D.A. Tulchinsky, K.J. Williams, T.D. Isshiki, G.S. Kinsey and R. Sudharsansan, "High saturation current charge-compensated InGaAs –InP uni-traveling-carrier photodiode," *IEEE Photo. Technol. Lett.*, vol. 16, no. 3, pp. 864-866, Mar. 2004.

[2-9] N. Shimizu, N. Watanabe, T. Furuta and T. Ishibashi, "InP-InGaAs un-traveling-carrier photodiode with improved 3-dB bandwidth of over 150 GHz," *IEEE Photon. Technol. Lett.*, vol. 10, no. 3, pp. 412-414, 1998.

[2-10] Zhi Li, et al., "High-saturation high-linearity flip-chip bonded modified uni-traveling carrier photodiode," *Opt. Express*, vol. 19, no. 26, pp. B385-B390, 2011.

[2-11] Q. Zhou, A.S. Cross, A. Beling, Y. Fu, Z. Lu, J. C. Campbell, "High Power V-Band InGaAs/InP Photodiodes," *IEEE Photon. Technol. Lett.*, vol. 25, no. 10, 2013.

[2-12] X. Xie, Q. Zhou, K. Li, Y. Shen, Q. Li, Z. Yang, A. Beling and J.C. Campbell, "Improved Power Conversion Efficiency in High Performance Photodiodes by flip chip on diamond," *Optica.*, vol.1, no.6, pp. 429-435, Dec. 2014.

[3-1] Victor G. Weizer, Navid S. Fatemi and Andreas L. Korenyi-Both, "Au/Zn contacts to p-Inp: Electrical and Metallurgical Characteristics and the Relationship Between Them." *MRS Spring Meeting*, Apr. 1994.

[3-2] F.G. Ivey, D. Wang, D. Yang, R. Bruce and G.Knight, “Au/Ge/Ni ohmic contacts to n-Type InP.” *Journal of Electronics Materials*, Vol.23, Issue 5, pp. 441-446, May 1994.

[4-1] Z. Li, H. Pan, H. Chen, A. Beling, and J.C. Campbell, “High-Saturation–current modified uni-traveling-carrier photodiode with cliff layer,” *IEEE J. of Quantum Electronics*., vol.46, no. 5, pp. 626-632 May 2010.

[4-2] E. B. Rosa, “The Self and Mutual Inductances of Linear Conductors”, *Bulletin of the Bureau of Standards*, Vol.4, No.2, pp301~344, Sep. 1907.

[4-3] MV. Fischetti, “Monte Carlo simulation of Transport in Technologically Significant Semiconductors of Diamond and Zinc- Blende Structures Part I- Homogeneous Transport,” *IEEE Transaction on Electron Devices*, vol. 38, no. 3, Mar. 1991.

[4-4] Xiaojun Xie, Kejia Li, Yang Shen, Qinglong Li, Jizhao Zang, Andreas Beling, and Joe C. Campbell, "Photonic Generation of High-Power Pulsed Microwave Signals," *J. Lightwave Technol.*, 33, 3808-3814 (2015).

[5-1] Qinglong Li, Kejia Li, Yang Fu, Xiaojun Xie, Zhanyu Yang, Andreas Beling, and Joe C. Campbell, "High-Power Flip-Chip Bonded Photodiode with 110 GHz Bandwidth," *J. Lightwave Technol*., vol. 34, issue 9, pp. 2139-2144, May 2016.

[5-2] John E. Bowers, C.A. Burrus, “High-speed zero-bias waveguide photodetectors,” *Electronics letters*, vol.22, issue 17, pp. 905-906, August 1986.

[5-3] Xiaojun Xie, et al., “High-Power and High-Speed Heterogeneously Integrated Waveguide-Coupled Photodiodes on Silicon-on-Insulator,” *J. Lightwave Technol.*, vol. 32, issue 1, pp. 73-78, Jan 2016.

[5-4] A. Beling, H.-G. Bach, R. Kunkel, G. G. Mekonnen, and D. Schmidt, “InP-Based 1.55 μm high-speed photodetectors for 80 Gbit/s systems and beyond,” in *Proc. Int. Conf. Transp. Opt. Netw.*, Jul. 2015, pp. 303–308.

[6-1] J. Federici and L. Moeller, “Review of terahertz and subterahertz wireless communications,” *Appl. Phys. Lett.*, vol. 107, pp. 111101, 2010.

[6-2] P. Cheolhee, and T. S. Rappaport, “Short-range wireless communications for next-generation networks: UWB, 60 GHz millimeter-wave WPAN, and ZigBee,” *IEEE Wireless Comm.*, vol. 14, no. 4, pp. 70-78, 2007.

[6-3] A. Stohr, S. Babiel, P. J. Cannard, B. Charbonnier, F. van Dijk, S. Fedderwitz, D. Moodie, L. Pavlovic, L. Ponnampalam, C. C. Renaud, D. Rogers, V. Rymanov, A. Seeds, A. G. Steffan, A. Umbach, and M. Weib, “Millimeter-wave photonic components for broadband wireless systems,” *IEEE Trans. Microw. Theory Techn.*, vol. 58, no. 11, pp. 3071-3082, 2010.

[6-4] N. Chen, H. Tsai, F. Kuo, and J. Shi, “High-speed W-band integrated photonic transmitter for radio-over-fiber applications,” *IEEE Trans. Microw. Theory Techn.*, vol. 59, no. 4, pp. 978-986, 2011.

[6-5] Friis, H.T., "A Note on a Simple Transmission Formula". *IRE Proc.*: 254–256, May 1946.

[7-1] H. Ibach and H. Lueth. *Solid-State Physics*. Springer Verlag, 2003.

[7-2] S. M.Sze. *Physics of Semiconductor Devices*. Wiley-Interscience, 2nd edition, 1981.

A. List of publicaions

- Qinglong Li, Kejia Li, Yang Fu, Xiaojun Xie, Zhanyu Yang, Andreas Beling, and Joe C. Campbell, "High-Power Flip-Chip Bonded Photodiode with 110 GHz Bandwidth," *J. Lightwave Technol.*, vol. 34, issue 9, pp. 2139-2144, May 2016.
- Qinglong Li, Keye Sun, Kejia Li, Qianhuan Yu, Patrick Punge, Willi Ebert, Andreas Beling, and Joe C. Campbell, "High-Power Evanescently-Coupled Waveguide MUTC photodiode with > 105 GHz Bandwidth," *J. Lightwave Technol.*, vol. 35, no.21, pp. 2139-2144, Nov. 2017.
- Qinglong Li, Keye Sun, Kejia Li, Qianhuan Yu, Patrick Punge, Willi Ebert, Andreas Beling, and Joe C. Campbell, "High-Power waveguide MUTC photodiode with 70 GHz Bandwidth," *Microwave Photonics (MWP), 2016 IEEE International Topical Meeting on,* pp. 225-228.
- Qinglong Li, Keye Sun, Kejia Li, Qianhuan, Yu, Jizhao Zang, Ze Wang, Patrick Punge, Willi Ebert, Andreas Beling and Joe C. Campbell, “Waveguide-Integrated High-Speed and High-Power Photodiode with >105 GHz Bandwidth,” *IEEE Photonics Conference(IPC)*, Oct. 2017.
- Qinglong Li, Kejia Li, Xiaojun Xie, Yang Fu, Zhanyu Yang, Yang Shen, Ye Wang, Andreas Beling and Joe C. Campbell, “High-power chip-chip bonded photodiode with 110 GHz bandwidth,” *IEEE Photonics Conference (IPC)*, pp. 450-451, Oct. 2015.
- Qinglong Li, Kejia Li, Xiaojun Xie, Zhanyu Yang, Andreas Beling and Joe C. Campbell, “Development of high-power photodiodes for W-band applications,” *Avionics and Vehicle Fiber-Optics and Photonics Conference (AVFOP)*, pp. 22-23, Nov. 2015 (Invited).

- Xiaojun Xie, Kejia Li, Yang Shen, Qinglong Li, Jizhao Zang, Andreas Beling and Joe C. Campbell, "Photonic generation of high-power pulsed microwave singals," *Journal of Lightwave Technology*, Vol.33, Issue 18, pp. 3808-3814, Sep. 2015.
- Kejia Li, Xiaojun Xie, Qinglong Li, Madison E. Woodsen, Zhanyu Yang, Anreas Beling and Joe C. Campbell, "High Power Photodiode integrated with coplanar patch antenna for 60 GHz applications," *IEEE Photonics Letters*, Vol. 27, Issue 6, pp. 650-653, Mar. 2015.
- Gan Zhou, Patrick Runge, Shahram Keyvaninia, Sten Seifert, Willi Ebert, Sven Mutschall, Angela Seeger, Qinglong Li and Andreas Beling, "High-power InP Based waveguide integrated modified uni-traveling-carrier photodiodes," *Journal of Lightwave Technology*, Vol.35, Issue 4, pp.717-721, Apr. 2017.
- Keye Sun, Jesse Moody, Qinglong Li, Steven M. Bowers and Andreas Beling, "High Power Integrated Photonic W-band Emitter," *IEEE Transactions on Microwave Theory and Techniques*, Vol. pp, Issue 99, Oct. 2017.
- Andreas Beling, Joe C. Campbell, Kejia Li, Qinglong Li, Ye Wang, Madison E. Woodsen, Xiaojun Xie, Zhanyu Yang, "High-power photodiodes for analog applications," IEICE Transactions on Electronics, Vol. 98, Issue 8, pp.764-768, Aug. 2015.
- Xiaojun Xie, Qiugui Zhou, Kejia Li, Yang Shen, Qinglong Li, Zhanyu Yang, Andreas Beling and Joe C. Campbell, "Improved Power Conversion Efficiency in High Performance Photodiodes by flip chip on diamond," *Optica.*, vol.1, no.6, pp. 429-435, Dec. 2014.

109

- Gan Zhou, Willi Ebert, Sven Mutschall, Angela Seeger, Patrick Runge, Qinglong Li and Andreas Beling, "High-power waveguide integrated MUTC photodiode with 5 dBm RF output power at 120 GHz," *Optical Fiber Communication Conference (OFC)*, Tu2D.3, Mar. 2016.
- Zhanyu Yang, Xiaojun Xie, Qinglong Li, Joe C. Campbell, and Anreas Beling, "20 GHz analog photonic link with 16 dB gain based on a high-power balanced photodiode," *IEEE Photonic Conference (IPC)*, pp.144-145, Oct. 2015.
- Keye Sun, Jesse Moody, Qinglong Li, Steven M. Bowers, Andreas Beling, "High-power Integrated Photodiode-Antenna Emitter for 100 GHz Applications," *Integrated Photonics Research, Silicon and Nanophotonics*, IW2A. 6, July 2016.
- Jesse Moody, Keye Sun, Qinglong Li, Andreas Beling, and Steven M. Bowers, "A Vivaldi antenna based W-band MUTC photodiode driven radiator," *Microwave Photonics (MWP), 2016 IEEE International Topical Meeting on*, pp.217-220, Oct. 2016.
- Patrick Punge, Gan Zhou, Shahram Keyvaninia, Sten Seifert, Angela Seeger, Qinglong Li, and Andreas Beling, "Waveguide integrated balanced MUTC photodiode," *CLEO: Science and Innovations*, sTh1G. 4, June 2016.
- Kejia Li, Xiaojun Xie, Efthymios Rouvalis, Sascha Fedderwitz, Andreas G. Steffan, Qinglong Li, Zhanyu Yang, Andreas Beling, and Joe C. Campbell, "High-power photodetector modules for microwave photonic applications," *SPIE OPTO*, pp. 93620x-93620x-6, March 2015.

B. Vita

Qinglong Li (李庆龙), son of Shulai Li (李树来) and Bingqin Xue (薛炳琴), was born on Feburary 16, 1985 in Tianjin, China. After completing his study at Tianjin No.47 middle school, he began his undergraduate study in Nankai University majoring in Microelectronics in 2004. After which, he worked for semiconductor international manufacturing corporation (SMIC) for over 1 year as a process integration engineer (PIE) in 2008. He then pursued his master of science degree with research focusing on thin film transistor (TFT) on glass for display under Dr. Karl Hirschman's supervision at Rochester Institue of Technology in 2010. In August 2013, he joined the Ph.D. program at ECE deparment in Univeristy of Virignia. In May 2014, he started his research on high power and high speed photodiodes, advised by Dr. Joe C. Campbell and co-advised by Dr. Andreas Beling.

Permanent address: 7-4-501 Jingtian Apartment, Jiarongli Street, Tianjin, China 300134

This dissertation is typed by the author.